Quasi-Optical Planar Grids for Microwave and Millimeter-Wave Power Combining

Thesis by

Robert M. Weikle, II

In Partial Fulfillment of the Requirements

for the Degree of

Doctor of Philosophy

California Institute of Technology

Pasadena, California

1992

(Submitted November 20, 1991)

To my Parents

Acknowledgements

I would like to express my gratitude to David Rutledge for his encouragement, support, and the opportunity to work in his research group. Under his guidance, I have learned much and I feel privileged to have been his student.

Many thanks go to Bill Hant and the Northrop Corporation for their support and interest in this project. In addition, I would like to acknowledge Emilio Sovero, Aiden Higgins, and the folks at the Rockwell Science Center for financial support and many interesting discussions.

It is with pleasure that I thank the past and present members of the Caltech MMIC group. I am grateful for their friendship, advice, and many extracurricular activities. For introducing me to the world of device fabrication, I thank Wayne Lam, Gabriel Rebeiz, and Wade Regehr. For help with measurements and discussions on a wide range of topics, thanks go to Kent Potter, Wyman Williams, Rick Compton, and Arthur Sheiman. I am indebted to my grid comrades, Zoya Popović, Moonil Kim, Jon Hacker, and Mike De Lisio for their insight and many valuable suggestions. It has been my good fortune to work with them and they have taught me much. Special thanks go to Victor Lubecke and Scott Wedge, my office mates, for rekindling my interest in the guitar. I also wish to thank Yong Guo, Karen Lee, Lars Foged, Olga Borić, Jung-Chih Chiao, Alina Moussessian, Shijie Li, David Haub, Erik Kollberg, and Koji Mizuno for their friendship and good conversation.

For accompanying me on numerous trips into the mountains and helping me stay sane during my graduate studies, I thank Phil Stimson, Matt Newlin, and Dan Laughlin. I am also thankful for the friendship and kindness of Dee Burgess, Tricia Stimson, Frank Markle, Randy Lee, Jon Burnett, Alan Mathiowetz, David Hudson, and Andy Crocker.

And finally, I thank my mother and father for always being there. For their love and encouragement, I will always be grateful.

No man can reveal to you aught but that which already lies half asleep in the dawning of your knowledge.

The teacher who works in the shadow of the temple, among his followers, gives not of his wisdom, but rather of his faith and lovingness.

If he is indeed wise, he does not bid you enter the house of wisdom, but rather leads you to the threshold of your own mind.

— Kahlil Gibran

Quasi-Optical Planar Grids for Microwave and Millimeter-Wave Power Combining

Abstract

Solid-state devices that produce radiation in the microwave and millimeter-wave region of the electromagnetic spectrum have relatively low power outputs compared to their electron-tube counterparts. In an attempt to obtain more power from solid-state sources, a number of power-combining schemes have been developed through the years. One of the most promising techniques involves superposing the outputs of many devices in free space. This quasi-optical approach has several advantages: the losses associated with waveguides and feed networks are eliminated, the power can be distributed over a large number of devices, and an external phase-locking signal is unnecessary. In this work, a method for quasi-optical power combining which is based on integrating devices into periodic grids is discussed. The approach is relatively simple to implement because the grid structures are planar. Thus they easily accommodate solid-state devices and allow for the possibility of wafer-scale integration. A method for analyzing the grids is presented and used to derive models for a variety of configurations. The validity of these models is investigated using a quasi-optical reflectometer. Designs and experimental results for MESFET oscillator grids operating in X-band and Ku-band are examined and discussed in detail.

Contents

Chapter 1

Introduction

Millimeter and submillimeter-wave systems continue to be a subject of growing interest. The applications involving this portion of the electromagnetic spectrum cover a broad range of scientific disciplines, varying from the measurement of electron densities in tokamak plasmas [1] to studying emission spectra of distant celestial bodies [2]. Millimeter waves correspond to the frequencies between 30 GHz and 300 GHz and the submillimeter-wave range is regarded as the region between 300 GHz and 3000 GHz. The shorter wavelengths at these frequencies allow the use of smaller and lighter components than for microwave systems. This is important in military and space-borne applications where size and weight are a prime concern. In addition, the atmospheric attenuation of millimeter waves is relatively low compared to infrared and optical wavelengths [3], particularly in the transmission windows that lie between water vapor and oxygen absorption peaks. This property can be exploited to build radars and cameras that penetrate clouds, smoke, and haze. Other commonly cited advantages of millimeter and submillimeter wave components over their microwave counterparts include broader bandwidths and higher resolution for radars and imaging systems.

1.1 Sources of Radiation

The lack of reliable, inexpensive high-power sources, however, has been a persistent obstacle in the development of millimeter and submillimeter-wave systems. The first devices to produce radiation in this part of the spectrum were

electron tubes. Today, electron tube devices such as klystrons and crossed-field amplifiers (CFA) are widely available and can produce several kilowatts of power in the microwave and lower millimeter-wave range [4,5]. Traveling-wave tubes are capable of better than 100 W at 100 GHz [6]. In the far infrared and submillimeter-wave range, optically-pumped FIR lasers have achieved several megawatts of pulsed power [7]. Nevertheless, in many circumstances, the size, weight, and required high-voltage power supplies of these devices limit their usefulness.

For most low and medium power applications, electron tube sources have been replaced by solid-state devices. Compared to tube sources, solid-state devices are small, light-weight, inexpensive, and require small to moderate voltages. At present, IMPATT's — the most powerful millimeter-wave solid-state sources — can produce several watts of power at 100 GHz. Silicon IMPATT's have produced useful power up to 300 GHz [9]. A major drawback of IMPATT's, however, is the high noise level arising from the avalanche multiplication process. Gunn diodes have better noise performance but only generate a few hundred milliwatts at 100 GHz [10]. Other two-terminal solid-state devices used to produce millimeter and submillimeter wave radiation include quantum well oscillators [11] and Josephson junctions [12], although the power levels are extremely small. An additional drawback of two-terminal solid-state sources is low DC-to-RF conversion efficiency. Better efficiencies can be realized with transistors. Pseudomorphic HEMT's have demonstrated output powers near 60 mW at 94 GHz [13]. HEMT's with 0.15 μm gate lengths have shown cutoff frequencies of over 170 GHz with $f_{\max}$ near 350 GHz [14]. Heterojunction bipolar transistors (HBT's) also have the potential to provide reasonable power levels at millimeter-wave frequencies without the need for sub-micron lithography. An HBT with emitter area of 80 μm^2 has shown 15 dB of gain with output power of 16 dBm at 35 GHz [15].

In an attempt to overcome the limited power output of solid-state devices, a variety of power-combining methods have been developed. A good review of these methods has been given by Chang and Sun for millimeter-wave frequencies [16]. Many of these techniques are based on scaled-down microwave circuits and involve resonant cavities [17] or hybrids. Resonant cavity combiners allow good isolation between the active devices and have been used up to 300 GHz. Hybrid power combiners, which often rely on external injection-locking to synchronize the sources, have been used up to 140 GHz. These approaches have a number of disadvantages. To prevent moding problems at higher frequencies, the size of the waveguide cavities must be scaled down. This makes circuit fabrication more difficult. Resistive losses in the waveguide walls, which reduce power-combining efficiency, become more severe at millimeter and submillimeter frequencies. In addition, combiners based on resonant cavities and hybrids can accommodate a limited number of devices, making large-scale power-combining impractical.

1.2 Quasi-Optical Power Combining

An approach which overcomes the limitations of power combiners based on scaled-down microwave systems involves combining the output powers of many devices in free space. Mink suggested using an array of millimeter-wave devices placed in an optical resonator as a means of large-scale power combining [18]. While it is unlikely that solid-state power-combiners will replace high-power electron tube sources, there is great potential for improvement in output power and combining efficiency by using quasi-optical techniques. Because the power is combined in free space, losses associated with waveguide walls and feed networks are eliminated. The power can be distributed over a larger number of devices than in a waveguide cavity because the quasi-optical resonator can be many wavelengths across. An external injection-locking signal is unnecessary because synchronization of the sources is accomplished by mutual coupling through the modes of the resonator.

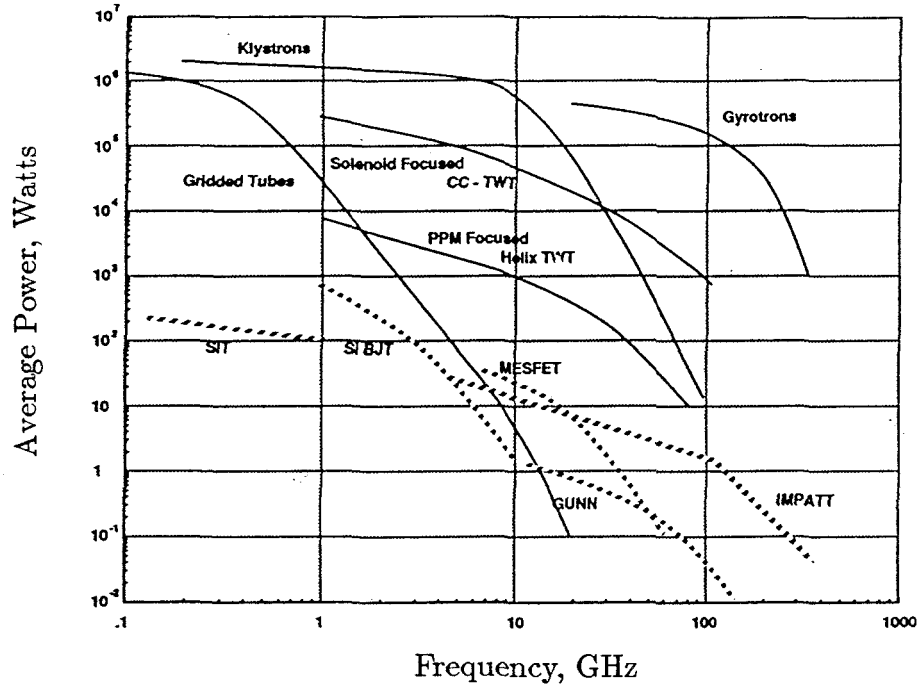

Figure 1.1 Comparison of output power vs. frequency for various microwave and millimeter-wave sources [8].

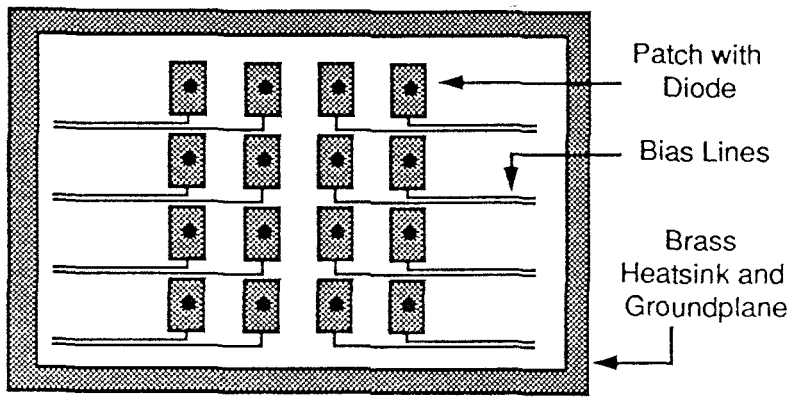

Figure 1.2 Schematic of a patch antenna power-combining array. Each patch element is excited with a Gunn diode and synchronization is achieved by adjusting the DC bias and using a partially transmitting reflector [22].

Several types of quasi-optical power combiners have been demonstrated over the past few years. Wandinger and Nalbandian combined the outputs of two Gunn diodes at 60 GHz using tapered dielectric rod antennas coupled to a Gaussian resonator [19]. Many designs have used microstrip radiators which are synchronized with feedback or an external signal. Stephan *et al.* investigated the coupling between open resonators and microstrip circuits at 10 GHz [20]. The microstrip ground plane and a spherical reflector formed the Gaussian cavity. Using this configuration, the output powers of two Gunn diodes were combined in free space [21]. A different approach, shown in Fig. 1.2, involves an array of weakly coupled patch antenna elements [22]. This method is similar to classic antenna arrays; each patch antenna is a free-running oscillator containing an active device [23]. The patch elements, which may contain either Gunn diodes or MESFET's, are synchronized using separate DC bias to each device. A dielectric slab placed above the array also facilitates locking. With this scheme, a 16-element MESFET array operating at 8 GHz produced 184 mW of power with a DC-to-RF efficiency of 25%. Linear arrays of patch antennas have also been used to combine the outputs of Gunn diodes at the second harmonic (18 GHz) [24]. More recently, a two-sided microstrip configuration has been developed that permits isolation between an external locking signal and the array output [25]. A different approach to quasi-optical power combining is based on integrating solid-state devices directly into a periodic grid.

1.3 Grid Oscillators

Grid oscillators are periodic arrays with embedded active solid-state devices. The grid is placed in a Fabry-Perot resonator to provide the feedback necessary for oscillation. This is illustrated in Fig. 1.3. Two important features distinguish grid oscillators from most quasi-optical power combiners built from microstrip circuits. First, grid oscillators do not necessarily have a ground plane and, as a result, do not rely on the interaction of microstrip modes with free-space ra-

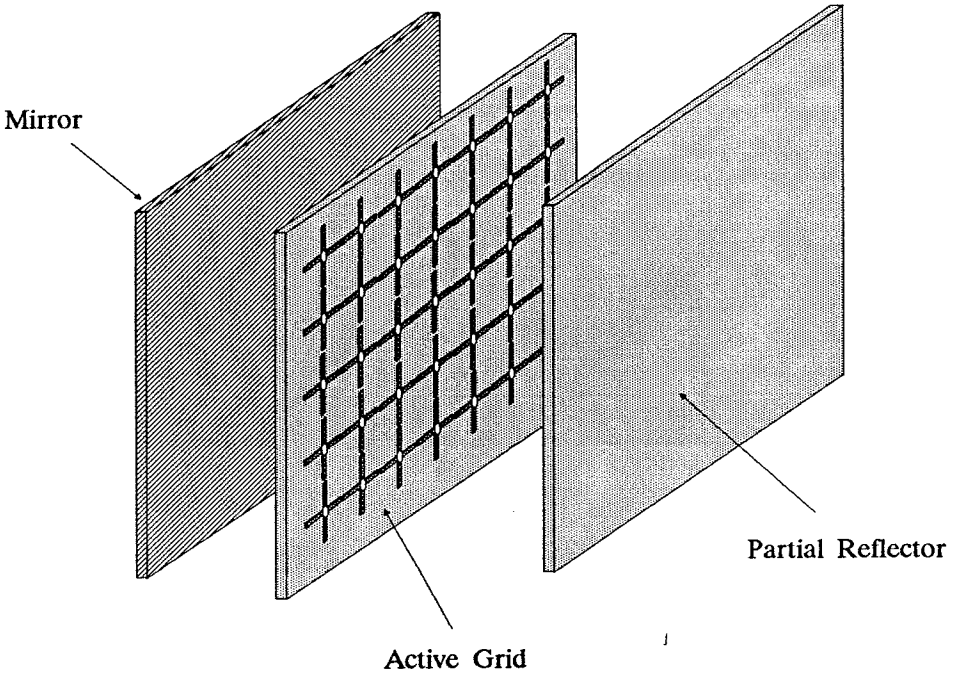

Figure 1.3 Grid oscillator configuration. An array of active devices is placed in an open resonator.

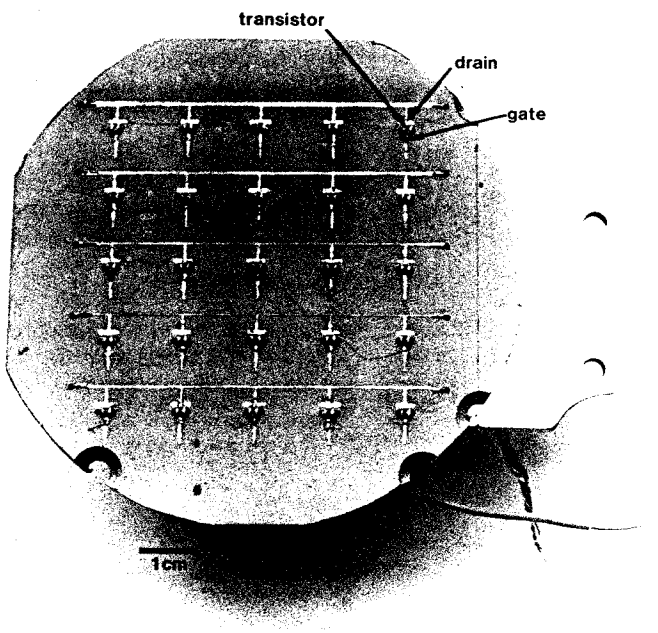

Figure 1.4 Photograph of a 25-element oscillator grid. The devices are packaged MESFET's (*Fujitsu* FSC11LF) and the substrate is a laminate (*Duroid*) fabricated by the Rogers Corporation.

diation. Second, microstrip-based power-combiners tend to be a collection of individual free-running oscillators that are weakly coupled. Thus, the operating frequency depends primarily on the behavior of the individual oscillators. In contrast, the elements making up an oscillator grid are not themselves free-running oscillators. Mutual interaction of all the devices in the grid is necessary for oscillation to occur. Consequently, the oscillation frequency and output power are strongly affected by the device spacing and the grid configuration. Each device in the array is presented with an embedding impedance which is a function of the grid structure. This embedding impedance, together with the device impedance, determines the grid's overall behavior as an oscillator.

A variety of transistor power-combining grids have been investigated. The first transistor oscillator grid, demonstrated by Popović *et al.* [26] in 1988, is shown in Fig. 1.4. The array is built on a dielectric substrate 2.35 mm thick with a dielectric constant 10.5. Packaged MESFET's are soldered to the grid. The metallized backside of the substrate and a planar dielectric slab placed in front of the grid form a Fabry-Perot resonator. The grid oscillates at 9.7 GHz and gives an output power of 464 mW with an efficiency of 15%.

1.4 Organization of the Thesis

This thesis consists of two main sections. Chapters 2 and 3, which constitute the first section, present a simple theoretical framework for analyzing planar quasi-optical grids. The analysis technique presented is used to derive models for these grids. The second section, consisting of chapters 4 and 5, presents experimental work involving the verification and application of these models.

Chapter 2 is an outline of the induced EMF method, a technique used to analyze radiating structures. This method is applied to planar periodic grids to find expressions for the grid driving-point impedance. Two simple structures, an inductive and a capacitive grid, are analyzed to illustrate the application of the method.

In chapter 3, the transmission-line models for three different grid configurations are derived. These derivations are based on the analysis presented in chapter 2. Two of the grids, a rectangular slot array and a bow-tie array, are suitable for two-terminal device integration. The third structure is compatible with three-terminal devices and is used as the configuration for planar transistor oscillator grids.

Chapter 4 describes a quasi-optical reflectometer that uses an HP 8510 vector network analyzer. The reflectometer is used to measure the reflection coefficient of the grids analyzed in chapters 2 and 3. These measurements allow us to evaluate the validity of the grid models derived using the EMF method.

Quasi-optical power combining using planar MESFET grids is the subject of chapter 5. The planar transistor array analyzed in chapter 3 is used to design a number of oscillator grids. Two basic grid configurations are examined and a design procedure is discussed. Experimental results for the oscillator grids are also presented.

In chapter 6, suggestions for future research involving quasi-optical active grids are discussed.

References

[1] N.C. Luhmann, Jr., "Intrumentation and Techniques for Plasma Diagnostics: An Overview," *Infrared and Millimeter Waves*, vol. 2, Chap. 1, K.J. Button, ed., Academic Press, Inc., New York, 1979.

[2] T.G. Phillips, D.B. Rutledge, "Superconducting Tunnel Detectors in Radio Astronomy," *Scientific American* vol. 254, pp. 96–102, 1986.

[3] J.C. Wiltse, "Introduction and Overview of Millimeter Waves," *Infrared and Millimeter Waves*, vol. 4, Chap. 1, K.J. Button, ed., Academic Press, Inc., New York, 1981.

[4] G. Kantorowicz, P. Palluel, "Backward Wave Oscillators," *Infrared and Millimeter Waves*, vol. 1, Chap. 4, K.J. Button, ed., Academic Press, Inc., New York, 1979.

[5] H. Bierman, "Microwave Tube Design Efforts Yield Steady Performance Improvements," *Microwave J.*, pp. 52–73, June 1988.

[6] J. W. Hansen, "US TWT's from 1 to 100 GHz," *Microwave J.*, pp. 179–193, 1989 State of the Art Reference.

[7] T.A. DeTemple. "Pulsed Optically Pumped Far Infrared Lasers," *Infrared and Millimeter Waves*, vol. 1, Chap. 3, K.J. Button, ed., Academic Press, Inc., New York, 1979.

[8] K.J. Sleger, R.H. Abrams, Jr., R.K. Parker, "Trends in Solid-State Microwave and Millimeter-Wave Technology," *IEEE MTT-S Newsletter,* no. 127, pp. 11-14, Fall 1990.

[9] Y.C. Shih, H.J. Kuno, "Solid-State Sources from 1 to 100 GHz," *Microwave J.*, pp. 145–161, 1989 State of the Art Reference.

[10] T.B. Ramachandran, "Gallium Arsenide Power Sources," *Microwave J.*, pp. 91–107, 1990 State of the Art Reference.

[11] E.R. Brown, T.C.L.G. Sollner, C.D. Parker, W.D. Goodhue, C.L. Chen, "Oscillations up to 420 GHz in *GaAs/AlAs* Resonant-Tunneling Diodes," *Appl. Phys. Lett.*, vol. 49, pp. 1777–1779, October 1989.

[12] S.P Benz, C.J. Burroughs, "Coherent Emission from Two-Dimensional Josephson Junction Arrays," *Appl. Phys. Lett.,* 58, pp. 2162–2164, May 1991.

[13] M.Y. Kao, P.M. Smith, P.Ho, P.C. Chao, K.H.G. Duh, A.A. Jabra, J.M. Ballingall, "Very High Power-Added Efficiency and Low-Noise 0.15-μm Gate-Length Pseudomorphic HEMT's," *IEEE Electron Device Lett.,* EDL-10, pp. 580–582, December 1989.

[14] C.A. Liechti, "High-Speed Transistors: Directions for the 1990's," *Microwave J.* pp. 165–177, 1989 State of the Art Reference.

[15] J.A. Higgins, "GaAs Heterojunction Bipolar Transistors: A Second Generation Microwave Power Amplifier Transistor," *Microwave J.*, pp. 176–194, May 1991.

[16] K. Chang, C. Sun, "Millimeter-Wave Power Combining Techniques," *IEEE Trans. Microwave Theory Tech.,* MTT-31, pp. 91–107, February 1983.

[17] K. Kurokawa, "The Single-Cavity Multiple-Device Oscillator," *IEEE Trans. Microwave Theory Tech.,* MTT-19, pp. 793–801, October 1971.

[18] J.W. Mink, "Quasi-Optical Power Combining of Solid-State Millimeter-Wave Sources," *IEEE Trans. Microwave Theory Tech.,* MTT-34, pp. 273–279, February 1986.

[19] L. Wandinger, V. Nalbandian, "Millimeter-Wave Power Combiner Using Quasi-Optical Techniques," *IEEE Trans. Microwave Theory Tech.,* MTT-31, pp. 189–193, February 1983.

[20] K.D. Stephan, S.L. Young, S.C. Wong, "Microstrip Circuit Applications of High-Q Open Microwave Resonators," *IEEE Trans. Microwave Theory Tech.,* MTT-36, pp. 1319–1327, Sept. 1988.

[21] S.L. Young, K.D. Stephan, "Stabilization and Power Combining of Planar Microwave Oscillators with an Open Resonator," 1987 *IEEE MTT-S International Symposium Digest,* vol. 1, pp. 185–188, Las Vegas, NV.

[22] R.A. York, R.C. Compton, "Quasi-Optical Power Combining Using Mutually Synchronized Oscillator Arrays," *IEEE Trans. Microwave Theory Tech.,* MTT-39, pp. 1000–1009, June 1991.

[23] K. Chang, K.A. Hummer, J.L. Klein, "Experiments on Injection Locking of Active Antenna Elements for Active Phased Arrays and Spatial Power Combiners," *IEEE Trans. Microwave Theory Tech.,* MTT-37, pp. 1078–1084, July 1989.

[24] A. Mortazawi, T. Itoh, "A Periodic Second Harmonic Spatial Power Combining Oscillator," 1990 *IEEE MTT-S International Symposium Digest,* vol. 3, pp. 1213–1216, Dallas, TX.

[25] J. Birkeland and T. Itoh, "A 16-Element Quasi-Optical FET Oscillator Power-Combining Array with External Injection Locking," *submitted to the IEEE Trans. Microwave Theory Tech.,* June 1991.

[26] Z.B. Popović, M. Kim, D.B. Rutledge, "Grid Oscillators," *Int. J. Infrared and Millimeter Waves,* vol. 9, no. 7, pp. 647–654, 1988.

Chapter 2

EMF Analysis for Planar Grids

Planar periodic structures have long been important components for infrared and millimeter-wave applications. A periodic array, or grid, of conductors acts as a frequency selective reflector or transmitter for incident plane waves. These grids are used in quasi-optical systems as filters [1], artificial dielectrics [2], beam-splitters [3], and output couplers for lasers [4]. More recently, attention has turned to structures based on integrating solid-state devices into periodic grids. Rutledge and Schwarz developed a multi-mode detector array using a grid of microbolometers [5]. Lam *et al.* built a monolithic Schottky diode-grid phase shifter at 94 GHz [6]. Using packaged beam-lead diodes mounted in a bow-tie grid, Hacker *et al.* demonstrated a quasi-optical mixer [7]. Grids containing active solid-state devices have also been investigated for use as oscillators and amplifiers [8-10].

To reliably design systems made of quasi-optical components, it is essential to characterize the grids' electromagnetic properties. Scattering from periodic structures can be determined rigorously by invoking Floquet's theorem and using the method of moments [11-14]. A drawback of this approach, however, is that a relatively complicated set of equations is generated which must be solved numerically. Other numerical techniques such as the finite element method [15] or conjugate gradient method [16] use an iterative approach which may require large amounts of computer time. The difficulties associated with these rigorous analysis techniques when applied to periodic grids have made approximate

methods based on equivalent circuit models a convenient alternative [17].

One analysis technique that is useful for determining the equivalent circuit models for periodic grids is the induced EMF method. This method was first introduced by Brillouin in 1922 [18] and later developed by Carter [19]. The EMF method was originally used as a means for calculating the self-impedance of various antennas. It involves the use of Poynting's Theorem to find an expression for the driving-point impedance of a radiating structure. Tai applied the EMF method to find the input impedance of a biconical antenna [20] and a nice treatment applying the method to a center-fed dipole is given by Elliot [21]. Eisenhart and Khan [22] later extended the technique to waveguides and used it to derive the impedance of a waveguide mounting structure.

2.1 Outline of the Method

Application of the EMF method relies on knowing how the currents on a given radiating structure are distributed. As a result, the EMF method is primarily used for simple configurations on which the current distribution can be assumed with reasonable accuracy. The relation between an impressed current, $\mathbf{J}(\mathbf{r})$, and the resulting electric field, $\mathbf{E}(\mathbf{r})$, is given by the inhomogeneous wave equation

$$\nabla \times \nabla \times \mathbf{E}(\mathbf{r}) - k^2 \mathbf{E}(\mathbf{r}) = -j\omega\mu \mathbf{J}(\mathbf{r}), \tag{2.1}$$

where $k = \omega\sqrt{\mu\epsilon}$. The solution of this equation determines the fields produced by the currents on a radiating structure. Usually, this involves the dyadic Green's function, $\overline{\mathrm{G}}(\mathbf{r}|\mathbf{r}')$, for the structure. The solution is given by

$$\mathbf{E}(\mathbf{r}) = -j\omega\mu \int_V \overline{\mathrm{G}}(\mathbf{r}|\mathbf{r}') \cdot \mathbf{J}(\mathbf{r}')\, dv', \tag{2.2}$$

where the primed coordinates denote the region containing the impressed current distribution.

Once a current distribution is assumed and the resulting fields found from equation (2.2), Poynting's Theorem is applied to determine the power radiated. Poynting's Theorem for phasors is normally stated as

$$\oint_S \mathbf{E} \times \mathbf{H}^* \cdot d\mathbf{s} = -\int_V \mathbf{E} \cdot \mathbf{J}^* dV - j\omega \int_V (\mathbf{H}^* \cdot \mathbf{B} - \mathbf{E} \cdot \mathbf{D}^*) dV. \tag{2.3}$$

In equation (2.3) all quantities are RMS values. The term on the left is interpreted as the average power carried by the fields across the closed surface S. The first term on the right represents the power loss resulting from the flow of electric currents. This is normally associated with the ohmic losses in the system. The final term on the right involves the energy stored in the electric and magnetic fields and can be thought of as the reactive power flowing back and forth between the fields within the volume enclosed by S. When applying the EMF method, equation (2.3) is usually rearranged and put in the following form :

$$-\int_V \mathbf{E} \cdot \mathbf{J}^* dV = \oint_S \mathbf{E} \times \mathbf{H}^* \cdot d\mathbf{s} + j\omega \int_V (\mathbf{H}^* \cdot \mathbf{B} - \mathbf{E} \cdot \mathbf{D}^*) dV. \tag{2.4}$$

The right side of this equation represents the total complex power radiated from within volume V. This includes the reactive power stored in the fields as well as that radiated across S. The total complex power can be determined by evaluating the left side of equation (2.4). For the EMF method, the driving-point impedance, Z, is calculated by equating the power delivered to Z with the total complex power radiated. As a result, the impedance is given by

$$Z = -\frac{1}{|\ I\ |^2} \int_V \mathbf{E}(\mathbf{r}) \cdot \mathbf{J}^*(\mathbf{r})\ dV, \tag{2.5}$$

where | I | is the magnitude of the assumed current distribution at the feed point.

2.2 Equivalent Waveguide

Finding the embedding impedance for solid-state devices integrated into a periodic grid is similar to determining the input impedance for an antenna

or waveguide mounting structure. The general task of calculating the driving-point impedance for devices in a finite grid is formidable. Complications arise from the unknown behavior of the field at the grid edges. In addition, each device in the array will couple to all other devices through the radiated fields. Even grids of moderate size generate a large number of unknowns which can make analysis exceedingly difficult. To make the problem more tractable, it is usually assumed that the grid is infinite in extent. Under this approximation, edge effects are ignored. The problem can be simplified further if the grid has internal symmetries that can be exploited.

For many grid structures, it is common to find planes of symmetry which leave the grid unchanged with respect to reflection. The simplification that results from this particular symmetry is illustrated in Fig. 2.1. Each cell of the grid in Fig. 2.1 is assumed to contain an identical AC current source. Furthermore, it is assumed that these current sources are locked to a single phase. This situation represents an array of phase-locked oscillators which is the basis for a quasi-optical power-combining grid. Symmetry planes which run horizontally can be replaced with electric walls. This results because identical currents flow above and below these planes, causing cancellation of the tangential electric field. Similarly, vertical symmetry planes can be replaced with magnetic walls. Once again, these arise from image currents. In this way, an infinite grid of phase-locked sources can be represented by an equivalent waveguide. The equivalent waveguide has electric walls on the top and bottom and magnetic walls on the sides. It should be noted that this equivalent waveguide representation is valid whenever a TEM wave is radiated from or incident on the grid. A plane wave incident from the z-direction with the electric field polarized along the y-axis will induce currents on the grid surface. As before, these currents will be in phase allowing the grid to be represented with an equivalent waveguide.

Planar periodic grids are well suited to the EMF method if the grid struc-

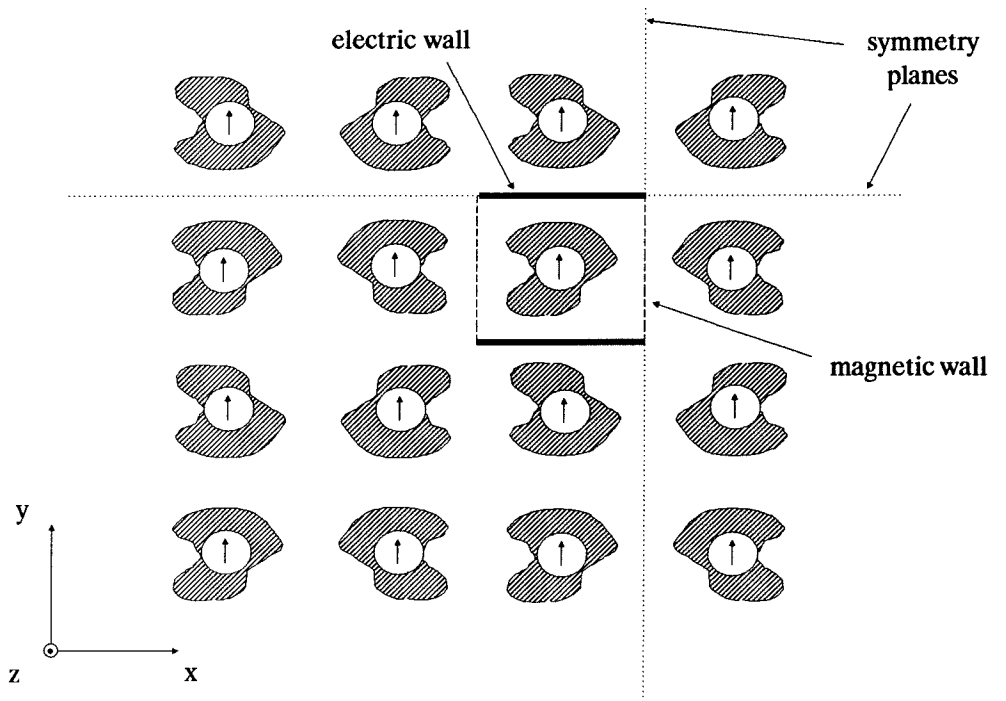

Figure 2.1 Schematic of a planar grid with reflection symmetry. Two symmetry planes are shown with dotted lines. If each cell is excited with an identical source, then horizontal symmetry planes can be replaced with electric walls and vertical symmetry planes with magnetic walls.

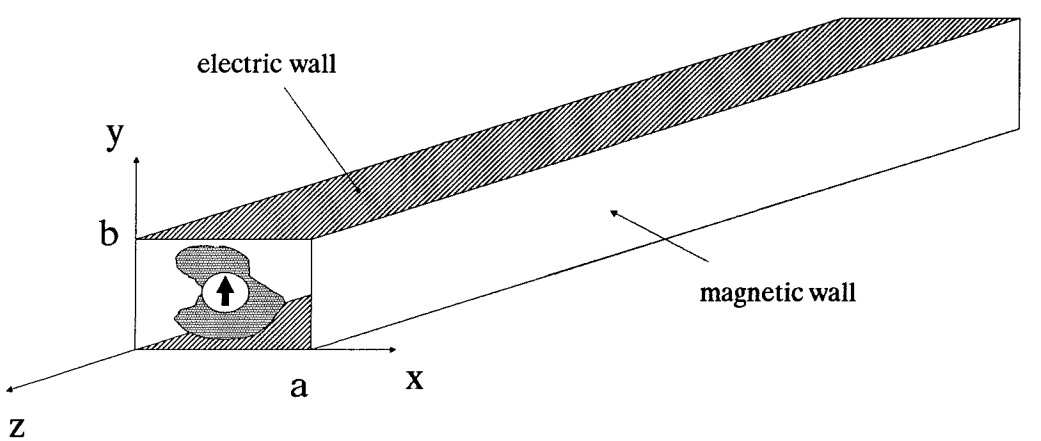

Figure 2.2 The planar grid equivalent waveguide. The waveguide has electric walls on top and bottom and magnetic walls on the sides.

ture has a simple symmetric geometry and the periodicity is smaller than a wavelength. An EMF analysis is applied to the equivalent waveguide to find the grid embedding impedance. This embedding impedance may be represented as a transmission-line circuit which describes the coupling between a device placed in the grid and a TEM wave.

Given an impressed current, equation (2.2) can be used to determine the electric field excited in the equivalent waveguide. A different approach is to expand the field in terms of the waveguide modes. A current source placed at a waveguide feed will, in general, excite all possible waveguide modes and the total field will be a superposition of these modes. They are found by solving the Helmholtz equation,

$$\nabla^2 \mathbf{E}(\mathbf{r}) = k^2 \, \mathbf{E}(\mathbf{r}) \tag{2.6}$$

subject to the waveguide boundary conditions. Consider the grid equivalent waveguide shown in Fig. 2.2. Traveling waves propagate along the z-axis and are characterized by a propagation vector k_z. The waveguide modes are classified as TEM, TM, or TE depending on which field components lie along the direction of propagation. For a wave propagating in the $+z$ direction, the TEM field components are given by

$$\mathbf{E}(\mathbf{r}) = \mathrm{E}\ \hat{y}, \qquad \mathbf{H}(\mathbf{r}) = -\sqrt{\frac{\epsilon}{\mu}}\mathrm{E}\ \hat{x} \tag{2.7}$$

where E is a constant. The TM field components can be written as

$$\begin{aligned}
\mathrm{E}_z &= \mathrm{E}_0 \cos(k_x x) \sin(k_y y) \\
\mathrm{E}_x &= j\frac{k_z}{k_c^2}\, \mathrm{E}_0 k_x \sin(k_x x) \sin(k_y y) \\
\mathrm{E}_y &= -j\frac{k_z}{k_c^2}\, \mathrm{E}_0 k_y \cos(k_x x) \cos(k_y y) \\
\mathrm{H}_x &= \frac{j\omega\epsilon}{k_c^2}\, \mathrm{E}_0 k_y \cos(k_x x) \cos(k_y y) \\
\mathrm{H}_y &= \frac{j\omega\epsilon}{k_c^2}\, \mathrm{E}_0 k_x \sin(k_x x) \sin(k_y y).
\end{aligned} \tag{2.8}$$

Similarly, the TE field components are given by

$$\begin{aligned}
\mathrm{H}_z &= \mathrm{H}_0 \sin(k_x x) \cos(k_y y) \\
\mathrm{H}_x &= -j \frac{k_z}{k_c^2} \mathrm{H}_0 k_x \cos(k_x x) \cos(k_y y) \\
\mathrm{H}_y &= j \frac{k_z}{k_c^2} \mathrm{H}_0 k_y \sin(k_x x) \sin(k_y y) \\
\mathrm{E}_x &= \frac{j\omega\mu}{k_c^2} \mathrm{H}_0 k_y \sin(k_x x) \sin(k_y y) \\
\mathrm{E}_y &= \frac{j\omega\mu}{k_c^2} \mathrm{H}_0 k_x \cos(k_x x) \cos(k_y y),
\end{aligned} \tag{2.9}$$

where $k_x = \mathrm{m}\pi/\mathrm{a}$, $k_y = \mathrm{n}\pi/\mathrm{b}$, and $k_c^2 = k_x^2 + k_y^2$ with m and n being integers. E_0 and H_0 are constant amplitude factors and a propagation factor of $e^{j(\omega t - k_z z)}$ has been assumed.

The following sections present the EMF solution for the planar grid equivalent waveguide. General expressions for the embedding impedance are derived in terms of a waveguide modal expansion. The cases of waveguide excitation with electric sources and magnetic sources are considered separately.

2.3 Electric Sources

In this section, we consider a planar grid equivalent waveguide which is excited with an electric current. It is convenient to define a set of orthonormal vectors which are used to expand the radiated field. This basis is constructed from the transverse electric field components given in equations (2.7)-(2.9). A unit TEM vector can be defined as

$$\hat{w} = \frac{1}{\sqrt{\mathrm{ab}}} \hat{y}. \tag{2.10}$$

Similarly, we define a unit TM vector :

$$\hat{u}_{\mathrm{mn}} = \sqrt{\frac{\epsilon_{\mathrm{m0}}\epsilon_{\mathrm{0n}}}{\mathrm{ab}k_c^2}} \left\{ k_x \sin(k_x x)\sin(k_y y)\hat{x} - k_y \cos(k_x x)\cos(k_y y)\hat{y} \right\} \tag{2.11}$$

and a unit TE vector :

$$\hat{v}_{\mathrm{mn}} = \sqrt{\frac{\epsilon_{\mathrm{m0}}\epsilon_{\mathrm{0n}}}{\mathrm{ab}k_{\mathrm{c}}^2}}\left\{k_y \sin(k_x x)\sin(k_y y)\hat{x} + k_x \cos(k_x x)\cos(k_y y)\hat{y}\right\}. \tag{2.12}$$

The vectors are normalized so that the inner product of any two is given by

$$\langle \hat{u}^l_{\mathrm{mn}} | \hat{u}^k_{\mathrm{m'n'}} \rangle = \int_0^{\mathrm{a}} \int_0^{\mathrm{b}} (\hat{u}^l_{\mathrm{mn}})^* \cdot \hat{u}^k_{\mathrm{m'n'}}\, dxdy = \delta_{\mathrm{mm'}}\delta_{\mathrm{nn'}}\delta_{kl}, \tag{2.13}$$

where l and k denote the mode classification of TEM, TE, or TM and δ is the Kronecker delta. These vectors are used in an expansion to represent the transverse electric field in the equivalent waveguide as

$$\mathbf{E}_{xy} = e_0\hat{w} + \sum_{\mathrm{m,n}} e^{\mathrm{TM}}_{\mathrm{mn}}\, \hat{u}_{\mathrm{mn}} + \sum_{\mathrm{m,n}} e^{\mathrm{TE}}_{\mathrm{mn}}\, \hat{v}_{\mathrm{mn}}, \tag{2.14}$$

where $e_0, e^{\mathrm{TM}}_{\mathrm{mn}}$, and $e^{\mathrm{TE}}_{\mathrm{mn}}$ are unknown coefficients. The summations are carried out over all waveguide modes. In this expansion, the z-component of the electric field has been neglected since we assume that currents flow only in the xy-plane. The impressed electric current, $\mathbf{J}_{xy}$, may also be written as a sum over the basis vectors

$$\mathbf{J}_{xy} = j_0\hat{w} + \sum_{\mathrm{m,n}} j^{\mathrm{TM}}_{\mathrm{mn}}\, \hat{u}_{\mathrm{mn}} + \sum_{\mathrm{m,n}} j^{\mathrm{TE}}_{\mathrm{mn}}\, \hat{v}_{\mathrm{mn}}, \tag{2.15}$$

where expansion coefficients j_0, $j^{\mathrm{TM}}_{\mathrm{mn}}$, and $j^{\mathrm{TE}}_{\mathrm{mn}}$ are determined by assuming a current distribution and evaluating the inner product $\langle \mathbf{J}_{xy} | \hat{u}^l_{\mathrm{mn}} \rangle$. We can relate the expressions for $\mathbf{E}_{xy}$ and $\mathbf{J}_{xy}$ by applying Maxwell's boundary conditions. The tangential components of $\mathbf{H}$ are discontinuous across a given boundary on which a surface current $\mathbf{J}_{\mathrm{s}}$ flows. We can express this as

$$\hat{n} \times \left(\mathbf{H}^+ - \mathbf{H}^-\right) = \mathbf{J}_{\mathrm{s}}, \tag{2.16}$$

where $\hat{n}$ represents a unit vector normal to the surface. The superscripts $+$ and $-$ represent the $\mathbf{H}$-field components above and below the given surface. For the

equivalent waveguide of Fig. 2.2, we assume that current flows only in the $z = 0$ plane. As a result, equation (2.16) may be rewritten as

$$\mathbf{J}_{xy} \times \hat{z} = \left(\mathbf{H}^{+} - \mathbf{H}^{-}\right)_{xy}. \tag{2.17}$$

The subscript xy denotes the component of $\mathbf{H}$ perpendicular to the z-axis. Equations (2.17) and (2.15) can be combined to find an expression for the discontinuity in the $\mathbf{H}$-field. This discontinuity is given by

$$\left(\mathbf{H}^{+} - \mathbf{H}^{-}\right)_{xy} = j_0\ (\hat{w} \times \hat{z}) + \sum_{\mathrm{m,n}} j_{\mathrm{mn}}^{\mathrm{TM}}\ (\hat{u}_{\mathrm{mn}} \times \hat{z}) + \sum_{\mathrm{m,n}} j_{\mathrm{mn}}^{\mathrm{TE}}\ (\hat{v}_{\mathrm{mn}} \times \hat{z}). \tag{2.18}$$

We can relate the transverse components of the $\mathbf{H}$-field with those of the $\mathbf{E}$-field by the characteristic mode admittances, Y_{mn}^{l}:

$$\mathbf{H}_{mn}^{(l)+} = -\mathrm{Y}_{mn}^{(l)+}\ (\mathbf{E}_{mn}^{(l)+} \times \hat{z}) \tag{2.19}$$

$$\mathbf{H}_{\mathrm{mn}}^{(l)-} = \mathrm{Y}_{\mathrm{mn}}^{(l)-}\ (\mathbf{E}_{\mathrm{mn}}^{(l)-} \times \hat{z}). \tag{2.20}$$

In equations (2.19) and (2.20), l refers to the mode classification (TEM, TM, or TE) and the superscripts $+$ and $-$ indicate waves propagating in the $+z$ and $-z$ directions, respectively. The characteristic admittances for the waveguide modes may be expressed as follows:

$$\begin{aligned} Y_0^{\mathrm{TEM}} &= \sqrt{\frac{\epsilon}{\mu}} \\ Y_{\mathrm{mn}}^{\mathrm{TM}} &= \frac{\omega\epsilon}{k_z} \\ Y_{\mathrm{mn}}^{\mathrm{TE}} &= \frac{k_z}{\omega\mu}, \end{aligned} \tag{2.21}$$

where k_z is the propagation constant and is given by :

$$k_z = \sqrt{\omega^2\mu\epsilon - \left(\frac{\mathrm{m}\pi}{\mathrm{a}}\right)^2 - \left(\frac{\mathrm{n}\pi}{\mathrm{b}}\right)^2}. \tag{2.22}$$

Maxwell's boundary conditions also require the tangential electric field be continuous. This means that the transverse $\mathbf{E}$-field for waves propagating in the $+z$

and $-z$ directions must match at the $z = 0$ plane. Using the expression for the electric field given in (2.14) and equations (2.19) and (2.20), we can find modal expansions for $\mathbf{H}^+$ and $\mathbf{H}^-$. For waves propagating in the $+z$ direction, it is necessary to use the mode admittances looking in that direction. Likewise, for waves propagating in the $-z$ direction, we use $Y_{mn}^{(l)-}$. Comparison with equation (2.18) allows us to relate the electric field and current expansion coefficients :

$$\begin{aligned} j_0 &= -\left(Y_0^{\mathrm{TEM}+} + Y_0^{\mathrm{TEM}-}\right) e_0 \\ j_{mn}^{\mathrm{TM}} &= -\left(Y_{mn}^{\mathrm{TM}+} + Y_{mn}^{\mathrm{TM}-}\right) e_{mn}^{\mathrm{TM}} \\ j_{mn}^{\mathrm{TE}} &= -\left(Y_{mn}^{\mathrm{TE}+} + Y_{mn}^{\mathrm{TE}-}\right) e_{mn}^{\mathrm{TE}}. \end{aligned} \tag{2.23}$$

Equations (2.23) show that the expansion coefficients are related by the parallel combination of the mode admittances looking in the $+z$ and $-z$ directions. Using these relations in equation (2.14) and applying Poynting's Theorem as stated in equation (2.5), we find the driving-point impedance for the radiating structure. This is given by

$$\begin{aligned} Z = \frac{1}{|\,I\,|^2}\Big\{ &\left(Z_0^{\mathrm{TEM}+} \parallel Z_0^{\mathrm{TEM}-}\right) |\, j_0\,|^2 + \sum_{m,n} |\, j_{mn}^{\mathrm{TM}}\,|^2 \left(Z_{mn}^{\mathrm{TM}+} \parallel Z_{mn}^{\mathrm{TM}-}\right). \\ &+ \sum_{m,n} |\, j_{mn}^{\mathrm{TE}}\,|^2 \left(Z_{mn}^{\mathrm{TE}+} \parallel Z_{mn}^{\mathrm{TE}-}\right)\Big\}. \end{aligned} \tag{2.24}$$

In equation (2.24), the $\parallel$ symbol indicates the impedances are to be combined in parallel. To solve a specific problem, an electric current distribution is assumed. From this current distribution, the expansion coefficients j_0, j_{mn}^{TM}, and j_{mn}^{TE} are determined. Once this is done, equation (2.24) can be evaluated to find the driving-point impedance.

An example to illustrate the application of the preceding analysis is given in Fig. 2.3(a). This grid consists of a series of equally spaced vertical metal strips. The grid unit cell is shown in Fig. 2.3(b). A current distribution is assumed on the strip and then used to determine the expansion coefficients. If the unit cell

dimensions are smaller than a wavelength, we may assume that the current is uniform along and across the strip :

$$\mathbf{J}_{xy} = \begin{cases} \mathrm{I_0/w}, & \text{if } \frac{\mathrm{a-w}}{2} \leq x \leq \frac{\mathrm{a+w}}{2}; \\ 0, & \text{otherwise.} \end{cases} \hat{y}. \tag{2.25}$$

With this distribution, the current expansion coefficients become :

$$\begin{aligned} j_0 &= \sqrt{\frac{\mathrm{b}}{\mathrm{a}}}\,\mathrm{I_0} \\ j_{\mathrm{mn}}^{\mathrm{TM}} &= 0 \\ j_{\mathrm{mn}}^{\mathrm{TE}} &= \sqrt{\frac{2\mathrm{b}}{\mathrm{a}}}\,\mathrm{I_0}\,\cos(\frac{\mathrm{m}\pi}{2})\,\mathrm{sinc}(\frac{\mathrm{m}\pi\mathrm{w}}{2\mathrm{a}}), \end{aligned} \tag{2.26}$$

where we define the sinc function as

$$\mathrm{sinc}(x) \;=\; \frac{\sin(x)}{x}. \tag{2.27}$$

Inserting these expressions into equation (2.24) , we find a formula for the impedance of the grid :

$$Z \;=\; \frac{\mathrm{b}}{\mathrm{a}}\,(Z_0^{\mathrm{TEM+}} \parallel Z_0^{\mathrm{TEM-}}) + \tag{2.28}$$

$$\frac{2\mathrm{b}}{\mathrm{a}} \sum_{\mathrm{m=1}}^{\infty} \cos^2(\frac{\mathrm{m}\pi}{2})\,\mathrm{sinc}^2(\frac{\mathrm{m}\pi\mathrm{w}}{2\mathrm{a}})(Z_{\mathrm{m0}}^{\mathrm{TE+}} \parallel Z_{\mathrm{m0}}^{\mathrm{TE-}}).$$

The grid impedance consists of two distinct terms which are added in series. The first term is a parallel combination of TEM mode impedances. TEM modes do not have a cutoff frequency and thus represent power propagating from the grid. These modes can be represented in the equivalent circuit model with a parallel combination of transmission lines of characteristic impedance (b/a) $Z_0^{\mathrm{TEM+}}$ and (b/a) $Z_0^{\mathrm{TEM-}}$, respectively. The second term is a sum over the waveguide TE modes. The TE mode impedances are given by $\omega\mu/k_z$. In most applications, the dimensions of the waveguide or unit cell are chosen so that all but the lowest order (TEM) mode are cutoff. As a result, the TE modes are normally evanescent,

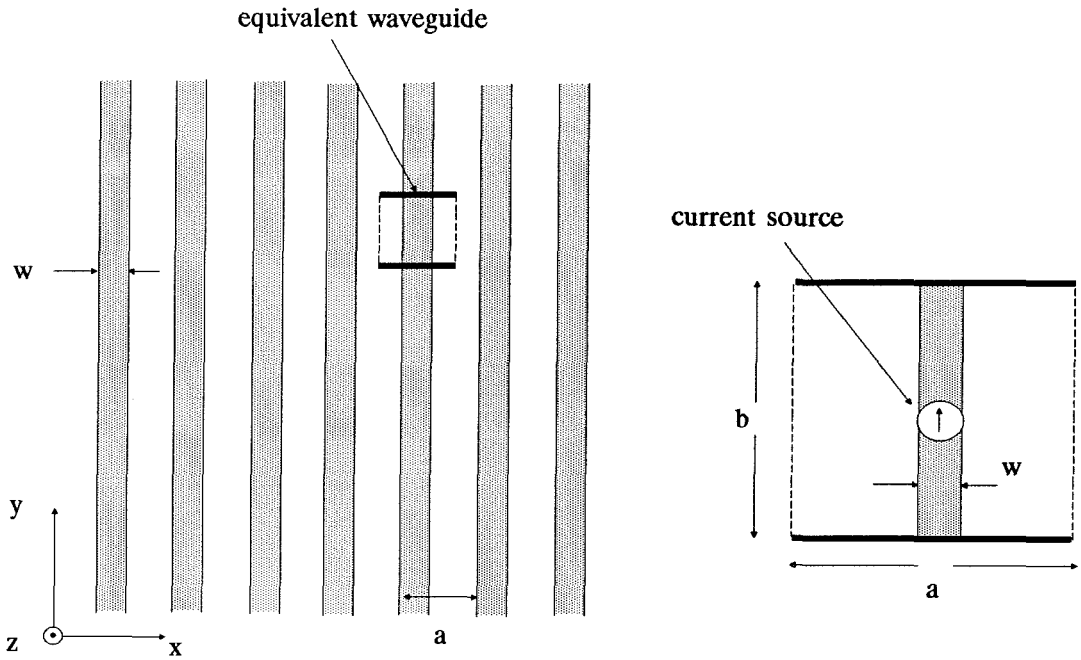

Figure 2.3 (a) A grid of vertical metal strips and (b) the resulting equivalent waveguide.

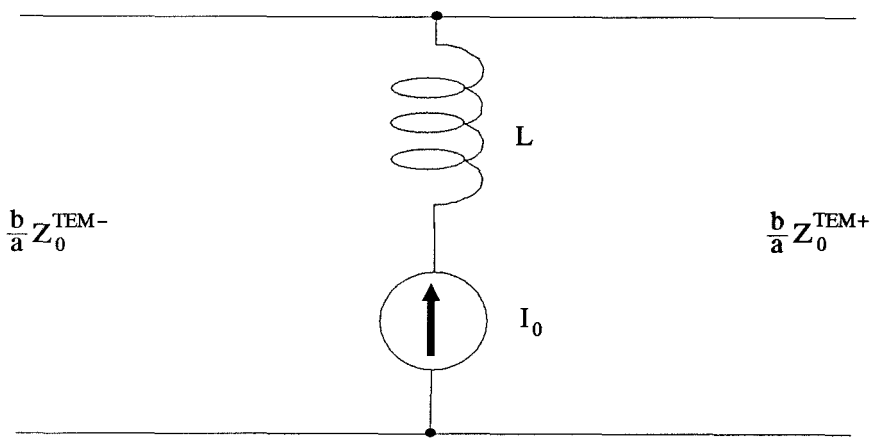

Figure 2.4 Equivalent transmission-line model for the inductive grid. The inductance is calculated by summing over the TE modes of the equivalent waveguide.

giving a reactive impedance of $j\omega\mu/|k_z|$. Evanescent TE modes are inductive and thus the second term in equation (2.28) represents an inductance in series with the current source excitation. The equivalent transmission-line model for the grid is shown in Fig. 2.4. In this model, the current source can be replaced with a short to represent a passive grid of vertical metal strips.

2.4 Magnetic Sources

Often it is more convenient to formulate the EMF solution to a problem in terms of a voltage excitation rather than a current excitation. An example of this is the grid shown in Fig. 2.5. This grid consists of an array of horizontal metal strips. It is the dual problem to the inductive grid and can be solved assuming a voltage excitation in the gaps between the metal. This voltage excitation can be represented as a magnetic current flowing between the strips.

Magnetic currents, $\mathbf{M}$, are included in Maxwell's equations by augmenting Faraday's law :

$$\nabla \times \mathbf{E} = -\mathbf{M} - j\omega\mu\mathbf{H} \tag{2.29}$$

subject to the boundary condition,

$$\left(\mathbf{E}^{+} - \mathbf{E}^{-}\right) \times \hat{n} = \mathbf{M}_{\mathrm{s}}, \tag{2.30}$$

where $\mathbf{M}_{\mathrm{s}}$ is the surface magnetic current and $\hat{n}$ is the unit vector normal to the surface. As in the case of electric current excitation, it is convenient to define a set of orthonormal vectors which are used to expand the radiated fields. These vectors are constructed from the magnetic field components in equations (2.7)-(2.9) and are given by :

$$\hat{w} = \frac{1}{\sqrt{\mathrm{ab}}}\,\hat{x}$$

$$\hat{u}_{\mathrm{mn}} = \sqrt{\frac{\epsilon_{\mathrm{m0}}\epsilon_{\mathrm{0n}}}{\mathrm{ab}k_{\mathrm{c}}^2}}\left\{\, k_y \cos(k_x x)\cos(k_y y)\hat{x} + k_x \sin(k_x x)\sin(k_y y)\hat{y}\right\} \tag{2.31}$$

$$\hat{v}_{\mathrm{mn}} = \sqrt{\frac{\epsilon_{\mathrm{m0}}\epsilon_{\mathrm{0n}}}{\mathrm{ab}k_{\mathrm{c}}^2}}\left\{\, -k_x \cos(k_x x)\cos(k_y y)\hat{x} + k_y \sin(k_x x)\sin(k_y y)\hat{y}\right\}.$$

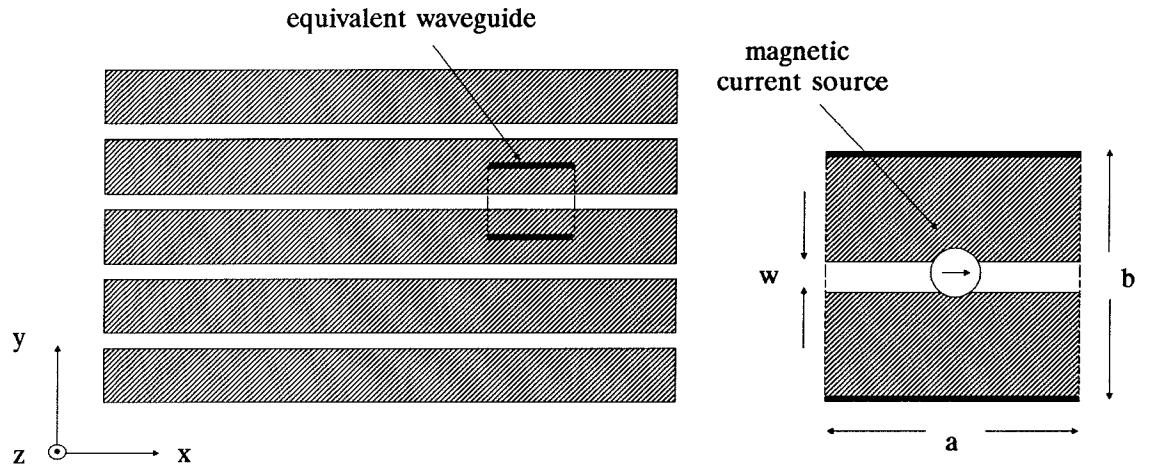

(a) (b)

Figure 2.5 (a) Schematic of a capacitive grid consisting of horizontal metal strips. (b) The equivalent waveguide for the grid with a magnetic current excitation.

As before $\hat{w}$ denotes the unit TEM vector and $\hat{u}_{\mathrm{mn}}$ and $\hat{v}_{\mathrm{mn}}$ are the unit TM and TE vectors, respectively. The magnetic field and magnetic current distribution are expanded in terms of this basis with unknown expansion coefficients :

$$\mathbf{H}_{xy} = h_0 \hat{w} + \sum_{\mathrm{m,n}} h_{\mathrm{mn}}^{\mathrm{TM}} \hat{u}_{\mathrm{mn}} + \sum_{\mathrm{m,n}} h_{\mathrm{mn}}^{\mathrm{TE}} \hat{v}_{\mathrm{mn}} \tag{2.32}$$

$$\mathbf{M}_{xy} = m_0 \hat{w} + \sum_{\mathrm{m,n}} m_{\mathrm{mn}}^{\mathrm{TM}} \hat{u}_{\mathrm{mn}} + \sum_{\mathrm{m,n}} m_{\mathrm{mn}}^{\mathrm{TE}} \hat{v}_{\mathrm{mn}}. \tag{2.33}$$

For a magnetic current excitation, the tangential magnetic field at $z = 0$ is continuous while the tangential electric field is discontinuous as given in equation (2.30). Applying the boundary condition (2.30), we find that the magnetic current and field expansion coefficients are related by :

$$\begin{aligned} m_0 &= -(Z_0^{\mathrm{TEM}+} + Z_0^{\mathrm{TEM}-})\, h_0 \\ m_{\mathrm{mn}}^{\mathrm{TM}} &= -(Z_{\mathrm{mn}}^{\mathrm{TM}+} + Z_{\mathrm{mn}}^{\mathrm{TM}-})\, h_{\mathrm{mn}}^{\mathrm{TM}} \\ m_{\mathrm{mn}}^{\mathrm{TE}} &= -(Z_{\mathrm{mn}}^{\mathrm{TE}+} + Z_{\mathrm{mn}}^{\mathrm{TE}-})\, h_{\mathrm{mn}}^{\mathrm{TE}}. \end{aligned} \tag{2.34}$$

From equation (2.34) and Poynting's Theorem, we find the driving-point admittance for the grid :

$$Y = -\frac{1}{|\mathrm{V}|^2} \int_V \mathbf{H} \cdot \mathbf{M}^* \, dV$$

$$= \frac{1}{|\mathrm{V}|^2} \{(Z_0^{\mathrm{TEM}+} + Z_0^{\mathrm{TEM}-})^{-1} |m_0|^2 + \sum_{\mathrm{m,n}} (Z_{\mathrm{mn}}^{\mathrm{TM}+} + Z_{\mathrm{mn}}^{\mathrm{TM}-})^{-1} |m_{\mathrm{mn}}^{\mathrm{TM}}|^2 \quad (2.35)$$

$$+ \sum_{\mathrm{m,n}} (Z_{\mathrm{mn}}^{\mathrm{TE}+} + Z_{\mathrm{mn}}^{\mathrm{TE}-})^{-1} |m_{\mathrm{mn}}^{\mathrm{TE}}|^2 \}.$$

An interesting feature of this equation is that the mode impedances add in series rather than parallel. This is a consequence of using a magnetic current source which requires the tangential electric field be discontinuous at $z = 0$. For a real grid, the tangential electric field is continuous at $z = 0$, which means the mode impedances should add in parallel. This can be understood by examining the relationship between an antenna and its dual and complementary structures. Dual and complimentary antennas are closely related by the Schelkunoff equivalence principle. Consider the antennas shown in Fig. 2.6. Each antenna is assumed to lie in the $z = 0$ plane. Usually, this is at the interface between two different dielectric media. For the dual antenna, magnetic current flows only on the magnetic conductor. An analogous situation exists for the complementary antenna where electric fields vanish on the electric conductor's surface. The admittance of an antenna made of electric conductors can be calculated by finding the voltage appearing across the antenna feed and dividing it into the input current:

$$Y = \frac{\mathrm{I}}{\mathrm{V}} \quad (2.36)$$

where,

$$\mathrm{V} = -\int \mathbf{E} \cdot d\mathbf{l}, \text{ and } \mathrm{I} = \oint \mathbf{H} \cdot d\mathbf{l}. \quad (2.37)$$

The input voltage is determined by integrating the electric field across the antenna feed. A dielectric interface presents no problem because the tangential

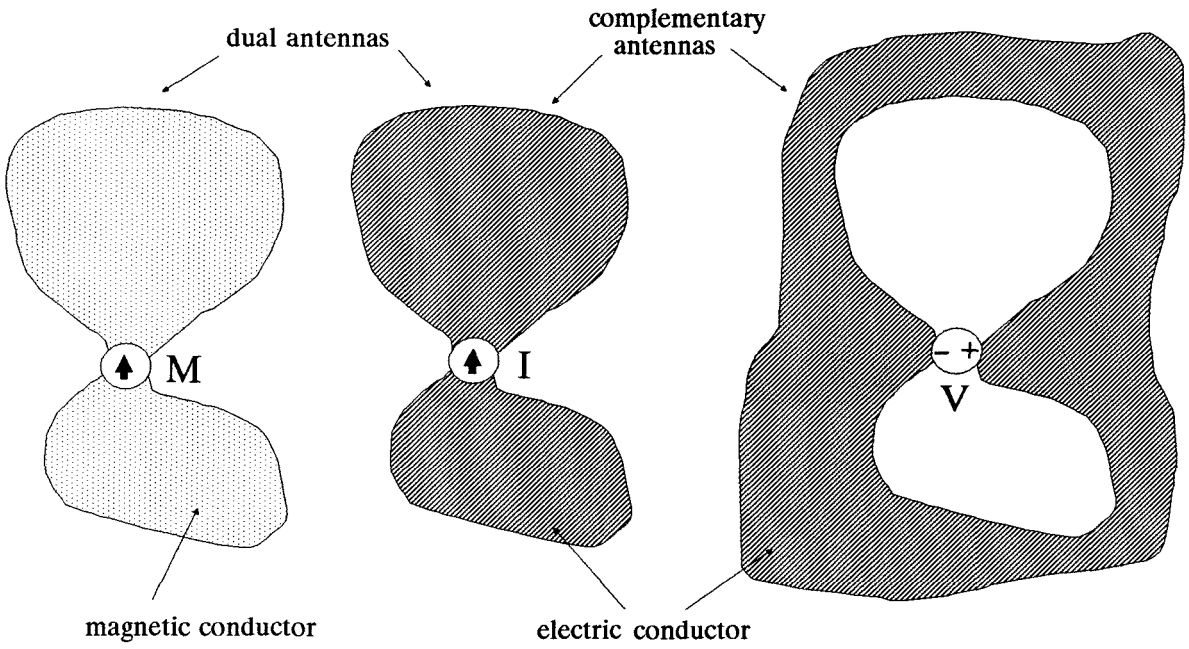

Figure 2.6 Schematic of an antenna with its dual and complement. The dual antenna is obtained by replacing electric conductors with magnetic conductors.

electric field is continuous across the boundary. The current flow at the feed is calculated by integrating the magnetic field along a loop enclosing the feed point. There will be a discontinuity in the magnetic field at the interface due to the current. Thus, the integration of $\mathbf{H}$ can be divided into a part for $z > 0$ and a part for $z < 0$:

$$\oint \mathbf{H} \cdot d\mathbf{l} = \oint_{z>0} \mathbf{H} \cdot d\mathbf{l} + \oint_{z<0} \mathbf{H} \cdot d\mathbf{l} \tag{2.38}$$

$$= I_{z>0} + I_{z<0}.$$

A constant voltage appears across the antenna feed, but different currents flow for $z > 0$ and $z < 0$. This corresponds to a parallel combination for the impedances looking in the $+z$ and $-z$ directions. A similar argument can be made for antennas made of magnetic conductor. However, in this case, the discontinuity in the electric field gives rise to different voltages across the feed for $z > 0$ and

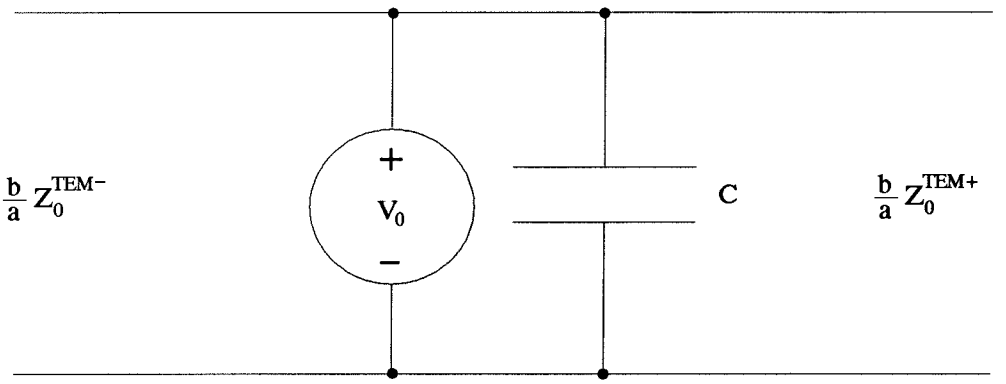

Figure 2.7 Transmission-line model for the capacitive grid.

$z < 0$. As a result, the impedances looking in the two different directions add in series. In an actual grid, there are no magnetic conductors. This means the series connections for the mode impedances in equation (2.35) should be changed to parallel connections. Hence, the admittance of the grid is given by :

$$Y = \frac{1}{|V|^2} \{(Y_0^{TEM+} + Y_0^{TEM-})|m_0|^2 + \sum_{m,n} (Y_{mn}^{TM+} + Y_{mn}^{TM-})|m_{mn}^{TM}|^2 \quad (2.39)$$

$$+ \sum_{m,n} (Y_{mn}^{TE+} + Y_{mn}^{TE-})|m_{mn}^{TE}|^2 \}.$$

We can apply this analysis to the equivalent waveguide of Fig. 2.5. A magnetic surface current is assumed in the gap and is given by :

$$M_{xy} = \begin{cases} V_0/w, & \text{if } \frac{b-w}{2} \leq y \leq \frac{b+w}{2}; \\ 0, & \text{otherwise.} \end{cases} \hat{x} \quad (2.40)$$

which results in the following expansion coefficients :

$$m_0 = \sqrt{\frac{a}{b}}\, V_0$$

$$m_{mn}^{TE} = 0 \quad (2.41)$$

$$m_{mn}^{TM} = \sqrt{\frac{2a}{b}}\, V_0\, \cos(\frac{n\pi}{2})\, \mathrm{sinc}(\frac{n\pi w}{2b}).$$

Using these coefficients in equation (2.39) gives the following expression for the grid admittance :

$$Y = \frac{a}{b}\,(Y_0^{TEM+} + Y_0^{TEM-}) + \tag{2.42}$$

$$\frac{2a}{b}\sum_{n=1}^{\infty} \cos^2(\frac{n\pi}{2})\, \mathrm{sinc}^2(\frac{n\pi w}{2b})(Y_{0n}^{TM+} + Y_{0n}^{TM-}).$$

Like the inductive grid, the input admittance consists of two terms. The first is the propagating TEM mode which is represented with a transmission-line. In parallel with this is a term consisting of a sum over the TM mode admittances. Below cutoff, these modes are capacitive and are represented by a shunt capacitor. The transmission-line model for the grid is shown in Fig. 2.7. The capacitance is calculated by adding the TM admittances looking in the forward and backward directions and summing over the modes. It is interesting to note that the capacitive grid of Fig. 2.5 is the complement of the inductive grid in Fig. 2.3. The impedances of complementary structures are related by Booker's relation [23]. As a result, the expression for the admittance of the capacitive grid can also be derived by using equation (2.28) and substituting directly into Booker's formula.

2.5 Stationary Character of the EMF Solution

The EMF method presented in this chapter is based on the principle of conservation of complex power. An expression for the driving-point impedance of a radiating structure is found by equating the complex power in the electromagnetic fields with the power delivered by a current or voltage source at the feed point. It is also possible to formulate a solution based on the Lorentz Reciprocity Theorem. The reciprocity theorem is conveniently expressed in terms reactions [24]. The reaction of field a with source b is defined as

$$\langle a, b \rangle = \int_V \mathbf{J}_b \cdot \mathbf{E}_a - \mathbf{M}_b \cdot \mathbf{H}_a \; dV. \tag{2.43}$$

Reaction is a complex quantity which has units of power. However, it is different from complex power in two respects. First, the complex conjugate of the current is used in the expression for power. Second, the reaction is defined for a source with respect to the field produced by another source. Using equation (2.43), the reciprocity theorem can be expressed as

$$\langle a, b \rangle = \langle b, a \rangle. \tag{2.44}$$

The input impedance at the feed of an antenna can be written in terms of the self-reaction of a source placed at the feed [24] :

$$Z_{\text{in}} = -\frac{\langle a, a \rangle}{\mathrm{I}^2} = -\frac{1}{\mathrm{I}^2} \int_S \mathbf{E}_a \cdot \mathbf{J}_a \, ds, \tag{2.45}$$

where I is the input current. Essentially, this expression is a statement that the input impedance is the ratio of voltage and current at the feed point. This is in contrast with the formulation based on Poynting's Theorem where the impedance is found from power considerations.

An intriguing feature of equation (2.45) is that the impedance calculated with this formula is stationary with respect to small variations in the source distribution, a. Harrington discusses this in detail [24]. The stationary character of the solution is easily shown by assuming the source distribution can be written in the following form :

$$a = c + \epsilon\chi \tag{2.46}$$

where c is the true source distribution, χ is an arbitrary error function which satisfies the boundary conditions of the problem, and ϵ is a small real parameter. The variation of the input impedance with the approximate source distribution is found by substituting equation (2.46) into (2.45) and differentiating with respect to ϵ :

$$\frac{\partial Z_{\text{in}}}{\partial \epsilon} = -\frac{1}{\mathrm{I}^2} \{\langle c, \chi \rangle + \langle \chi, c \rangle + 2\epsilon \langle \chi, \chi \rangle\}. \tag{2.47}$$

The reactions in equation (2.47) are evaluated for the region containing the antenna. For small variations about the true source distribution, we set $\epsilon = 0$. Using reciprocity, we find that

$$\frac{\partial Z_{\text{in}}}{\partial \epsilon} = -\frac{2}{\mathrm{I}^2} \langle c, \chi \rangle = 0. \tag{2.48}$$

The second equality comes from the fact that the true electric field, c is zero on the antenna's conducting surface. The only place where the electric field does not vanish is at the feed point. However, the error function, χ, is zero there. As a result, the variation of the input impedance with current distribution is zero to first order and equation (2.45) is a stationary formula. It therefore follows that a first-order approximation for the source distribution yields a second-order approximation to the input impedance.

Strictly speaking, the input impedance found from the induced EMF method is not stationary. The difference in the impedance formula for the EMF method is that the complex conjugate of the source current is used. However, if the assumed current distribution is real, the EMF method leads to an impedance identical to that found from equation (2.45) and thus gives a stationary solution.

References

[1] J.A. Arnaud, A. Pelow, "Resonant-Grid Quasi-Optical Diplexers, " *Bell Sys. Tech. J.,* vol. 54, pp. 263–283, 1975.

[2] R.E. Collin, *Field Theory of Guided Waves, 2nd ed.,* Chapter 12, IEEE Press, New York, 1991.

[3] R. Watanabe, "A Novel Polarization Independent Beam Splitter," *IEEE Trans. Microwave Theory and Tech.,* MTT-28, pp. 685–689, 1980.

[4] R. Ulrich, T.J. Bridges, M.A. Pollack, "Variable Metal Mesh Coupler for Far Infrared Lasers," *Appl. Opt.,* vol. 11, pp. 2511–2516, 1970.

[5] D.B. Rutledge, S.E. Schwarz, "Planar-Multimode Detector Arrays for Infrared and Millimeter-Wave Applications," *IEEE J. of Quantum Electronics,* QE-17, pp. 407–414, March 1981.

[6] W.W. Lam, *et al.*, "Millimeter-Wave Diode-Grid Phase Shifters," *IEEE Trans. Microwave Theory Tech.,* MTT-36, pp. 902–907, May 1988.

[7] J.B. Hacker, R.M. Weikle, II, M. Kim, M.P. De Lisio, D.B. Rutledge, "A 100-Element Planar Schottky Diode Grid Mixer," *submitted to the IEEE Trans. Microwave Theory Tech.,* June 1991.

[8] Z.B. Popović, R.M. Weikle, II, M. Kim, D.B. Rutledge, "A 100-MESFET Planar Grid Oscillator," *IEEE Trans. Microwave Theory Tech.,* MTT-39, pp. 193–200, February 1991.

[9] R.A. York, R.C. Compton, "Quasi-Optical Power Combining Using Mutually Synchronized Oscillator Arrays," *IEEE Trans. Microwave Theory Tech.,* MTT-39, pp. 1000–1009, June 1991.

[10] M. Kim, *et al.,* "A Grid Amplifier," *IEEE Microwave and Guided Wave Lett.,* vol. 1, no. 11, pp. 322–324, November 1991.

[11] S.W. Lee, "Scattering by Dielectric-Loaded Screen," *IEEE Trans. Antennas Propagat.,* AP-19, pp. 656–665, Sept. 1971.

[12] C.C. Chen, "Transmission of Microwaves Through Perforated Flat Plates," *IEEE Trans. Microwave Theory Tech.,* MTT-21, pp. 1–6, Jan. 1973.

[13] J.P. Montgomery, "Scattering by an Infinite Periodic Array of Thin Conductors on a Dielectric Sheet," *IEEE Trans. Antennas Propagat.,* AP-23, pp. 70–75, January 1975.

[14] B.J. Rubin, H.L. Bertoni,"Reflection from a Periodically Perforated Plane Using a Subsectional Current Approximation," *IEEE Trans. Antennas Propagat.,* AP-31, pp. 826–836, November 1983.

[15] "HP 85180A High-Frequency Structure Simulator," Hewlett- Packard Company, Networks Measurements Division, 1400 Foutaingrove Parkway, Santa Rosa, CA 95403, U.S.A.

[16] R. Kastner, R. Mittra, "Iterative Analysis of Finite-Sized Planar Frequency Selective Surfaces with Rectangular Patches or Perforations," *IEEE Trans. Antennas Propagat.,* AP-35, pp. 372–377, April 1987.

[17] N. Marcuvitz, *Waveguide Handbook,* Peter Peregrinus Ltd., London, 1986, pp. 280–295.

[18] L. Brillouin, "Origin of Radiation Resistance," *Radioélectricité,* 3, pp. 147–152, 1922.

[19] P.S. Carter, "Circuit Relations in Radiating Systems and Applications to Antenna Problems," *Proc. IRE,* vol. 20, pp. 1004–1041, June 1932.

[20] C.T. Tai, "A Study of the E.M.F. Method," *J. Appl. Phys.,* vol. 20, pp. 717–723, July 1949.

[21] R.S. Elliot, *Antenna Theory and Design,* Prentice-Hall, Englewood Cliffs, 1981, pp. 297–305.

[22] R.L. Eisenhart, P.J. Khan, "Theoretical and Experimental Analysis of a Waveguide Mounting Structure," *IEEE Trans. Microwave Theory Tech.,* MTT-19, pp. 706–719, August 1971.

[23] J.A. Kong, *Electromagnetic Wave Theory,* John Wiley & Sons, New York, 1986, pp. 367–371.

[24] R.F. Harrington, *Time-Harmonic Electromagnetic Fields,* McGraw-Hill Inc. New York, 1961, pp. 340–355.

Chapter 3

Planar Grid Transmission-Line Models

An attractive feature of planar periodic grids is their capacity to accommodate solid-state devices. In addition, the performance of the grids can be understood in terms of an equivalent circuit model. In the previous chapter, a method for obtaining these models for geometrically simple grids was presented. Inductive and capacitive grids were analyzed using the induced EMF method and the corresponding transmission-line models derived. While these grids are suitable as filters and polarizers, they are not very useful structures to integrate with solid-state devices.

A variety of structures such as rectangular slot arrays and bow-tie grids are amenable to two-terminal devices. Often, the analysis of these grid configurations require the use of both electric and magnetic sources to find a complete transmission-line model. This introduces an additional complication in the EMF analysis. Furthermore, transistor arrays present the problem of how to deal with the third device terminal. In the following sections, grid configurations which are compatible with two- and three-terminal device integration are examined.

3.1 Rectangular Slot Arrays

One grid configuration which readily permits integration of two-terminal devices is the rectangular slot array. A schematic of the grid is shown in Fig. 3.1. This structure has been the building block for several previous quasi-optical grids including a multi-mode detector array [1], a Schottky diode grid phase-shifter [2], and a diode-grid multiplier [3]. The equivalent waveguide for the grid, shown in Fig. 3.2, is closely related to the waveguide mounting structure investigated by Eisenhart and Khan [4] and may be analyzed using the same method. The main difference is the unit cell is a slot configuration which is most conveniently analyzed using duality. For the analysis, we assume a current I_0 flows along the vertical metal strips. We also assume this current is uniform and thus specifies an "aperture" magnetic field, H_A. The "aperture" refers to the vertical metal strip in the unit cell and is dual to the gap or aperture in Eisenhart and Khan's waveguide post. If the aperture field is uniform along the y-direction, it can be written as :

$$H_A = -\frac{I_0}{g} \begin{cases} 1, & \text{if } 0 \le x \le g \\ 0, & \text{otherwise.} \end{cases} \hat{x} \tag{3.1}$$

The spatial dependence of H_A can be expressed in terms of a Fourier series expansion :

$$H_A(x,y) = -\frac{I_0}{a} \sum_{m=0}^{\infty} \epsilon_{m0} \, \mathrm{sinc}(\frac{m\pi g}{a}) \cos(\frac{m\pi x}{a}) \, \hat{x}. \tag{3.2}$$

H_A serves as an excitation for the grid unit cell and is analogous to a uniform electric field in a waveguide post feed. The aperture magnetic field gives rise to a magnetic current, $\mathbf{M}$, which flows in the x-direction as shown in Fig. 3.2. Making the assumption that the magnetic current is uniform across the gap, we may write $\mathbf{M}$ as :

$$\mathbf{M}(x,y) = \frac{V_0}{w} \, u(x) \, u(y) \, \delta(z) \, \hat{x}, \tag{3.3}$$

where the spatial dependence of $\mathbf{M}$ on x is described by $u(x)$, $\delta(z)$ is the Dirac

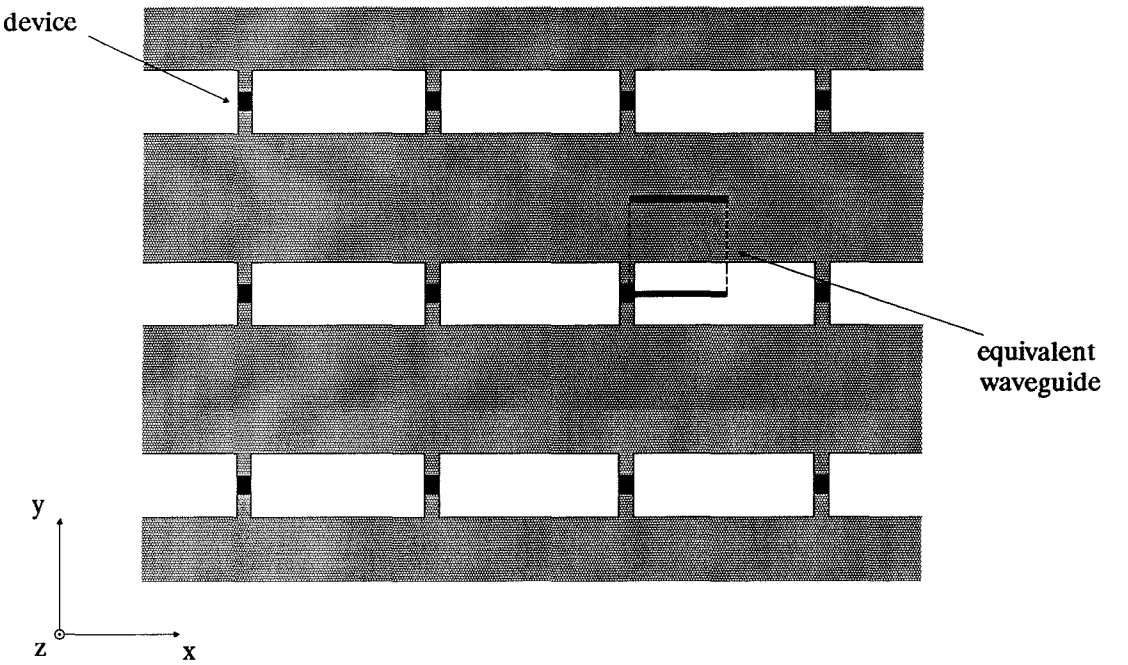

Figure 3.1 Schematic of the rectangular slot array. Devices are embedded in the vertical leads and DC bias is fed along the horizontal metal strips.

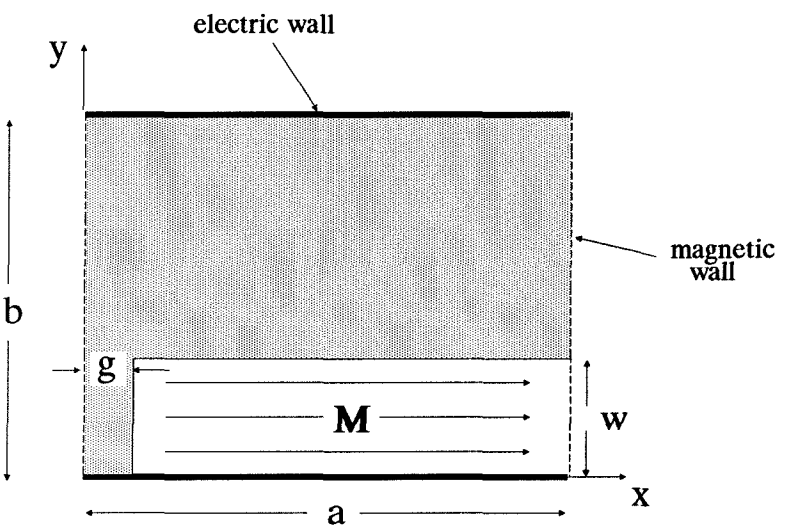

Figure 3.2 Equivalent waveguide for the slot array. An aperture magnetic field, $H_A\,\hat{x}$, assumed on the metal strip drives a magnetic current, **M**, as shown.

delta function, and $u(y)$ is given by :

$$u(y) = \begin{cases} 1, & \text{for } 0 \leq y \leq \mathrm{w}; \\ 0, & \text{otherwise.} \end{cases} \tag{3.4}$$

The power generated by the aperture field, $\mathrm{H_A}$, is evaluated by using Poynting's Theorem :

$$P = -\int_0^{\mathrm{a}} \int_0^{\mathrm{b}} \mathbf{H_A} \cdot \mathbf{M}^* \, dxdy \tag{3.5}$$

$$= \frac{\mathrm{I_0 V_0}}{\mathrm{a}} \sum_{\mathrm{m}=0}^{\infty} \epsilon_{\mathrm{m0}} \, \mathrm{sinc}(\frac{\mathrm{m}\pi \mathrm{g}}{\mathrm{a}}) \int_0^{\mathrm{a}} u(x) \cos(\frac{\mathrm{m}\pi x}{\mathrm{a}}) \, dx.$$

From equation (3.5), we see that the total power generated is a summation of individual power harmonic terms, $\mathrm{P_m}$, and may be expressed as:

$$P = \sum_{\mathrm{m}=0}^{\infty} P_{\mathrm{m}} = \mathrm{I_0} \sum_{\mathrm{m}=0}^{\infty} V_{\mathrm{m}} = \mathrm{I_0}^2 \sum_{\mathrm{m}=0}^{\infty} Z_{\mathrm{m}}. \tag{3.6}$$

The last two equalities come from assuming that a constant current, $\mathrm{I_0}$, is maintained on the vertical metal strip. Equation (3.6) shows that the impedance harmonic terms, $\mathrm{Z_m}$, add in series. As a result, the driving-point impedance for a device in the grid can be calculated by summing over the impedance terms:

$$Z = \sum_{\mathrm{m}=0}^{\infty} Z_{\mathrm{m}} = \sum_{\mathrm{m}=0}^{\infty} \frac{\mathrm{V_m}^2}{P_{\mathrm{m}}}. \tag{3.7}$$

The power delivered by the grid can also be determined by calculating the total power in the radiated fields. This is done by applying equation (2.39) in the preceding chapter. Evaluating the inner products for the TEM, TM and TE mode expansion coefficients, we find that the total power is given by:

$$P = \frac{\mathrm{V_0^2}}{\mathrm{ab}} \sum_{\mathrm{m}=0}^{\infty} \sum_{n=0}^{\infty} \epsilon_{\mathrm{m0}} \epsilon_{\mathrm{0n}} \, \mathrm{sinc}^2(\frac{\mathrm{n}\pi \mathrm{w}}{\mathrm{b}}) \frac{\{k_y^2 Y_{\mathrm{mn}}^{\mathrm{TM}} + k_x^2 Y_{\mathrm{mn}}^{\mathrm{TE}}\}}{k_c^2} \tag{3.8}$$

$$\times \Big(\int_0^{\mathrm{a}} u(x) \cos(\frac{\mathrm{m}\pi x}{\mathrm{a}}) \, dx \Big)^2.$$

In this expression, the admittances Y_{mn}^{TM} and Y_{mn}^{TE} are assumed to be parallel combinations of the wave admittances looking in the $+z$ and $-z$ directions. Also note that the TEM mode is included with the m = 0, n = 0 term. From equation (3.5) we find V_m which is used with equations (3.7) and (3.8) to find the grid driving-point impedance:

$$Z = \frac{b}{a} \sum_{m=0}^{\infty} \frac{\epsilon_{m0}\ \mathrm{sinc}^2(\frac{m\pi g}{a})}{\sum_{n=0}^{\infty} \frac{\epsilon_{0n}}{k_c^2}\ \mathrm{sinc}^2(\frac{n\pi w}{b})\{k_y^2 Y_{mn}^{TM} + k_x^2 Y_{mn}^{TE}\}}. \tag{3.9}$$

In this expression for the grid embedding impedance, the spatial harmonics associated with the y-direction add in parallel while the harmonics associated with the x-direction add in series. A circuit model representing this embedding impedance is shown in Fig. 3.3. The m = 0 term consists of a parallel combination of TEM and TM modes. Because the TEM modes are propagating waves, they are represented as a resistor. The TM and TE modes are indicated with capac-

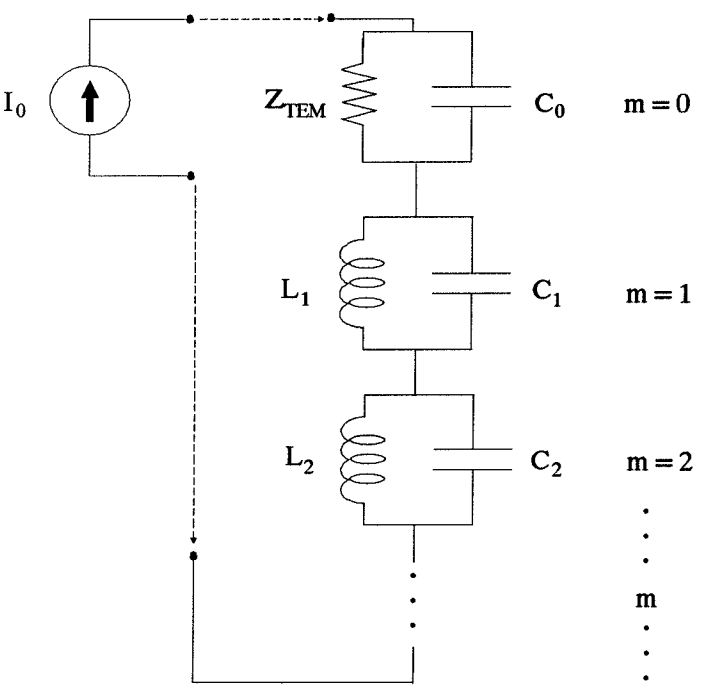

Figure 3.3 Lumped-element circuit model for the slot array embedding impedance. The TEM mode is represented by a lumped resistor. TM and TE modes are shown as capacitors and inductors, respectively.

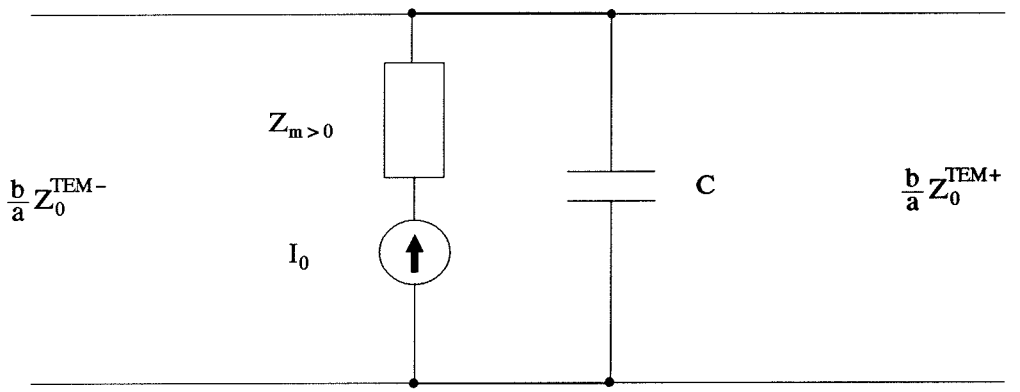

Figure 3.4 Transmission-line model for the rectangular slot array.

itors and inductors, respectively. Fig. 3.3 is a lumped-element representation of the grid as seen by devices embedded in the vertical metal leads. An equivalent transmission-line model for this circuit is shown in Fig. 3.4. The TEM mode is represented with a transmission line. A gap capacitance appears in parallel with the transmission line and is given by :

$$C = \frac{1}{j\omega}\,\frac{2a}{b}\sum_{n=1}^{\infty}\cos^2\left(\frac{n\pi}{2}\right)\operatorname{sinc}^2\left(\frac{n\pi w}{2b}\right)\left(Y_{0n}^{TM+} + Y_{0n}^{TM-}\right) \tag{3.10}$$

which is the same capacitance calculated in equation (2.42). The remaining terms ($m > 0$) consist of both capacitive (TM) and inductive (TE) modes which appear in series with the embedded device. In Fig. 3.4, these terms are represented with a series impedance which is given by:

$$Z_{m>0} = \frac{2b}{a}\sum_{m=1}^{\infty}\frac{\operatorname{sinc}^2\left(\frac{m\pi g}{a}\right)}{\sum_{n=0}^{\infty}\frac{\epsilon_{0n}}{k_c^2}\operatorname{sinc}^2\left(\frac{n\pi w}{b}\right)\left\{k_y^2 Y_{mn}^{TM} + k_x^2 Y_{mn}^{TE}\right\}}. \tag{3.11}$$

At low frequencies, the inductive modes dominate so that $Z_{m>0}$ can be interpreted as the lead inductance of the vertical strip.

3.2 Bow-tie Grids

The bow-tie antenna is a structure which is also attractive for integration with two-terminal devices. One advantage of the bow-tie is that its input impedance is not a strong function of frequency. In fact, the impedance of an infinite bow-tie antenna is independent of frequency. As a result, this structure allows for the possibility of constructing very broadband circuits. The quasi-static impedance, Z_{bt}, for the bow-tie on a semi-infinite dielectric substrate may be determined from transmission-line theory [5,6]. In this analysis, the antenna input impedance is calculated as the characteristic impedance of a radial transmission line and is given by

$$Z_{bt} = \eta_0 \sqrt{\frac{2}{\epsilon_r + 1}} \frac{K(k)}{K'(k)}, \tag{3.12}$$

where $K(k)$ and $K'(k)$ are elliptic integrals, ϵ_r is the substrate dielectric constant, and $k = \tan^2(45° - \theta/4)$, where θ is the bow-tie angle. A rigorous analysis of the bow-tie antenna based on the method of moments was developed by Compton [7] and gave good agreement with measured results.

An array of bow-tie antennas, shown in Fig. 3.5, may be analyzed using the techniques outlined in chapter 2. To find the equivalent circuit for the bow-tie unit cell, we assume an impressed electric current flows on the bow. In addition, an electric field will exist between the bow and the electric wall of the equivalent waveguide. We can account for this by assuming a magnetic current flows in the gap. The charge distribution on the diagonal metal strip representing a bow-tie in the unit cell can be determined by conformal mapping techniques. This charge distribution will have a singularity along the edge of the bow. In the quasi-static approximation, the current density will have the same edge singularity [8] and may be expressed as

$$\mathbf{J}(r, \psi) = \frac{\mathrm{I}_0 / r}{\sqrt{\sin^2\phi - \sin^2\psi}} \hat{r}, \tag{3.13}$$

where ϕ is the angle of the bow and $0 \leq \psi \leq \phi$. This current distribution is used in the EMF analysis of the previous chapter to find an expression for the bow-tie

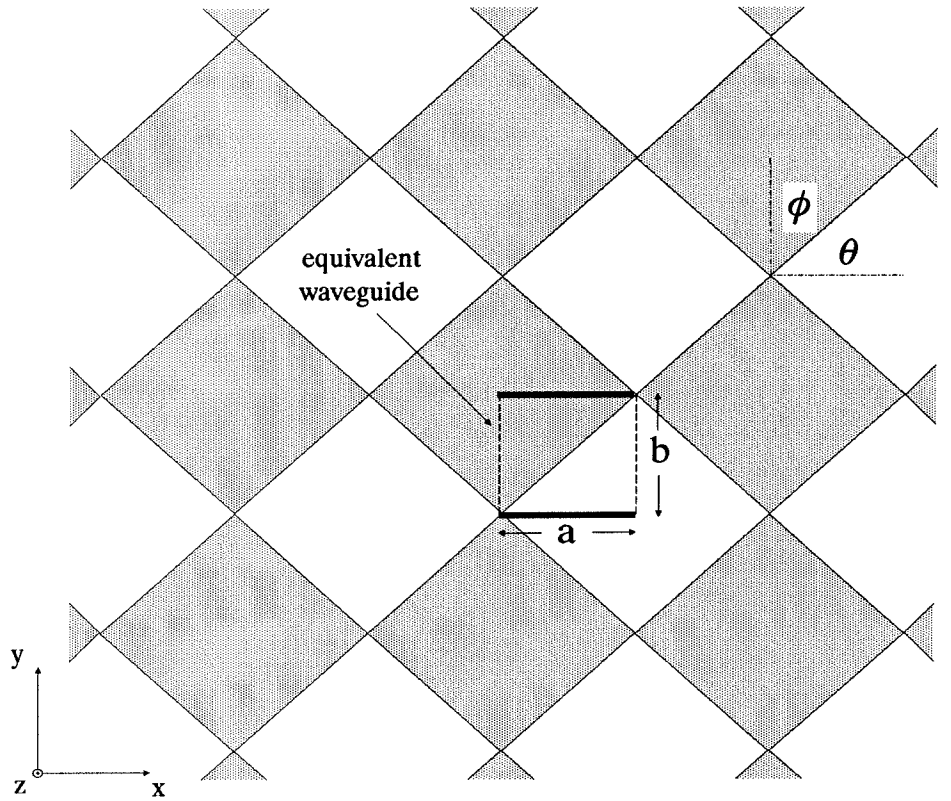

Figure 3.5 Schematic of a bow-tie grid. The equivalent waveguide is shown with solid lines representing electric walls and dashed lines representing magnetic walls.

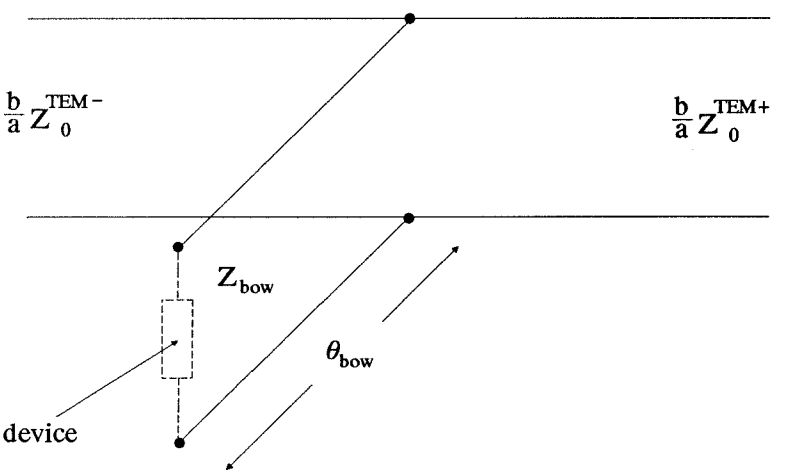

Figure 3.6 Transmission-line model for the bow-tie grid. The bow-tie antennas are represented as a shunt transmission line with characteristic impedance Z_{bow} and electrical length θ_{bow}.

input impedance. Application of equation (2.28) gives us

$$Z = \frac{1}{ab} \sum_{\substack{m=1 \\ n=0}}^{\infty} 2\epsilon_{0n} \frac{k_c^2}{k_x^2} A_{mn}^2 \left(Z_{mn}^{TE+} \parallel Z_{mn}^{TE-}\right), \tag{3.14}$$

where

$$A_{mn} = \frac{\int_0^b \int_0^\phi \frac{\cos(k_x y \tan\psi)}{\sqrt{\sin^2\phi - \sin^2\psi}} \cos k_y y \, d\psi dy}{\int_0^\phi \frac{d\psi}{\sqrt{\sin^2\phi - \sin^2\psi}}}. \tag{3.15}$$

In equation (3.14), the TEM mode is included when m = 0, n = 0. The electric current couples to TE modes which gives rise to an inductance for the bow-tie grid. This expression gives only part of the impedance because power stored in the electric fields between the bow-ties has been neglected. We include this contribution by assuming a magnetic current flows between the bow-tie antennas. The magnetic current is assumed to have the same form as the electric current in equation (3.13) and is given by

$$M(r, \xi) = \frac{M_0/r}{\sqrt{\sin^2\theta - \sin^2\xi}} \hat{r}, \tag{3.16}$$

where $\theta = 90° - \phi$ and $0 \leq \xi \leq \theta$. Application of equation (2.39) gives us

$$Y = \frac{1}{ab} \sum_{\substack{m=0 \\ n=1}}^{\infty} 2\epsilon_{m0} \frac{k_c^2}{k_y^2} B_{mn}^2 \left(Y_{mn}^{TM+} + Y_{mn}^{TM-}\right), \tag{3.17}$$

where

$$B_{mn} = \frac{\int_0^a \int_0^\theta \frac{\cos(k_y x \tan\xi)}{\sqrt{\sin^2\theta - \sin^2\xi}} \cos k_x x \, d\xi dx}{\int_0^\theta \frac{d\xi}{\sqrt{\sin^2\theta - \sin^2\xi}}}. \tag{3.18}$$

The magnetic current couples only to the TM modes and leads to a bow-tie capacitance. This capacitance may be considered as distributed along the length of the bow-tie. Equation (3.17) gives an expression for the total capacitance of a bow in the unit cell. Similarly, the inductance calculated in equation (3.14)

is also distributed along the length of the bow. As a result, the bow-tie array can be modeled as a section of transmission line with net inductance given by equation (3.14) and net capacitance given in (3.17). It is straightforward to show that these equations satisfy Babinet's principle for a bow-tie flair angle of 45°. The characteristic impedance, Z_{bow}, and electrical length, θ_{bow}, of the bow-tie transmission line are given by

$$Z_{bow} = \sqrt{\frac{\mathrm{Z}}{\mathrm{Y}}} \tag{3.19}$$

and

$$\theta_{bow} = \sqrt{\mathrm{ZY}}. \tag{3.20}$$

The bow-tie grid model is shown in Fig. 3.6. The transmission line representing the bow-tie grid appears in shunt across a second transmission line which models propagating TEM waves.

A device embedded in a bow-tie grid couples to an incident TEM wave through a short section of transmission line. The characteristic impedance for a 45° bow-tie grid on a substrate of $\epsilon_r = 10$ is about 78 Ω. This value can be made larger or smaller by adjusting the aspect ratio of the unit cell. The electrical length of the bow-tie is typically only a small fraction of a free-space wavelength. With a backshort used for reactive tuning, the bow-tie structure can offer an excellent means of matching solid-state devices to incident electromagnetic radiation [9].

3.3 Planar Transistor Grids

The grid configurations discussed so far have been well-suited for integration with two-terminal solid-state devices. However, it is also possible to embed three-terminal devices such as transistors and contiguous domain oscillators (CDO's) [10] into a periodic array. Transistors, for a variety of reasons, are attractive devices for use in a quasi-optical grid. Two of the device terminals can

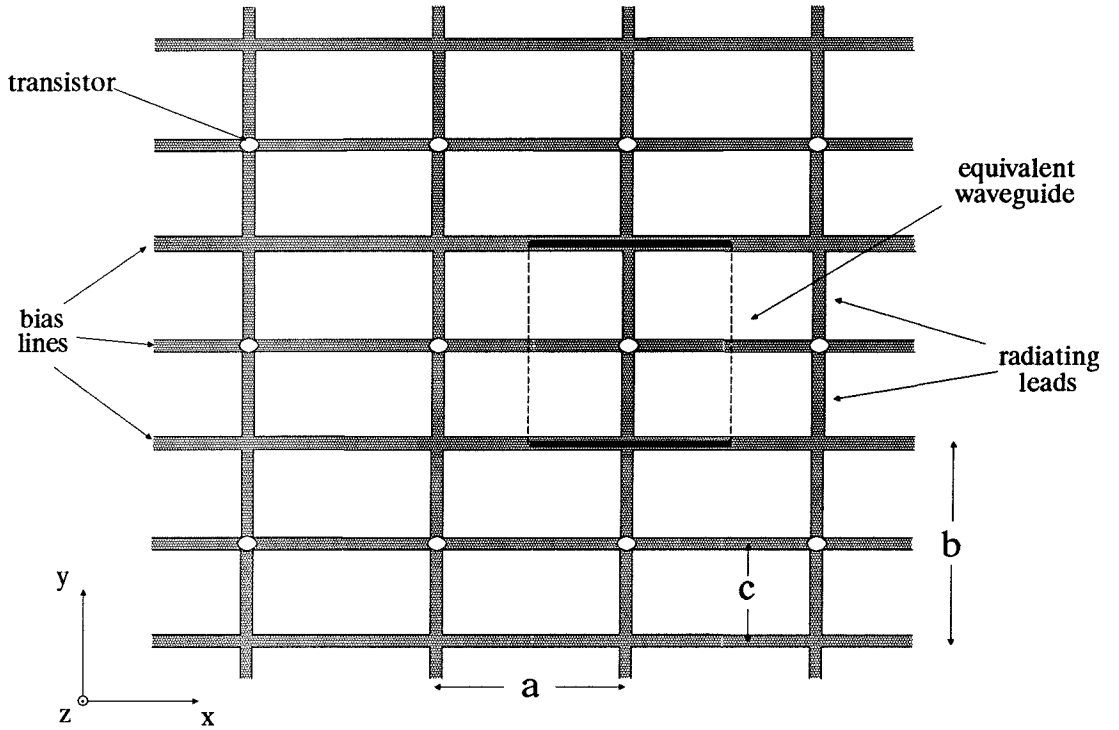

Figure 3.7 Configuration of a planar transistor grid. Bias lines run horizontally across the grid while the radiating leads run vertically as shown. Adjacent rows of devices share bias lines. The equivalent waveguide is shown with solid lines for electric walls and dashed lines for magnetic walls.

couple to an output wave leaving the third as a separate input terminal. By attaching the terminals to antennas designed to receive and transmit orthogonally polarized waves, it is possible to build a plane-wave amplifier [11]. The grid embedding circuit can also be used to provide feedback between the device input and output to create an oscillator [12]. Other applications have included using the transistor as a tuning element to electronically vary the resonant length of slot antennas [13]. One question that arises when using transistors as the active element in a quasi-optical array involves how to accommodate the third device terminal. The design must provide DC bias to the transistors as well as allow a means of coupling the devices to free-space radiation. In addition, a grid configuration which is completely planar has certain advantages with respect to monolithic integration. For the two-terminal device grids, DC bias is fed from the sides of the grid on horizontal metal lines. These bias lines are perpendicular

to the polarization of the incident and radiated electric fields. This suggests the planar configuration of Fig. 3.7 is a suitable design for a quasi-optical transistor grid. In this design, adjacent rows of transistors are oriented so they can share bias lines. The devices themselves are placed on (or embedded into) a central bias line which runs through the center of the unit cell. By orienting the devices in this way, the mirror symmetry of the array is preserved and this allows a unit cell equivalent waveguide to be defined. Currents on the vertical leads couple directly to radiation polarized along the y-direction. However, from the grid symmetry, currents on the bias lines cancel at the sides of the unit cell.

To apply the EMF method of the preceding chapter, we need to assume a current distribution on the transistor leads. A schematic of the grid equivalent waveguide is shown in Fig. 3.8(a). Two of the transistor terminals are connected to the vertical leads. We designate the currents on these leads as I_1 and I_2. The third device lead is connected on both sides to a horizontal bias line and carries a total current of I_3. By symmetry, half of I_3 will flow to the left of the device and half to the right. In addition, these horizontal currents must vanish at the sides of the unit cell where there is a magnetic wall. This leads us to the distribution shown in Fig. 3.8(b) for the current on the horizontal lead. The current is assumed to be piecewise continuous and varies linearly with distance. We also assume that the current density is uniform across the lead. Thus we write the horizontal current as :

$$J_h(x,y,z) = \frac{I_3}{2\mathrm{w_s}}\, h(x)h(y)\delta(z)\ \hat{x} \tag{3.21}$$

where

$$h(x) = \begin{cases} -2x/(\mathrm{a}-\mathrm{w}), & \text{for } 0 \le x \le \frac{\mathrm{a}-\mathrm{w}}{2}; \\ (2x-\mathrm{a})/\mathrm{w}, & \text{for } \frac{\mathrm{a}-\mathrm{w}}{2} \le x \le \frac{\mathrm{a}+\mathrm{w}}{2}; \\ -2(x-\mathrm{a})/(\mathrm{a}-\mathrm{w}), & \text{for } \frac{\mathrm{a}+\mathrm{w}}{2} \le x \le \mathrm{a} \end{cases} \tag{3.22}$$

and

$$h(y) = \begin{cases} 1, & \text{for } \mathrm{c} - \frac{\mathrm{w_s}}{2} \le y \le \mathrm{c} + \frac{\mathrm{w_s}}{2}; \\ 0, & \text{otherwise.} \end{cases} \tag{3.23}$$

Currents flowing in the vertical direction are also assumed to be uniform across the leads. Furthermore, because they flow into and out of electric walls, we can assume these currents are uniform along the leads. However, I_1 and I_2 may differ in magnitude and phase because they connect to different leads of the transistor. As a result, we assume the vertical currents can be written as :

$$J_v(x,y,z) = v(x)v(y)\delta(z)\ \hat{y}, \tag{3.24}$$

where

$$v(y) = \begin{cases} -I_2/\mathrm{w}, & \text{for } 0 \le y \le \mathrm{c} - \frac{\mathrm{w_s}}{2}; \\ \frac{I_1}{\mathrm{ww_s}}\ (y - \mathrm{c} + \mathrm{w_s}/2) + & \\ \quad \frac{I_2}{\mathrm{ww_s}}\ (y - \mathrm{c} - \mathrm{w_s}/2), & \text{for } \mathrm{c} - \frac{\mathrm{w_s}}{2} \le y \le \mathrm{c} + \frac{\mathrm{w_s}}{2}; \\ I_1/\mathrm{w}, & \text{for } \mathrm{c} + \frac{\mathrm{w_s}}{2} \le y \le \mathrm{b}; \end{cases} \tag{3.25}$$

and

$$v(x) = \begin{cases} 1, & \text{for } \frac{\mathrm{a-w}}{2} \le x \le \frac{\mathrm{a+w}}{2}; \\ 0, & \text{otherwise.} \end{cases} \tag{3.26}$$

The vertical current distribution as a function of y is shown in Fig. 3.8(c). In these formulas, I_1, I_2, and I_3 are assumed to be phasor amplitudes which may have different magnitudes and phases. The only assumptions made about the currents concern their spatial distribution along and across the leads. Using these current distributions and evaluating the inner products, $\langle \mathbf{J}_{\mathrm{xy}} | \hat{u}^l_{\mathrm{mn}} \rangle$, we find:

$$j_0 = \frac{1}{\sqrt{\mathrm{ab}}}\ (I_1(\mathrm{b} - \mathrm{c})\ -\ \mathrm{c}I_2)$$

$$j^{\mathrm{TM}}_{\mathrm{mn}} = \sqrt{\frac{2\epsilon_{\mathrm{m0}}}{\mathrm{ab}k_c^2}}\ \cos(\frac{\mathrm{m}\pi}{2})\ \sin(\frac{\mathrm{n}\pi\mathrm{c}}{\mathrm{b}})\ \mathrm{sinc}(\frac{\mathrm{m}\pi\mathrm{w}}{2\mathrm{a}})\ \mathrm{sinc}(\frac{\mathrm{n}\pi\mathrm{w_s}}{2\mathrm{b}}) \times$$
$$\{(\frac{\mathrm{a}}{\mathrm{a-w}})\ I_3 + I_1 + I_2\} \tag{3.27}$$

$$j^{\mathrm{TE}}_{\mathrm{mn}} = \sqrt{\frac{2\epsilon_{\mathrm{0n}}}{\mathrm{ab}k_c^2}}\ \cos(\frac{\mathrm{m}\pi}{2})\ \sin(\frac{\mathrm{n}\pi\mathrm{c}}{\mathrm{b}})\ \mathrm{sinc}(\frac{\mathrm{m}\pi\mathrm{w}}{2\mathrm{a}})\ \mathrm{sinc}(\frac{\mathrm{n}\pi\mathrm{w_s}}{2\mathrm{b}}) \times$$
$$\{\frac{k_y}{k_x}\ (\frac{\mathrm{a}}{\mathrm{a-w}})\ I_3 - \frac{k_x}{k_y}\ (I_1 + I_2)\}.$$

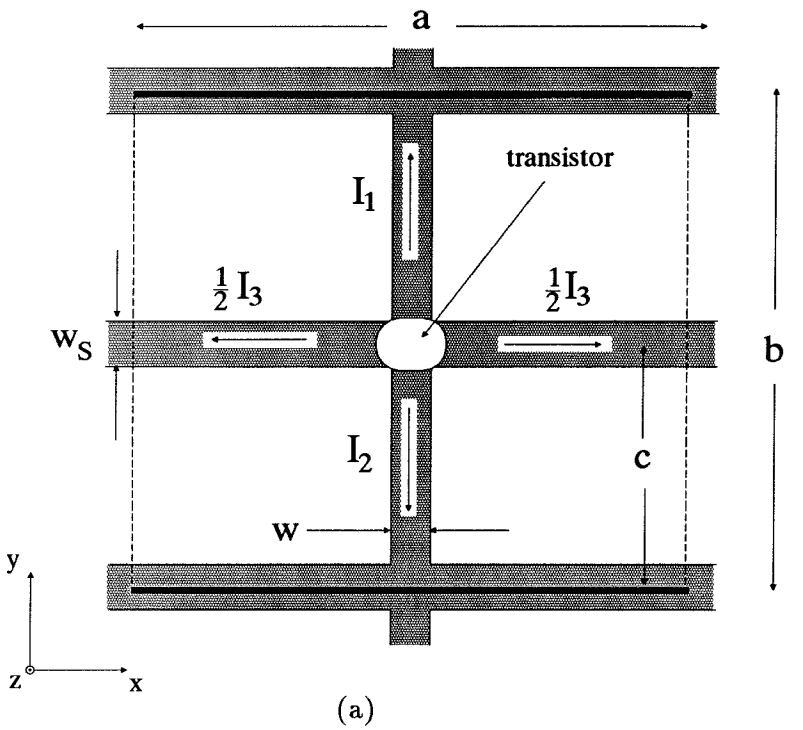

(a)

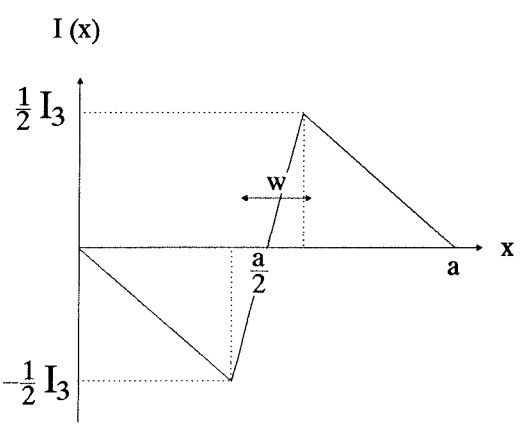

(b)

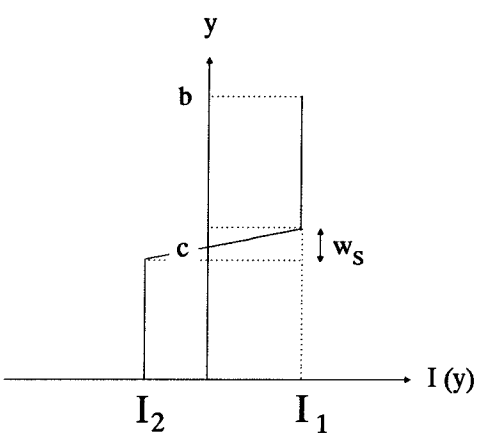

(c)

Figure 3.8 (a) Schematic of an equivalent waveguide for the planar transistor grid. The radiated field is assumed polarized in the y-direction. (b) Current distribution along the horizontal lead and (c) vertical lead.

In addition, the currents flowing into and out of the transistor must satisfy Kirchoff's Law

$$I_1 + I_2 + I_3 = 0. \tag{3.28}$$

Applying Kirchoff's Law to the current expansion coefficients given in equation (3.27) and using the complex power expansion of equation (2.24), we obtain the following expression:

$$P = \{(1-r)^2\ (Z_0 + Z_L) + Z_C + Z\ \}\ I_1 I_1^* + \tag{3.29}$$

$$\{r^2\ (Z_0 + Z_L) + Z_C + Z\ \} I_2 I_2^* - \{r(1-r)\ (Z_0 + Z_L) - Z_C - Z\ \} I_1^* I_2$$

$$-\{r(1-r)\ (Z_0 + Z_L) - Z_C - Z\} I_1 I_2^*,$$

where the $r = \mathrm{c/b}$ and impedance terms are defined as:

$$Z_0 = \frac{\mathrm{b}}{\mathrm{a}}\ (Z_0^{\mathrm{TEM}+} \parallel Z_0^{\mathrm{TEM}-}) \tag{3.30}$$

$$Z_L = \frac{2\mathrm{b}}{\mathrm{a}} \sum_{\mathrm{m}=1}^{\infty} \cos^2\left(\frac{\mathrm{m}\pi}{2}\right) \mathrm{sinc}^2\left(\frac{\mathrm{m}\pi\mathrm{w}}{2\mathrm{a}}\right)\ (Z_{\mathrm{m0}}^{\mathrm{TE}+} \parallel Z_{\mathrm{m0}}^{\mathrm{TE}-}) \tag{3.31}$$

$$Z_C = \frac{2}{\mathrm{ab}} \sum_{\mathrm{n}=1}^{\infty} \frac{1}{k_y^2} \sin^2\left(\frac{\mathrm{n}\pi\mathrm{c}}{\mathrm{b}}\right) \mathrm{sinc}^2\left(\frac{\mathrm{n}\pi\mathrm{w_s}}{2\mathrm{b}}\right)\ (Z_{\mathrm{0n}}^{\mathrm{TM}+} \parallel Z_{\mathrm{0n}}^{\mathrm{TM}-}) \tag{3.32}$$

$$Z = \frac{4}{\mathrm{ab}} \sum_{\substack{\mathrm{m}>0 \\ \mathrm{n}>0}}^{\infty} \frac{1}{k_c^2} \cos^2\left(\frac{\mathrm{m}\pi}{2}\right) \sin^2\left(\frac{\mathrm{n}\pi\mathrm{c}}{\mathrm{b}}\right) \mathrm{sinc}^2\left(\frac{\mathrm{m}\pi\mathrm{w}}{2\mathrm{a}}\right) \mathrm{sinc}^2\left(\frac{\mathrm{n}\pi\mathrm{w_s}}{2\mathrm{b}}\right) \times \tag{3.33}$$

$$\left\{\left(1 - \frac{\mathrm{a}}{\mathrm{a}-\mathrm{w}}\right)^2 Z_{\mathrm{mn}}^{\mathrm{TM}+} \parallel Z_{\mathrm{mn}}^{\mathrm{TM}-} + \left(\frac{k_x}{k_y} + \frac{k_y \mathrm{a}}{k_x(\mathrm{a}-\mathrm{w})}\right)^2 Z_{\mathrm{mn}}^{\mathrm{TE}+} \parallel Z_{\mathrm{mn}}^{\mathrm{TE}-}\right\}.$$

There are four distinct impedance terms in equation (3.29). Z_0 is simply the parallel combination of the TEM impedances looking in the $+z$ and $-z$ directions. Z_L is a sum over TE mode impedances and appears in series with Z_0. It represents the inductance associated with the vertical leads. Similarly, Z_C is a combination of TM mode impedances and gives rise to a capacitive term in

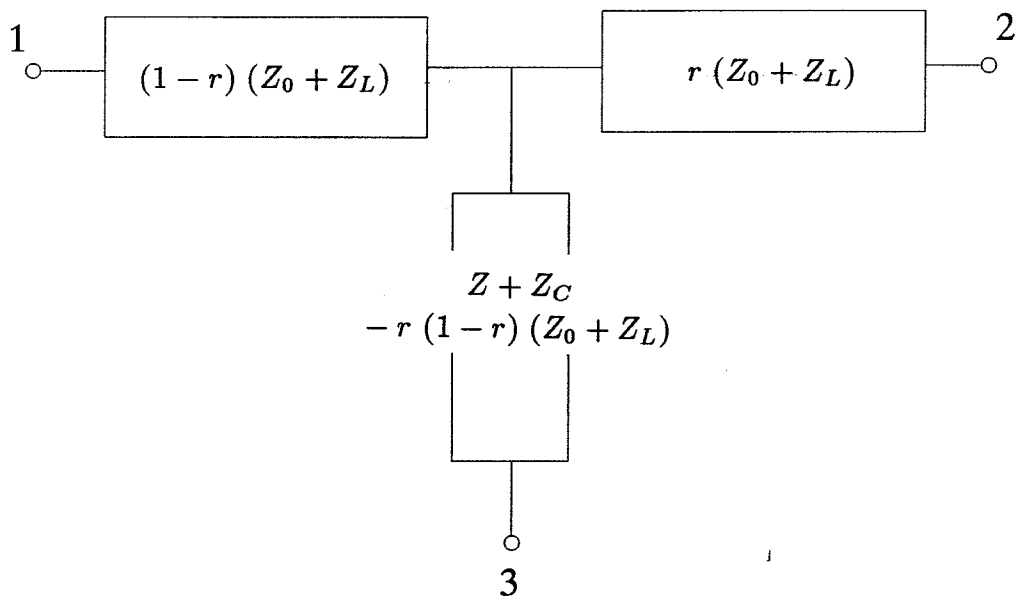

(a)

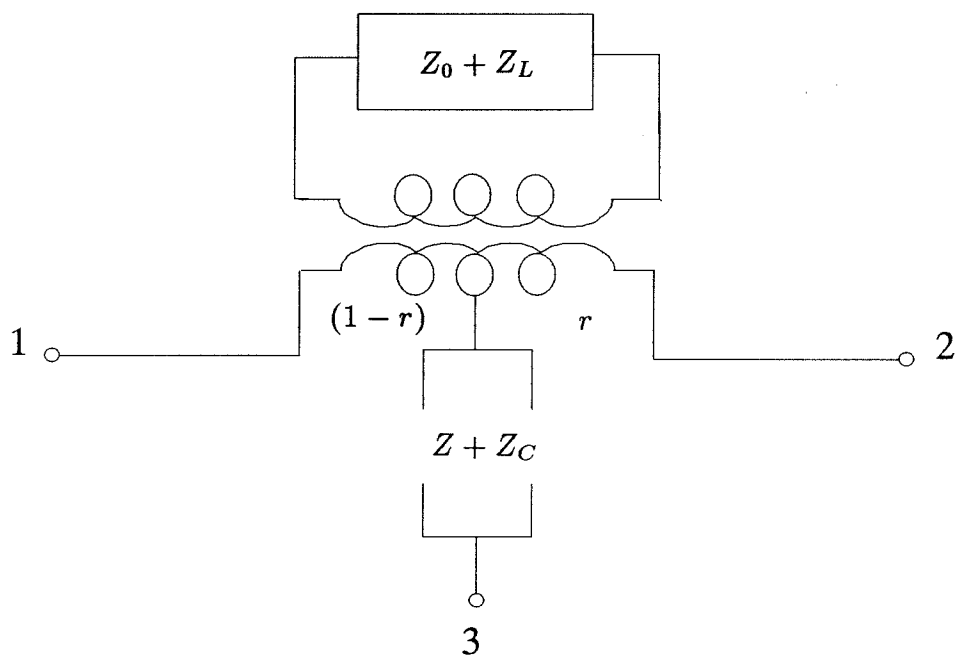

(b)

Figure 3.9 (a) Two-port equivalent network for the planar transistor grid. (b) Transistor grid network model with the center-tapped transformer.

the impedance expression. Finally, there is a term denoted as Z which is a series combination of TM and TE modes. This represents capacitive and inductive impedances connected in series. Equation (3.29) is somewhat different than the previous formulas for the grid driving-point impedance because it involves two current excitations, I_1 and I_2. The form of equation (3.29) is reminiscent of the expression for the complex power delivered to a two-port linear network. Two-port linear networks are characterized by an impedance matrix relating the voltages and currents at the network terminals. By inspection, we can write the impedance matrix of the transistor grid directly from equation (3.29). This two-port network is shown in Fig. 3.9 connected as a "T" equivalent model. The terminal labels (1,2,3) correspond to the transistor currents (I_1, I_2, I_3).

In the "T" model for the grid, a common impedance term, $Z_0 + Z_L$, appears in all three branches. The arrangement of the impedances in this network can be represented with a circuit containing a center-tapped transformer as shown in Fig. 3.9(b). The impedance term, $Z_0 + Z_L$, appears on one side of the trans-

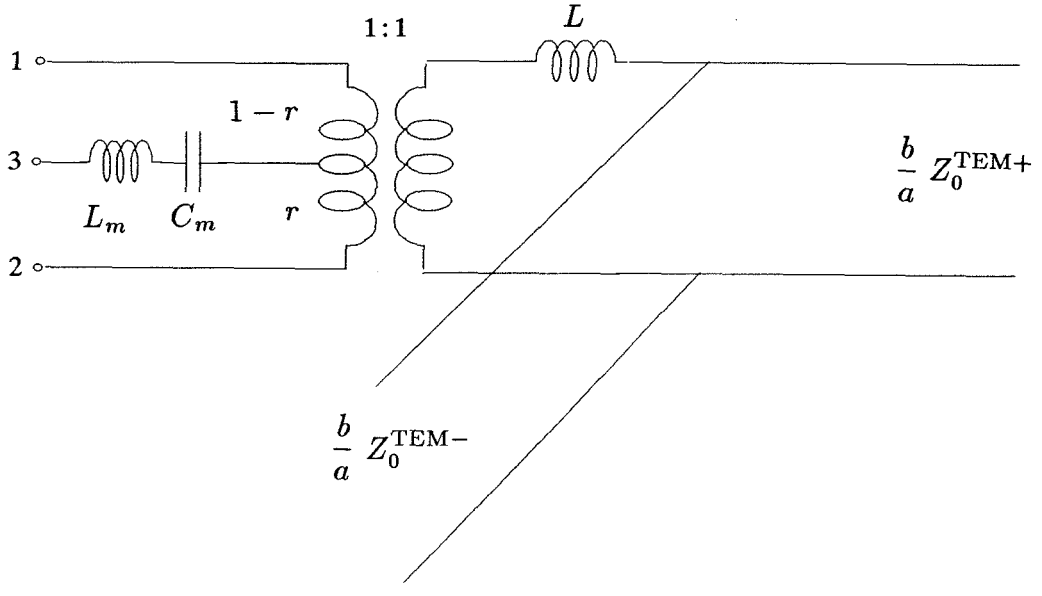

Figure 3.10 Equivalent transmission-line model for the planar transistor grid. Propagating TEM modes are represented with transmission lines and evanescent modes with reactive lumped elements. The transformer turns ratio is given by $r = c/b$.

former, which has a total turns ratio of 1 : 1. On the side with the center tap, the turns ratios are r and $1 - r$, respectively with the impedance, $Z_C + Z$, appearing in the center lead. The two networks shown in Fig. 3.9 are equivalent. However, the circuit of Fig. 3.9(b) is more useful with regard to finding the embedding impedance a transistor sees when placed in the grid. The grid equivalent transmission-line model is shown in Fig. 3.10. In this model, the TM and TE mode impedances are represented explicitly using capacitors and inductors. Terminals 1 and 2 of the circuit represent connections to the vertical leads of the grid. Currents in these leads couple to the radiated field through the transformer. TEM waves propagating to and from the grid are represented with transmission lines. In addition, there is a lead inductance, L, associated with TE modes excited by currents flowing in the y-direction. The third terminal of the transistor is connected to the horizontal lead running through the center of the unit cell. Currents on this lead are perpendicular to the radiated field and thus produce evanescent TE and TM modes which are modeled with reactive lumped elements. It should be noted that the model neglects the capacitance between the grid bias lines. This is justified if the bias lines are sufficiently thin and far apart.

The planar grid transmission-line model shown in Fig. 3.10 is general in that it makes no assumption as to how the transistor is connected to the grid. Two transistor leads will radiate and the third will couple to this radiation through the center lead reactive elements. In effect, the center lead is a path that provides feedback at a frequency determined by the resonance of these reactive elements. In choosing the dimensions for the unit cell, the reactance in the feedback path can be adjusted to produce instability at a particular frequency. In this way, a planar grid oscillator can be realized [12,14].

References

[1] D.B. Rutledge, S.E. Schwarz, "Planar Multimode Detector Arrays for Infrared and Millimeter-Wave Applications," *IEEE J. Quantum Electronics*, QE-17, pp. 407–414, March 1981.

[2] W.W. Lam, C.F. Jou, H.Z. Chen, K.S. Stolt, N.C. Luhmann, Jr., D.B. Rutledge, "Millimeter-Wave Diode-Grid Phase Shifters," *IEEE Trans. Microwave Theory Tech.*, MTT-36, pp. 902–907, May 1988.

[3] C.F. Jou, W.W. Lam, H.Z. Chen, K.S. Stolt, N.C. Luhmann, Jr., D.B. Rutledge, "Millimeter-Wave Diode-Grid Frequency Doubler," *IEEE Trans. Microwave Theory Tech.*, MTT-36, pp. 1507–1514, November 1988.

[4] R.L. Eisenhart, P.J. Khan, "Theoretical and Experimental Analysis of a Waveguide Mounting Structure," *IEEE Trans. Microwave Theory Tech.*, MTT-19, pp. 706–719, August 1971.

[5] D.B. Rutledge, M.S. Muha, "Imaging Antenna Arrays," *IEEE Trans. Antennas and Propagat.*, AP-30, pp. 535–540, July 1982.

[6] D.B. Rutledge, D.P. Neikirk, D.P. Kasilingam, "Integrated Circuit Antennas," *Infrared and Millimeter Waves,* vol. 10, K.J. Button ed., Academic Press, New York, 1983, pp. 1–90.

[7] R.C. Compton, *Analysis of Millimeter and Microwave Integrated Circuits,* Ph.D. Thesis, California Institute of Technology, Pasadena, CA, Chapter 2, 1987.

[8] R.C. Compton, R.C. McPhedran, Z. Popović, G.M. Rebeiz, P.P Tong, D.B. Rutledge, "Bow-tie Antennas on a Dielectric Half-Space: Theory and Experiment," *IEEE Trans. Antennas and Propagat.,* AP-35, pp. 622–631, June 1987.

[9] J.B. Hacker, R.M. Weikle, II, M. Kim, M.P. De Lisio, D.B. Rutledge, "A 100-Element Planar Schottky Diode Grid Mixer," *submitted to the IEEE Trans. Microwave Theory Tech.*, July 1991.

[10] J.A. Cooper, K.K. Thornber, "Screened-Space-Charge Transferred-Electron Oscillators," *IEEE Electron Device Letters,* EDL-6, pp. 50–53, January 1985.

[11] M. Kim, J.J. Rosenberg, R.P. Smith, R.M. Weikle, II, J.B. Hacker, M.P. De Lisio, D.B. Rutledge, "A Grid Amplifier," *IEEE Microwave and Guided Waves Lett.,* no. 1, vol. 11, pp. 322-324, November 1991.

[12] Z.B. Popović, R.M. Weikle, II, M. Kim, D.B. Rutledge, "A 100-MESFET Planar Grid Oscillator, " *IEEE Trans. Microwave Theory Tech.*, MTT-39, pp. 193–200, February 1991.

[13] S. Kawasaki, T. Itoh, "A Slot Antenna with Electronically Tunable Length," *IEEE AP-S International Symposium Digest,* vol. 1, pp. 130–133, London, Ontario, June 1991.

[14] R.M. Weikle, II, M. Kim, J.B. Hacker, M.P. De Lisio, D.B. Rutledge, "Planar MESFET Grid Oscillators using Gate Feedback," *submitted to the IEEE Trans. Microwave Theory Tech.,* August 1991.

Chapter 4

Quasi-Optical Reflectometer Measurements

In the previous chapters, we used the induced EMF method to derive transmission line models for several different planar grids. These models are based on the assumption that the grid is infinite in extent and the devices in the grid are identical. Furthermore, in applying the EMF method we assumed the current distribution on the grid was either uniform or could be represented with simple piecewise linear functions. Transmission-line models are only approximate representations for planar grids because they neglect edge effects and diffraction. In addition, the embedding impedance calculated from the EMF method can be inaccurate if the assumed current distribution is significantly different from the true distribution. For these reasons, it is desirable to verify the grid transmission-line models by measuring the driving-point impedance the grid presents to an embedded device.

A transmission-line model for a grid of two-terminal devices is shown in Fig. 4.1. A device placed in the grid sees an impedance Z_{in} and a plane wave incident on the grid sees a reflection coefficient Γ. Ideally, we would like to measure the input impedance Z_{in}. For a finite grid, this involves placing devices (or equivalent loads) in each unit cell and measuring the impedance at one pair of input terminals. A difficulty with this method is that an impedance probe must be placed at the unit cell terminals without disturbing the fields around the grid. Also, during the measurement, all the devices in the grid must be locked in phase as they are when the grid is operating normally. As a result,

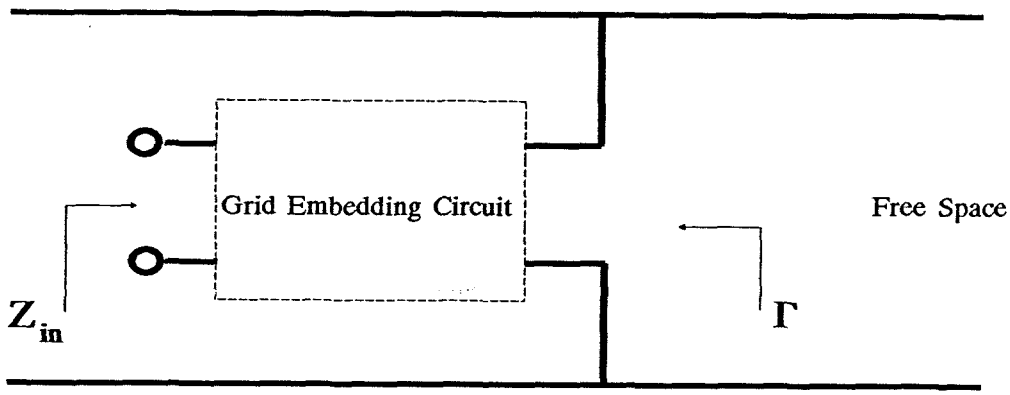

Figure 4.1 A grid transmission-line model. The grid embedding circuit can be determined by measuring the driving-point impedance Z_{in} or the reflection coefficient presented to an incident plane wave Γ.

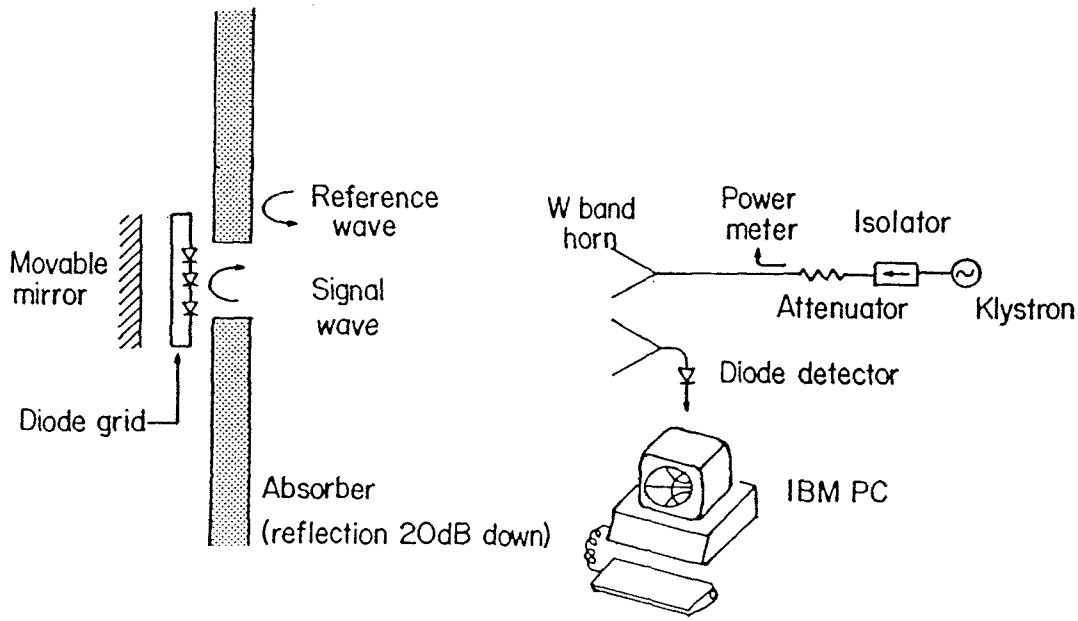

Figure 4.2 Schematic of the small aperture reflectometer used by Lam [6].

many researchers have developed more practical techniques based on waveguide simulators and quasi-optical reflectometers.

4.1 Grid Measurement Techniques

One method for measuring the driving-point impedance Z_{in} is to simulate the grid in waveguide. This approach allows the entire grid to be represented with only a few elements or a single unit cell. Hannan and Balfour developed a technique for determining the impedance of phased-array antennas using a variety of apertures placed in metal waveguides [1]. In their experiment, radiation of different polarizations and incident from various directions is simulated by exciting different metal waveguide modes. The impedance of elements in the array is determined by measuring the reflection coefficient with a slotted line. More recently, Pance and Wengler modeled two-dimensional grids using a parallel-plate waveguide and a rectangular dielectric rod [2]. Metal plates replace the electric walls of the unit cell equivalent waveguide and the dielectric rod simulates the grid substrate. A small hole in the metal plates allows access to the waveguide feed input terminals. The grid driving-point impedance is then measured with a microwave network analyzer.

Modeling of grid arrays in waveguide is convenient because the number of grid elements needed is greatly reduced. There are, however, several drawbacks to the method. Precision machining is required to reproduce the details of the grid unit cell. Furthermore, there is no easy way to duplicate the magnetic walls on the sides of the grid equivalent waveguide. Finally, array simulation using waveguides becomes difficult at high frequencies thus making scaled models necessary. For these reasons, measurement methods based on quasi-optical techniques are attractive, particularly at millimeter-wave frequencies.

If a known load is placed across the input terminals of Fig. 4.1, then the grid embedding impedance can be deduced from the reflection coefficient Γ. Several different quasi-optical systems have been developed to measure the reflection

coefficients of planar structures. Many of these systems use beam splitters and power sensors to sample the field intensity at various measurement planes and are thus equivalent to the six-port reflectometer [3]. Using horn antennas and dielectric lenses, the reflection coefficient of dielectrics can be measured with great precision. Stumper used a four-port quasi-optical reflectometer to measure the complex dielectric constant of fused silica at 390 GHz with an uncertainty of 0.02 in magnitude and 2° in phase [4]. An alternative method is based on measuring the interference of the reflected wave with a reference signal. With this scheme, it is only necessary to use one power detector if the phase relationship between the reflected and reference signals is variable and reproducible [5]. This approach was used by Lam to measure the reflection coefficient of a monolithic Schottky diode-grid phase shifter at 93 GHz [6]. A schematic of the reflectometer is shown in Fig. 4.2. A horn antenna illuminates the grid which is surrounded by microwave absorber. Reflection of the wave off the absorber provides a reference signal which interferes with the wave reflected from the grid. By sampling the intensity of the interfering waves at 90° intervals, the complex reflection coefficient of the grid can be determined. These 90° phase shifts are introduced by translating the grid relative to the absorber at intervals of one-eighth of a wavelength. Roberts and Compton extended Lam's method to obtain measurements over a continuum of frequencies [7]. Their technique used a magic tee to split the signal from a synthesized sweeper. Part of this signal was sent to a diode detector as the reference and the remainder fed a horn antenna which illuminated the grid. The advantage of this method is the reference and reflected waves are combined in waveguide and thus only one horn antenna is needed for the measurement.

4.2 Reflectometer Model

For reflectometer measurements up to 40 GHz, it is convenient to use a microwave network analyzer. Computer controlled network analyzers have a variety of features such as automatic error correction and the ability to store,

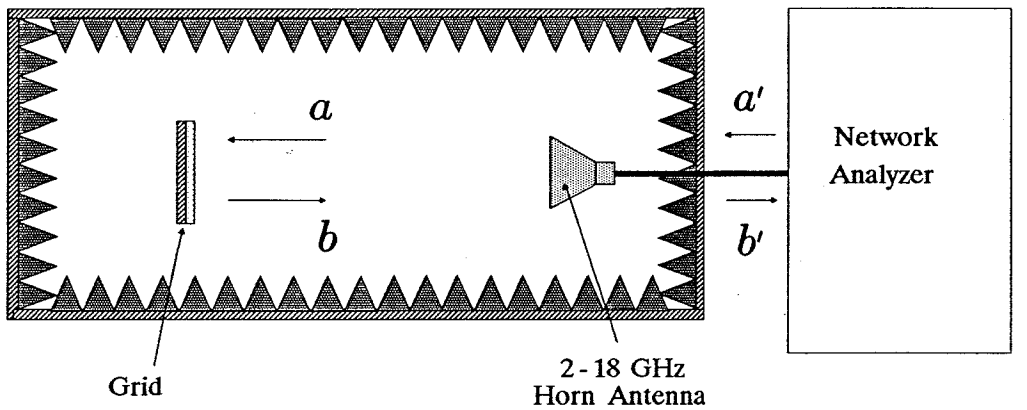

(a)

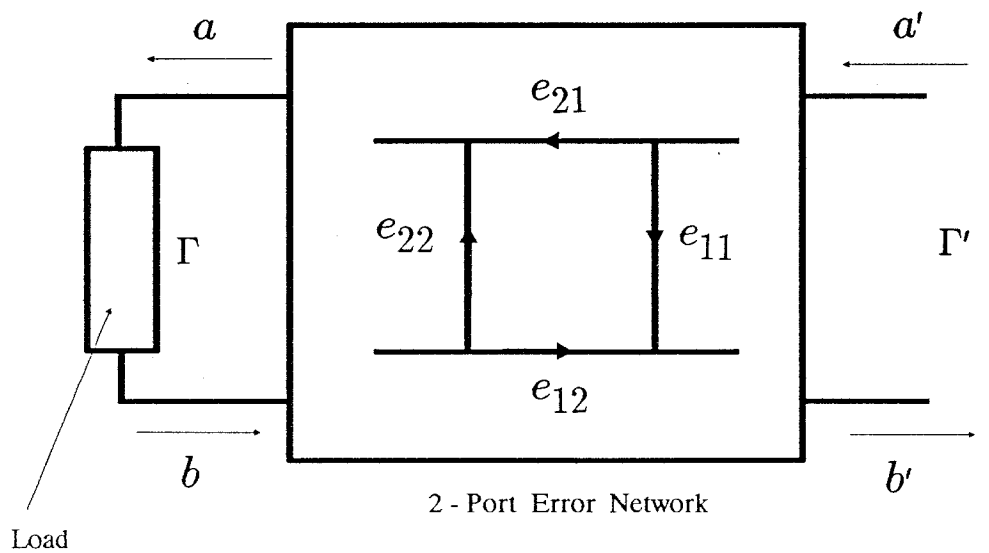

(b)

Figure 4.3 (a) Schematic of a quasi-optical reflectometer using a network analyzer. (b) Network representing the reflectometer. Systematic errors are modeled with a two-port error network.

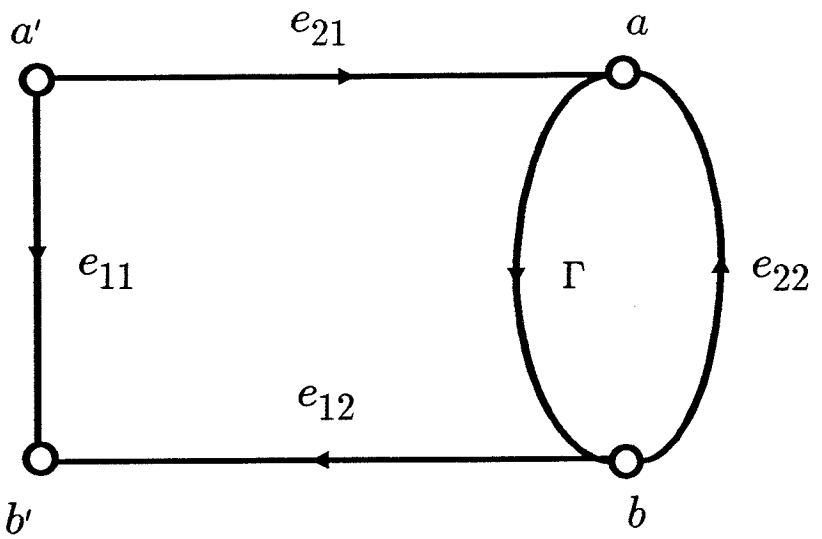

Figure 4.4 Signal flow graph for the reflectometer.

transform, and summarize measured data that facilitate s-parameter measurement. Fig. 4.3(a) shows a schematic of a quasi-optical reflectometer that uses a microwave network analyzer. This experimental setup was used to measure the reflection coefficients of the grids discussed in chapters 2 and 3. A standard gain horn antenna with a bandwidth of 2 to 18 GHz is connected to one port of an HP 8510 network analyzer. The horn is placed at one end of an anechoic chamber and the grid is placed at the other end, 50 cm away. The grid is attached to an optical stage which is mounted on a micrometer. This allows the distance between the horn and grid to be varied with precision. A model of the reflectometer is shown in Fig. 4.3(b). Systematic errors that result from imperfections in the network analyzer as well as reflections from the horn antenna and propagation loss through the chamber are modeled with a two-port error network. A signal flow graph representing this network is shown in Fig. 4.4. Using Mason's Rule [8], we find the reflection coefficient of the grid, Γ, is related to the measured

reflection coefficient, Γ', by :

$$\Gamma' = e_{11} + \frac{e_{21}e_{12}\Gamma}{1 - e_{22}\Gamma} \tag{4.1}$$

To find the reflection coefficient of the grid, the error network must be characterized by calibrating the reflectometer. Hence, it is necessary to find quasi-optical calibration standards.

4.3 System Calibration

Equation (4.1), which relates the measured reflection coefficient to the actual reflection coefficient of the load, contains four unknown parameters. To determine these unknowns, we need to measure the reflection coefficient of known loads or "calibration standards." Because the forward and reverse transmission parameters, e_{21} and e_{12}, appear as a product, only three standards are required to characterize the error network. In principle, we can choose any well-known load as a calibration standard. However, if the reflection coefficients of the standards are close enough that any two overlap due to measurement error, then equation (4.1) will have no solution. Therefore it is desirable to choose standards with well separated reflection coefficients.

Standard network analyzer calibration kits usually include a short, open, and $50\,\Omega$ load. These standards are well separated on the Smith Chart and are suitable for coaxial media. For quasi-optical systems, we can use a planar metal sheet to serve as a short and highly absorbing material for a matched load. Because quasi-optical open circuits do not exist, we choose a delayed short as the third calibration standard. The short defines the reference plane where the measurements are taken. Due to the frequency dependence of the delayed short's reflection coefficient, care must be taken to ensure the calibration standards do not overlap at any of the measurement frequencies. The reflectometer of Fig. 4.3 makes measurements between 2 and 18 GHz. A 7.5 mm delayed short presents a normalized impedance that varies from $+j0.33$ to $-j0.33$ over this frequency

range and, as a result, can be used as a calibration standard throughout the entire band. For measurements over a broad range of frequencies, several delayed shorts can be used for different frequency bands. In fact, by using a series of delayed shorts for calibration standards, it is possible to avoid using a matched load altogether. This technique is described in detail by Engen [9].

The quasi-optical reflectometer of Fig. 4.3, was calibrated using a short, matched load, and two delayed shorts. A square copper sheet 10 cm on a side was used as the short and a 25 cm × 25 cm sheet of Eccosorb AN75 absorber (manufactured by *Emerson and Cuming*) served as a matched load. For the frequency range 2 to 6 GHz, the copper sheet was translated 19 mm from the reference plane to provide the third standard. A 6.3 mm delay was used for frequencies between 6 and 18 GHz. As a check on measurement repeatability, the reflection coefficients of the short and match were remeasured after calibration. These measurements are shown in Fig. 4.5. The repeatability for the short is quite good; the magnitude varies only a tenth of a decibel while the phase is repeatable to 1°. Results are not as good for the absorber, particularly at the lower frequencies. At 2 GHz, the Eccosorb has a measured return loss of 7 dB. As frequency increases, the return loss improves and remains better than 12 dB.

To investigate the accuracy of the calibration, the copper sheet was translated 5 mm from the reference plane. Fig. 4.6 shows the measured reflection coefficient. Generally, the reflection coefficient behaves as expected. The measurement indicates that the magnitude of the reflection coefficient can be determined to about 1 dB and the phase to within a few degrees. Although these deviations are unacceptable for many applications, they are sufficient for determining the validity of the grid EMF models. Fig. 4.8 shows the reflection coefficient measured from a square 2.5 mm thick dielectric slab, 10 cm on a side. The dielectric is a ceramic polytetrafluoroethylene composite called *Duroid* manufactured by the Rogers Corporation [10]. It has a dielectric constant of 10.8 (±0.25) and copper

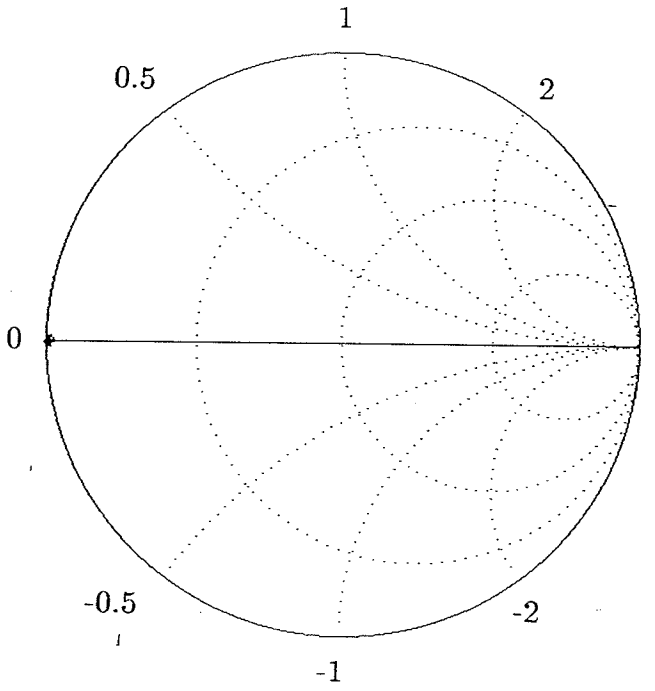

(a)

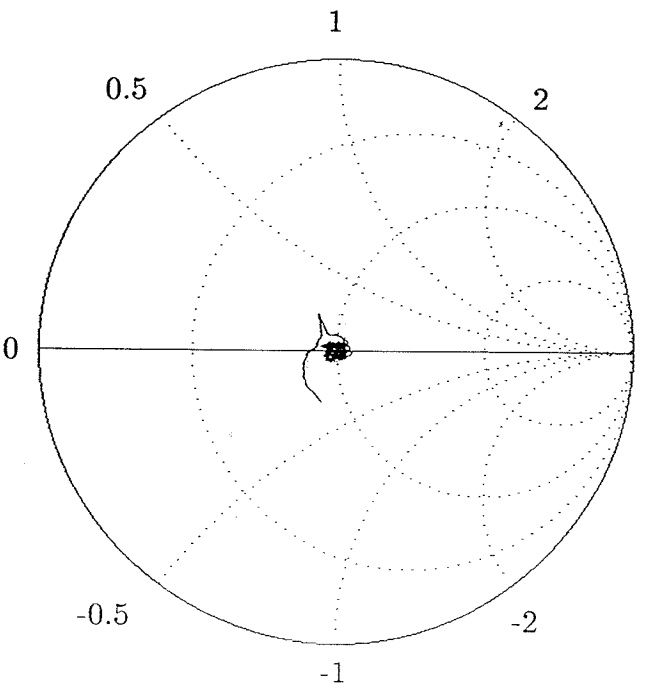

(b)

Figure 4.5 (a) Measured reflection coefficient of the short after calibration. (b) Reflection coefficient of the Eccosorb sheet. The frequency is swept from 2 to 18 GHz.

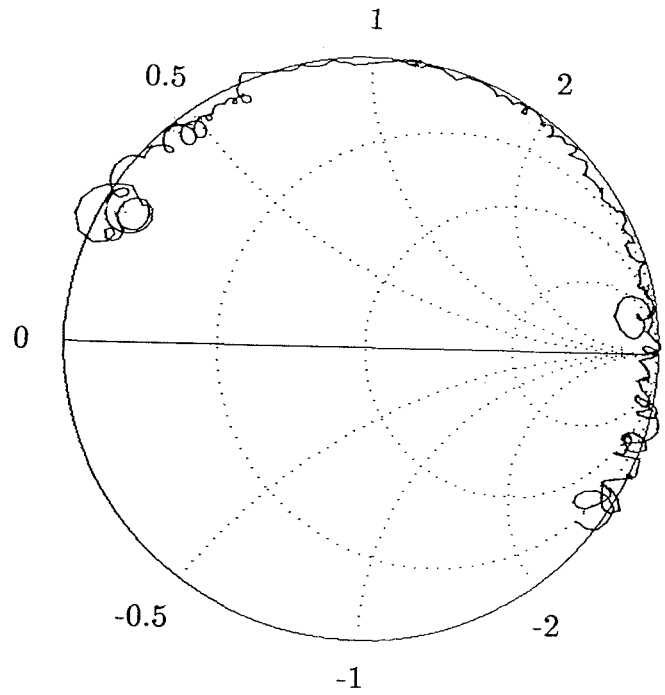

Figure 4.6 Measured reflection coefficient of a 5 mm delayed short.

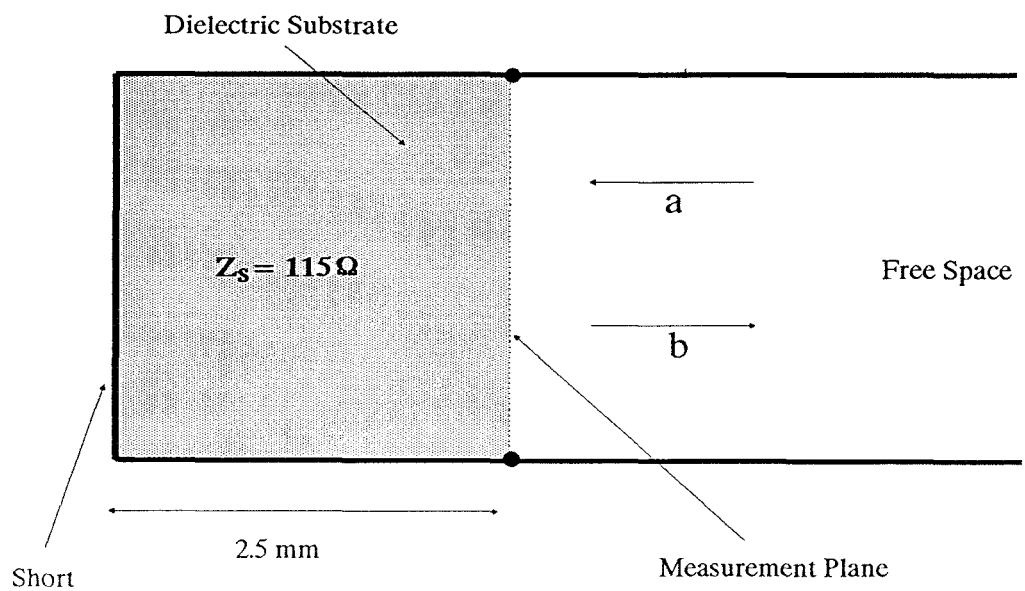

Figure 4.7 Transmission-line model for a 2.5 mm thick dielectric ($\epsilon_r = 10.8$) backed with copper cladding.

cladding on the back. A transmission-line model for the slab is shown in Fig. 4.7. The measurements in Fig. 4.8(a) and Fig. 4.8(b) indicate the transmission-line circuit is a valid model for the dielectric. As with the delayed short, there is considerable scatter in the measured data showing an uncertainty in the magnitude of the reflection coefficient of about 1.5 dB.

With some modifications, more accurate measurements can be made with the quasi-optical reflectometer. One source of error is wave diffraction. Waves incident on the grid surface do not have planar phase fronts, thus there is a phase difference between the wavefronts reflected from the center and edge of the grid. If the wave radiated from the horn is assumed to have a spherical phase front, this phase difference can be approximated by

$$\Delta\phi \approx \frac{\pi}{4}\,\frac{D^2}{\lambda_0 R} \quad \text{(radians)}, \tag{4.2}$$

where R is the wave radius of curvature and D is the diameter of the grid. From equation (4.2), we see that phase errors are less severe for longer wavelengths, smaller grids, and a large wave radius of curvature. To improve measurements, microwave dielectric lenses can be used to generate planar phase fronts. Using a biconvex lens and an X-band horn, Gagnon made very sensitive reflectometer measurements with essentially the same setup as shown in Fig. 4.3 [11].

Diffraction losses can lead to additional inaccuracies in quasi-optical reflection measurements. The free-space path loss from the horn to the measurement plane is included in the two-port error network. However, there is additional path loss associated with the delayed shorts. We can account for this by adding loss terms to the delays. Using this method, diffraction loss is included for the calibration standards, but loss for intermediate delays (i.e., measurements at planes not corresponding to a calibration standard) is not adequately modeled. Again, a focussing lens seems to be the most direct solution, as evidenced by the results of others [4, 11].

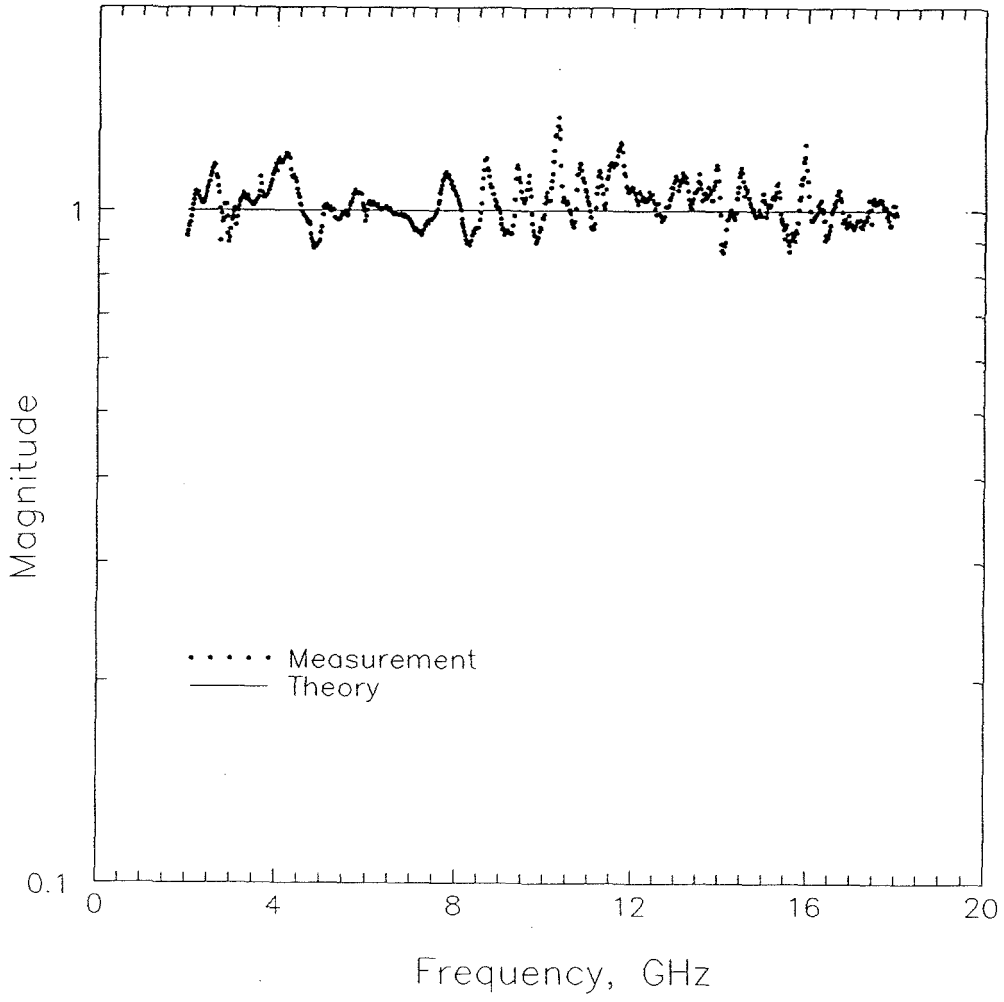

Figure 4.8(a) Magnitude of the reflection coefficient for the 2.5 mm thick dielectric slab. The dielectric constant of the slab is 10.8 and the loss tangent ($\tan \delta = 0.002$) is neglected.

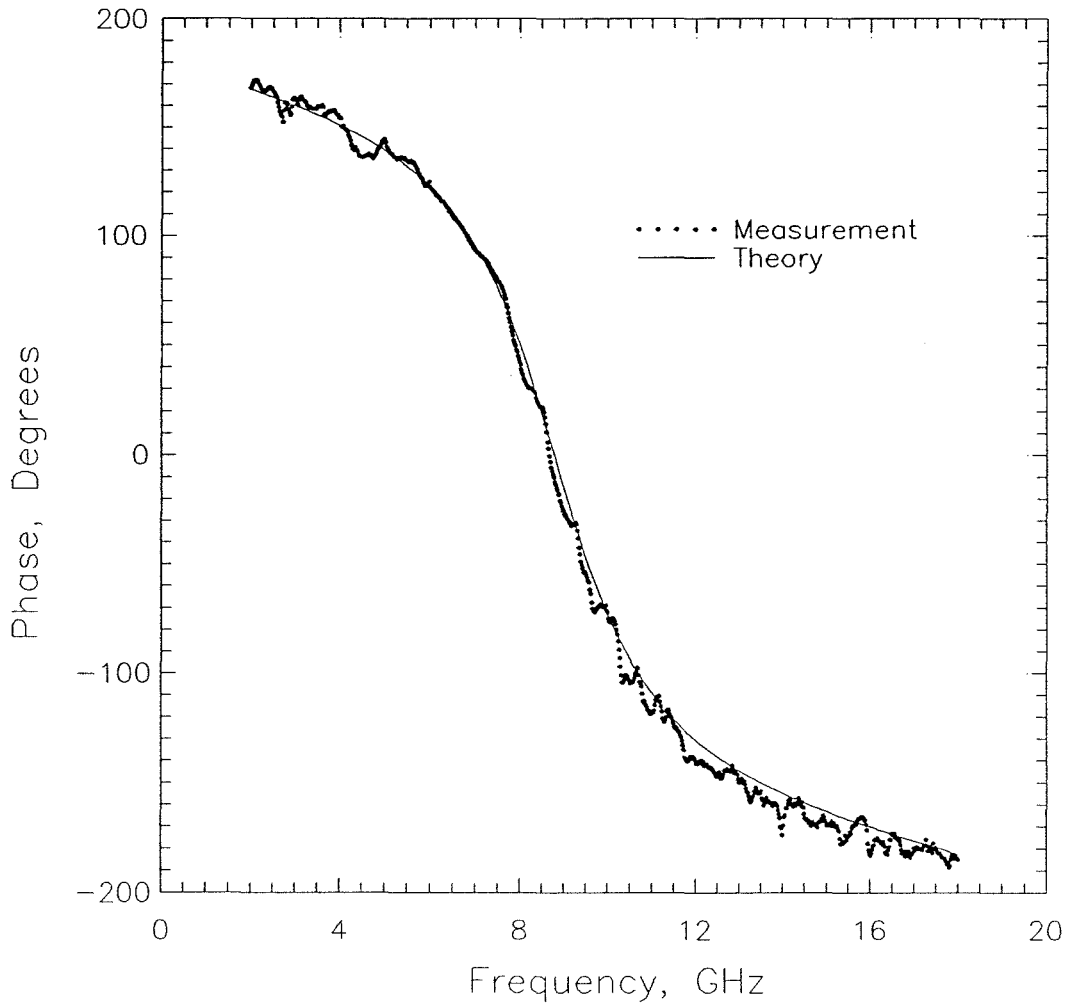

Figure 4.8(b) Phase of the reflection coefficient for the dielectric slab. The theoretical curve is obtained from the transmission-line model.

Measurement inaccuracy also arises from extraneous reflections within the anechoic chamber and misalignment of the horn antenna and grid. Elimination of these sources of error also permits more precise measurements.

4.4 Measurements on Planar Grids

In this section, we will present and discuss magnitude and phase reflection measurements for the planar grid configurations analyzed in chapters 2 and 3. These measurements are done with the quasi-optical reflectometer illustrated in Fig. 4.3. The grids are fabricated on 10 cm × 10 cm sheets of *Duroid* with copper cladding on the back [10]. To ensure the grids and calibration loads are the same size, the metallized back of the grids is used for the short and delayed short standards.

4.4.1 Inductive and Capacitive Grids

The inductive grid illustrated in Fig. 4.9(a) was fabricated on a 2.5 mm thick *Duroid* slab with $\epsilon_r = 10.5$. The vertical copper lines are 1 mm wide and separated by 7 mm. Equation (2.28) was used to calculate the reflection coefficient of the grid, which is modeled by the circuit in Fig. 4.9(b). Although the grid impedance is dispersive, at low frequencies it can be approximated with a (linear) lumped inductor. At 5 GHz, the grid has an inductance of 3.4 nH. Fig. 4.10 shows the measured and theoretical reflection coefficient. Both magnitude and phase response show reasonably good agreement with theory. As expected from the calibration check in section 4.3, there is an uncertainty in the magnitude response of about 1.5 dB. Fig. 4.11(a) shows a capacitive grid fabricated on a 1.27 mm thick Duroid substrate (also with $\epsilon_r = 10.5$). The gaps between the metal strips are 1 mm wide and spaced 5 mm apart. From equation (2.42), we calculate a grid capacitance of 320 fF at 5 GHz. The measured grid reflection coefficient is shown in Fig. 4.12(a) and Fig. 4.12(b).

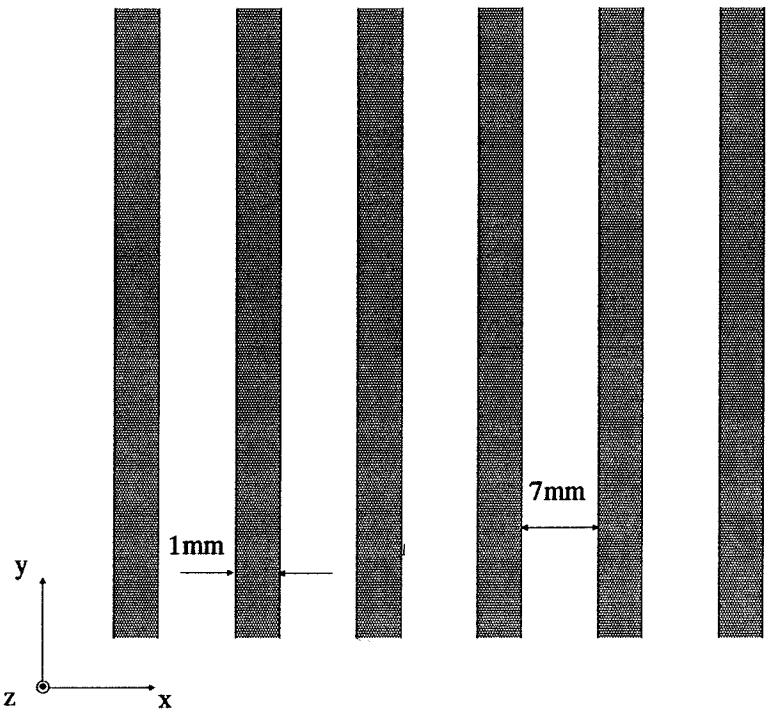

(a)

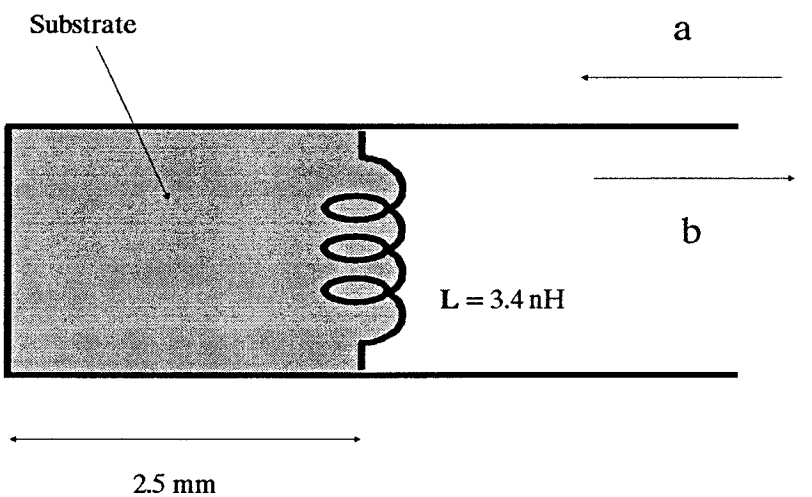

(b)

Figure 4.9 (a) Schematic of the inductive grid fabricated on *Duroid*. The dielectric constant is 10.5 and the back of the substrate is metallized. (b) Equivalent transmission-line model for the inductive grid.

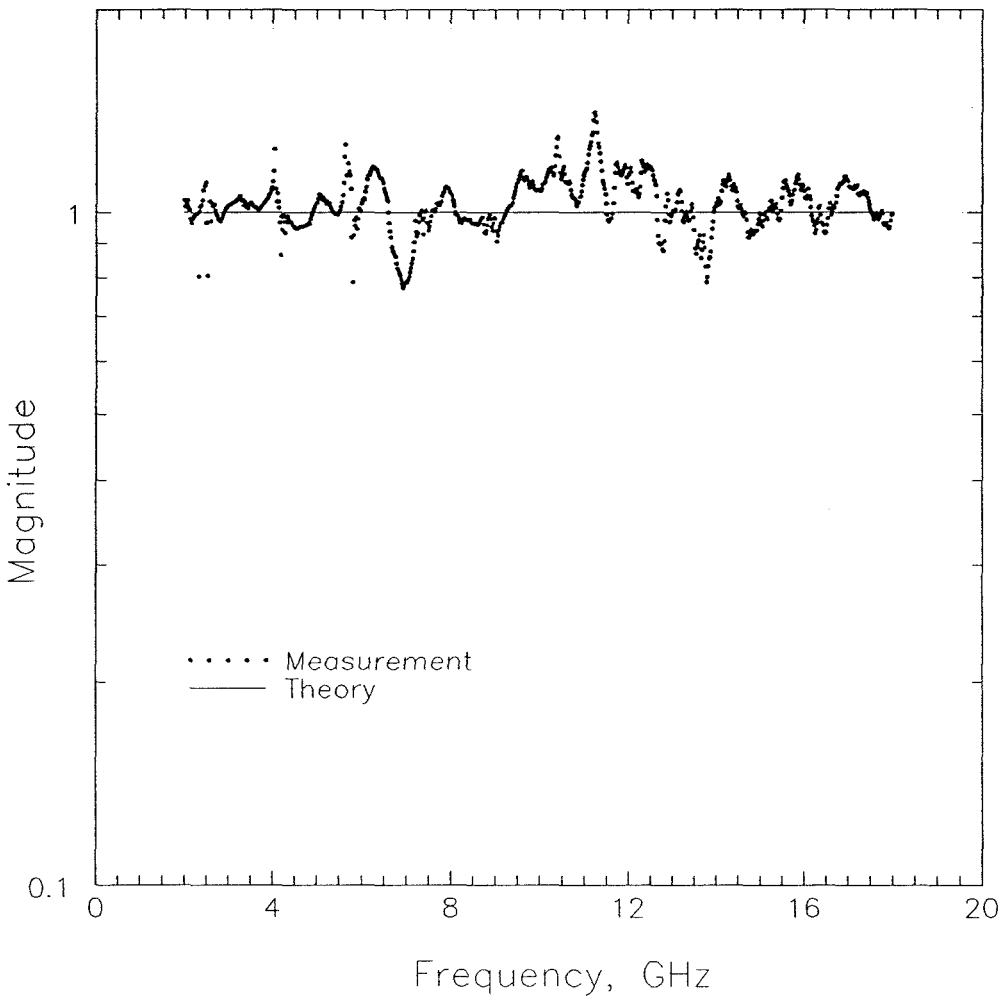

Figure 4.10(a) Magnitude response of the inductive grid.

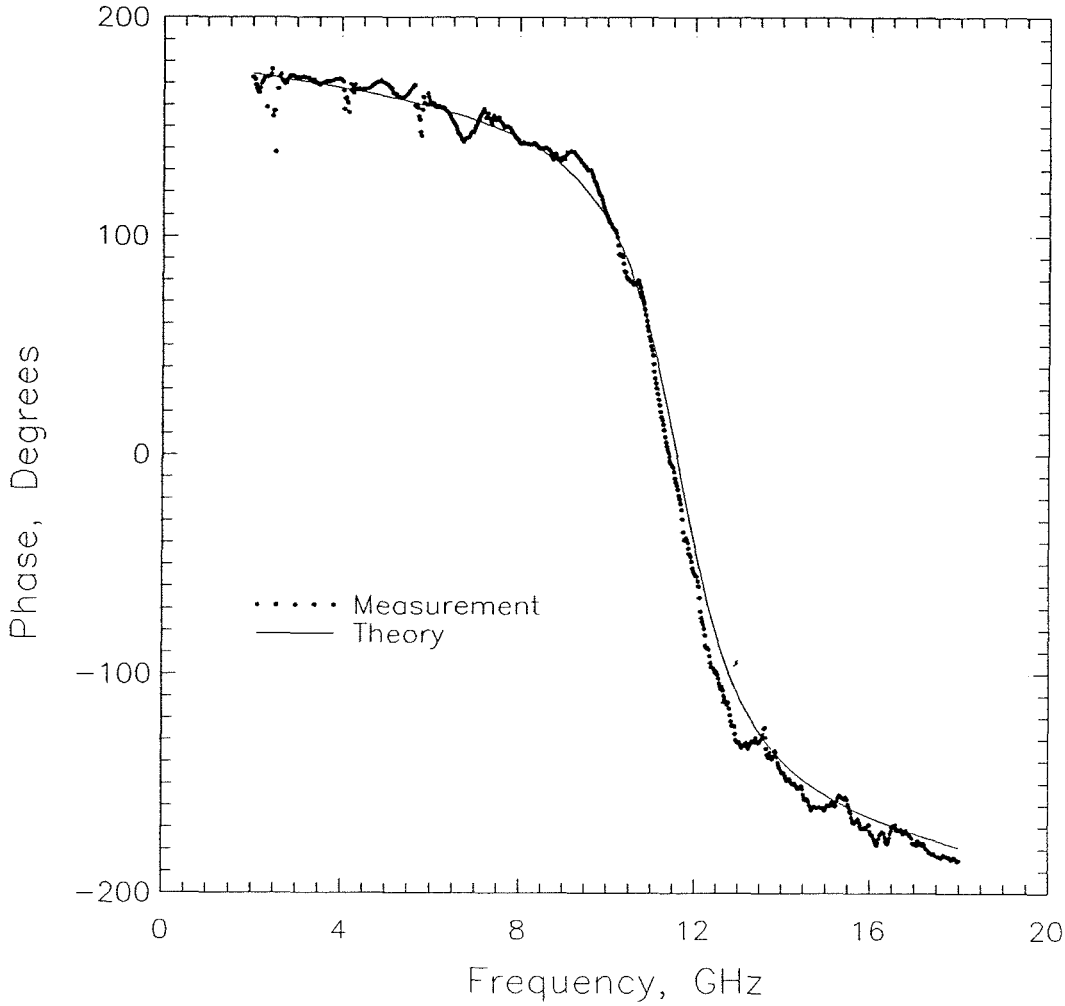

Figure 4.10(b) Phase response of the inductive grid.

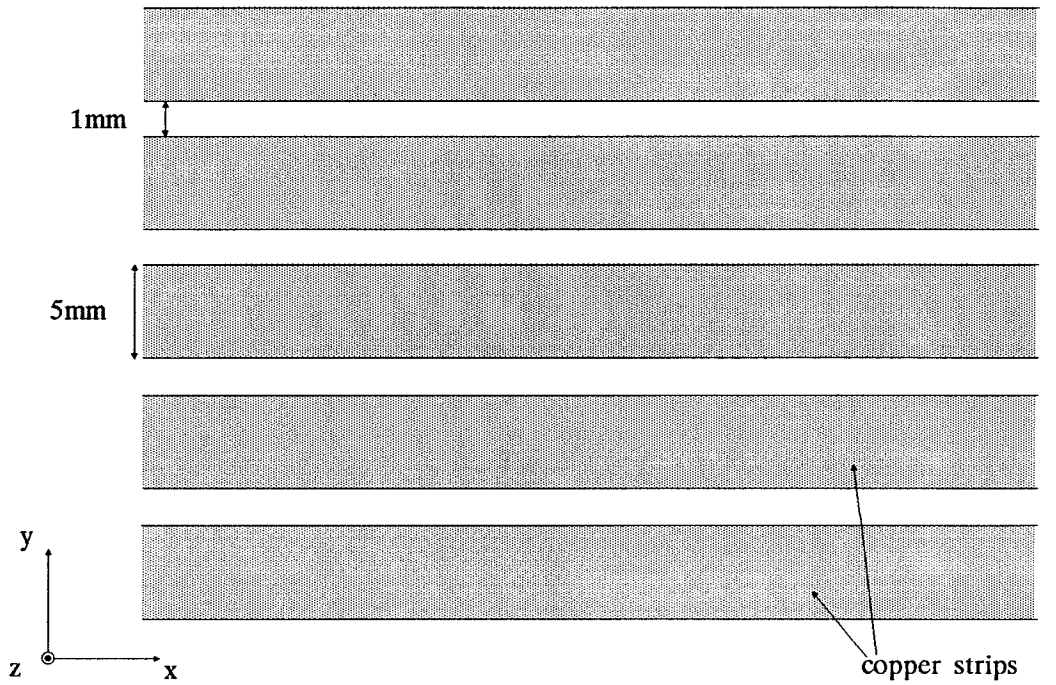

(a)

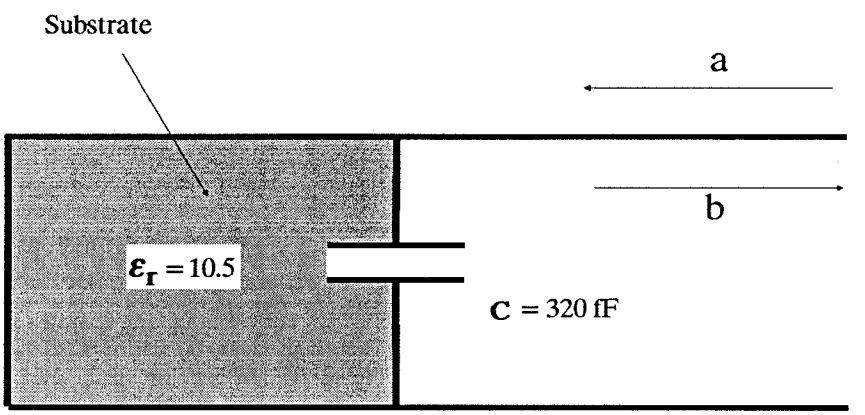

(b)

Figure 4.11 (a) Schematic of the capacitive grid fabricated on *Duroid*. The dielectric constant is 10.5 and the back of the substrate is metallized. (b) Equivalent transmission-line model for the capacitive grid.

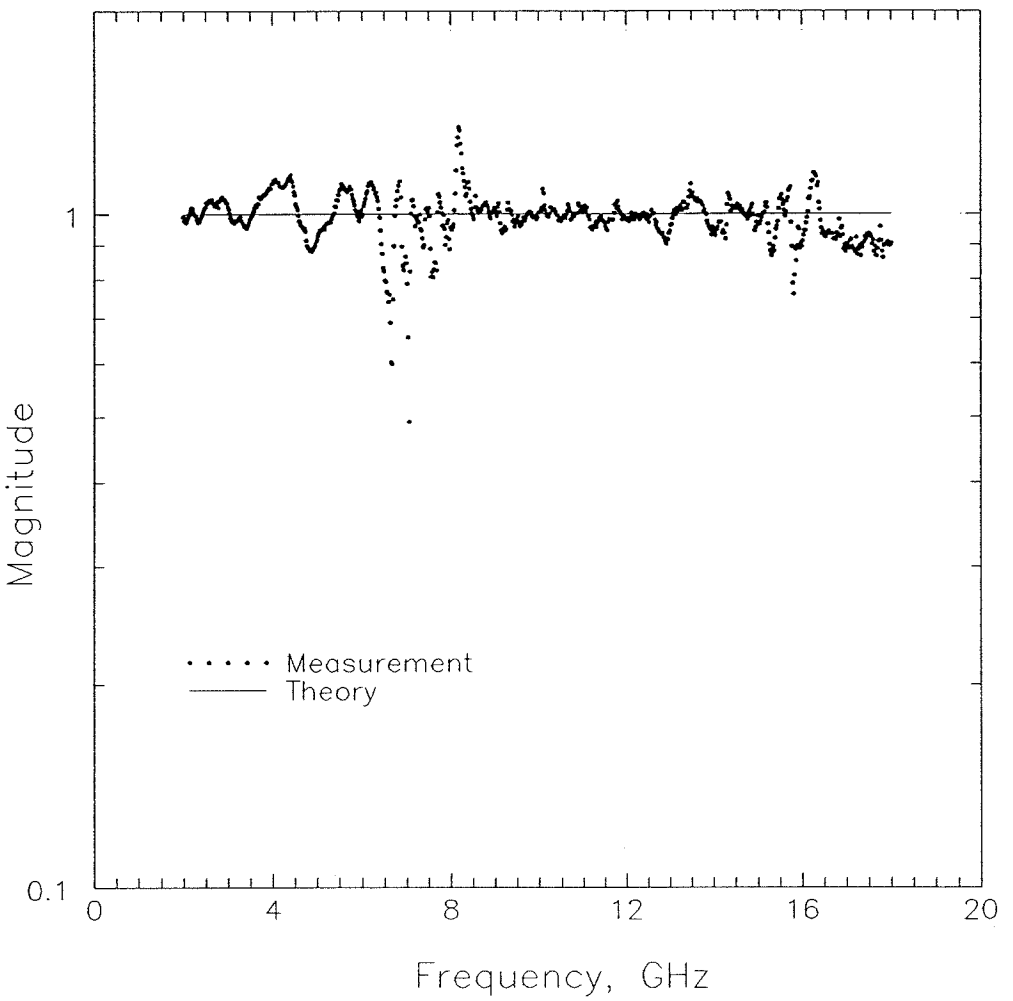

Figure 4.12(a) Magnitude response of the capacitive grid.

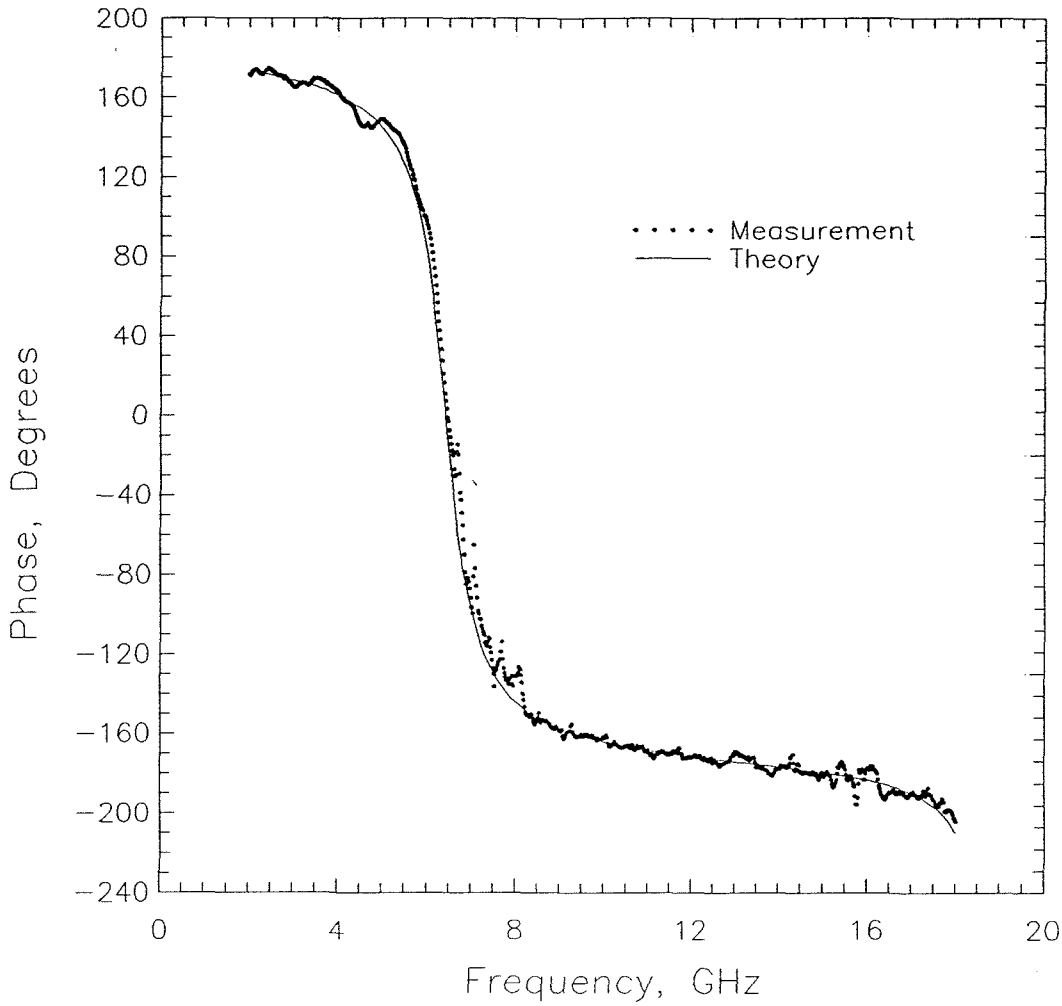

Figure 4.12(b) Phase response of the capacitive grid.

The measured phase of the grid reflection coefficient agrees quite well with the predicted phase. The magnitude response, however, shows 3 dB of loss near the grid resonance frequency (6.5 GHz). This variation in magnitude of the reflection coefficient is significantly larger than the expected scatter due to calibration error. It suggests there may be substantial loss in the grid. Investigation of the other grid configurations show there are indeed measurable loss mechanisms present in the grids.

4.4.2 Slot Grid

Fig. 4.13(a) shows the rectangular slot array. This grid, which was fabricated on a 2.5 mm thick *Duroid* substrate with $\epsilon_r = 10.5$, is modeled with the parallel resonant circuit of Fig. 4.13(b). The slots are 3 mm wide, 5 mm long and are separated in the x-direction by 1 mm and in the y-direction by 3 mm. Equations (3.10) and (3.11) are used to compute values for the reactive elements in the transmission-line model. Measured and theoretical responses for the grid reflection coefficient are shown Fig. 4.14(a) and 4.14(b). Examining the phase response in Fig. 4.14(a), we note the transmission-line model predicts a resonance where the phase changes by 360° at 11 GHz and 16.5 GHz. The model, which assumes the grid is lossless, is in good agreement up to the second resonance, but fails to predict the phase response at 16 GHz. The magnitude of the measured reflection coefficient, shown in Fig. 4.14(b), shows 7 dB of loss at the second resonance. These measurements clearly indicates that the loss is real and not merely a result of calibration error. The loss is large enough to prevent the phase from making a full 360° swing at 16 GHz. This is illustrated on the Smith Chart plot of Fig. 4.15(a). We can model the loss by placing a resistor in the transmission-line circuit as shown in Fig. 4.15(b). By choosing an approriate value for the resistor, we get good agreement between the measured reflection coefficient and the "lossy" circuit model. In section 4.5, grid losses will be examined in more detail.

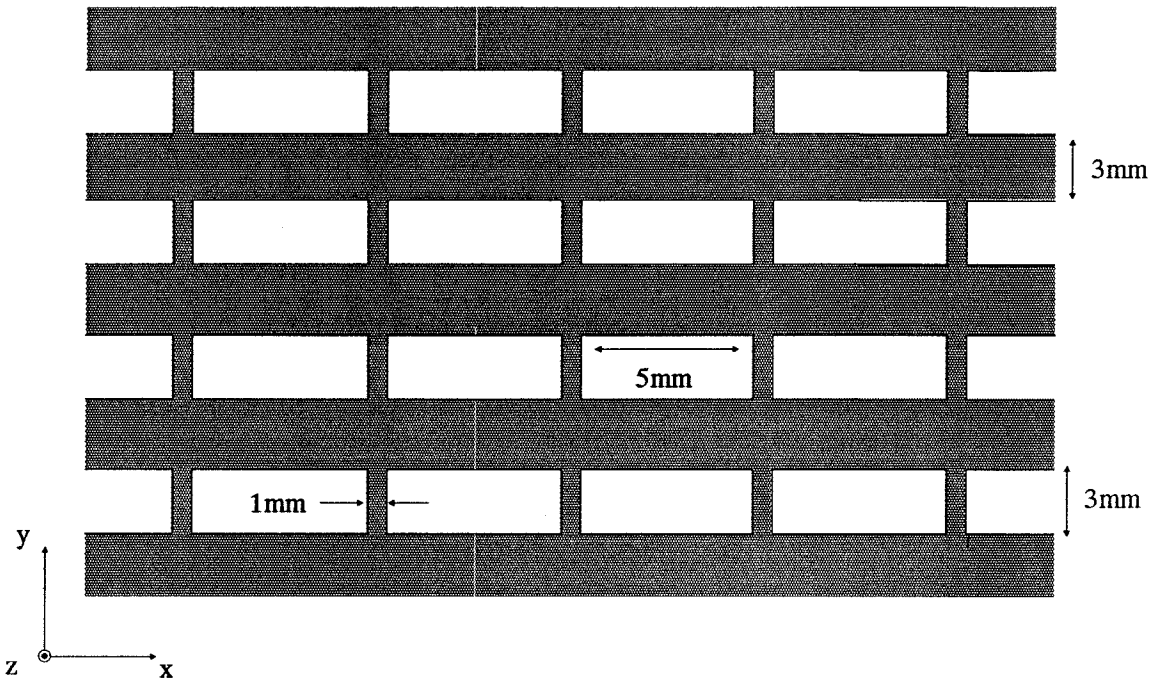

(a)

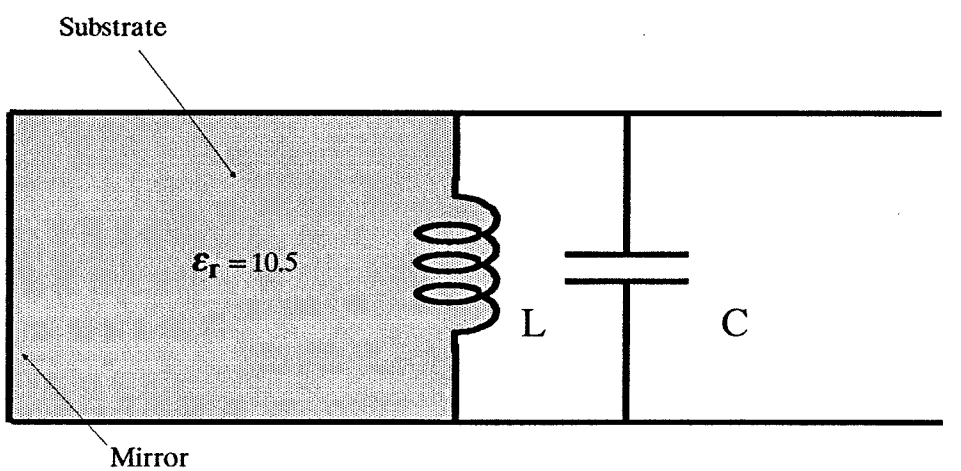

(b)

Figure 4.13 (a) Schematic of the slot grid. The substrate is *Duroid* and has a dielectric constant of 10.5. (b) Transmission-line model for the slot grid.

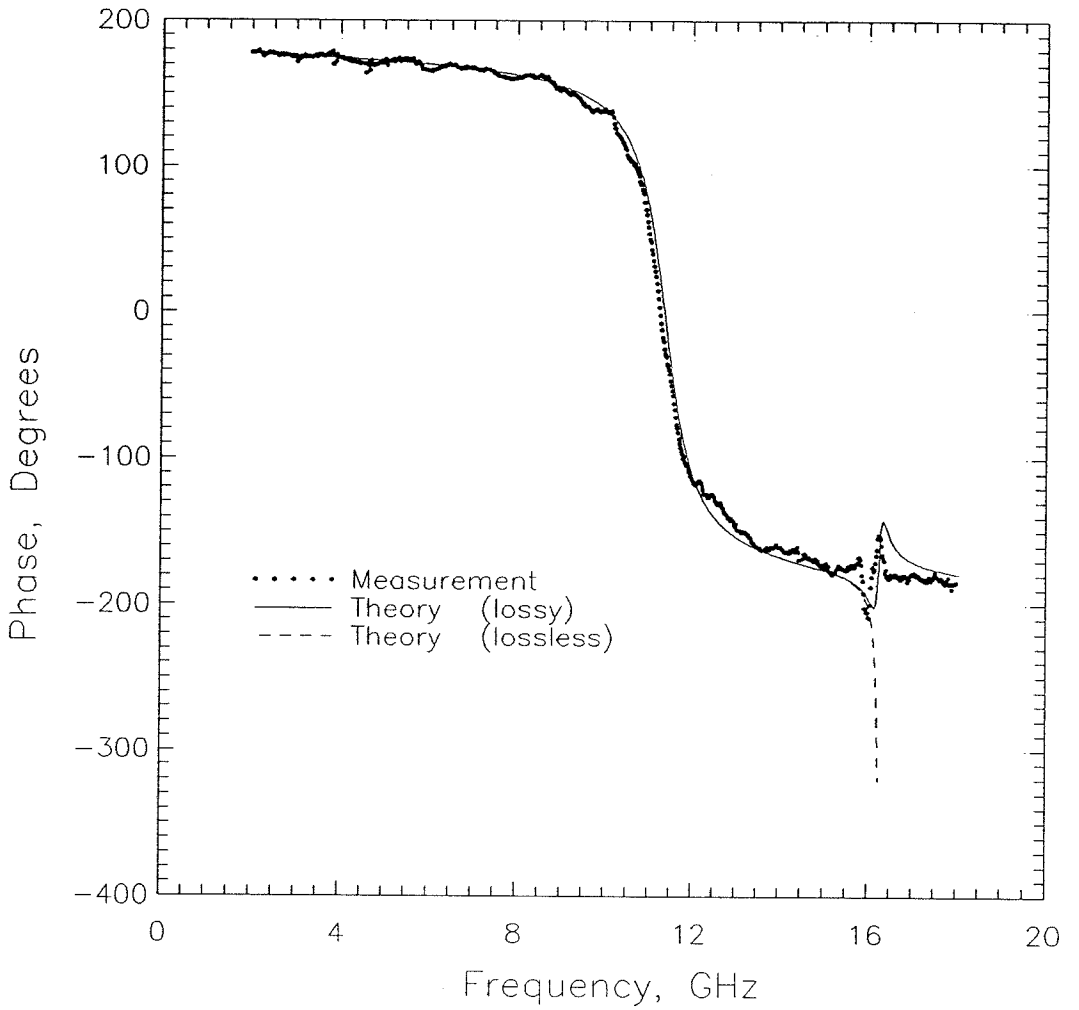

Figure 4.14(a) Phase response for the slot grid. The "lossless" model for the grid is shown in Fig. 4.13(b) and the "lossy" model is shown in Fig. 4.15(b).

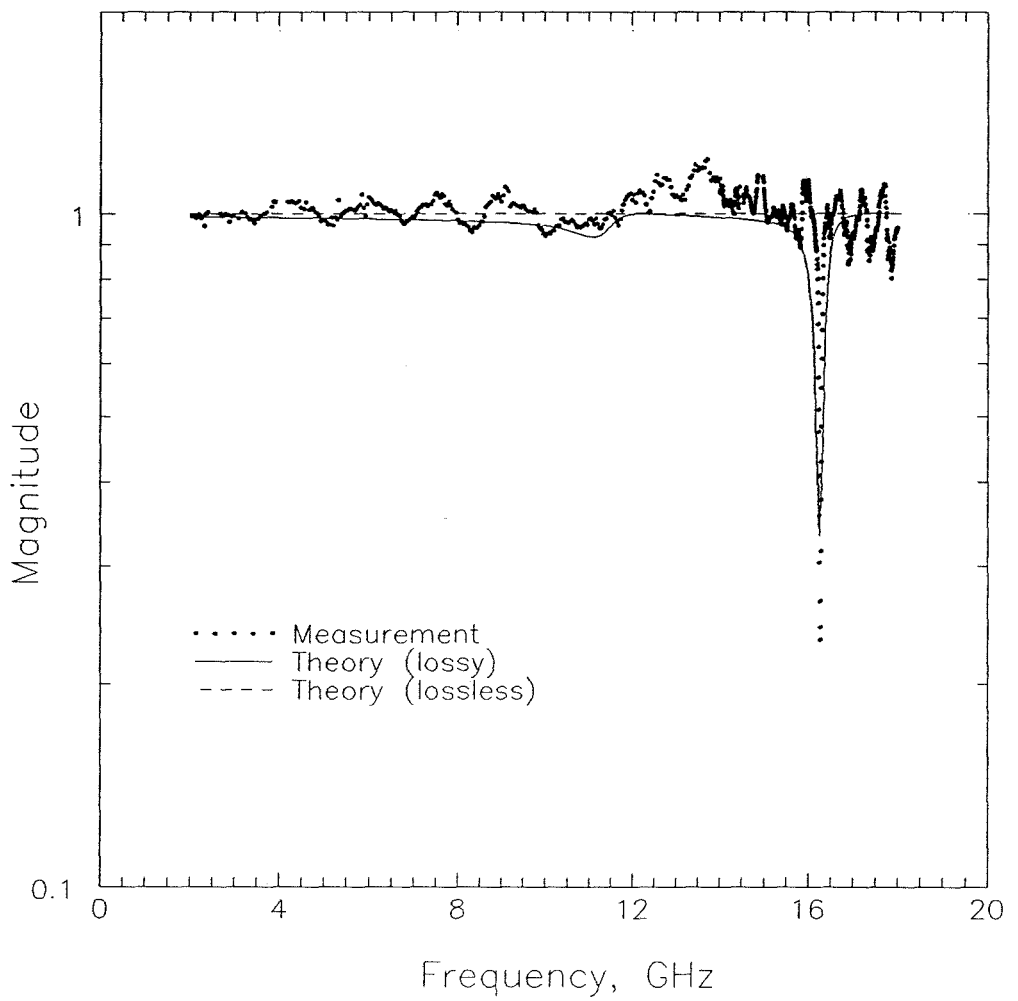

Figure 4.14(b) Magnitude response of the slot grid showing 7 dB of loss at the second resonance (16.5 GHz).

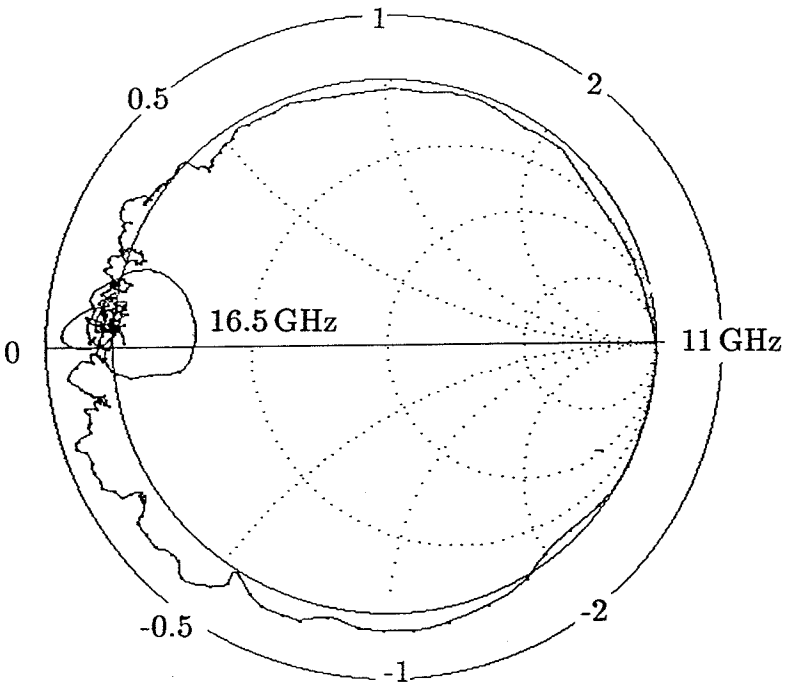

(a)

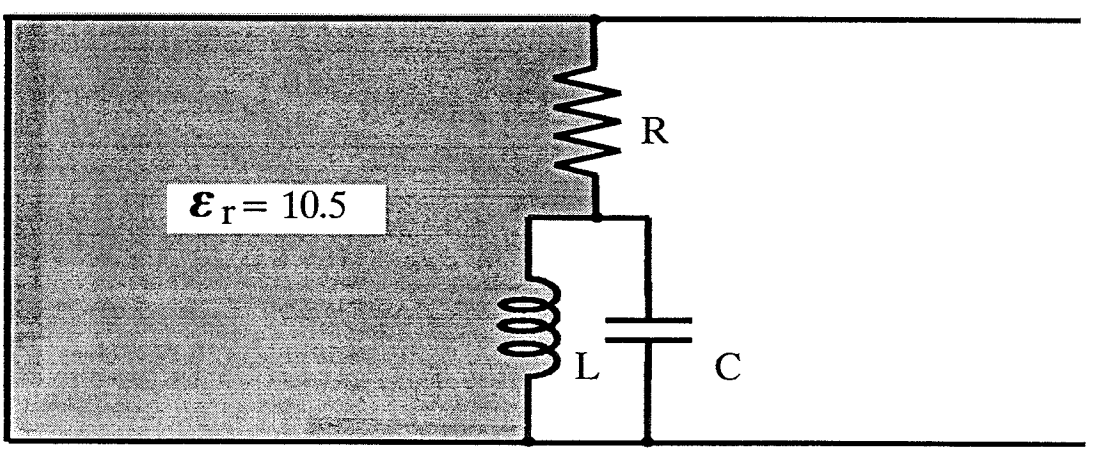

(b)

Figure 4.15 (a) Reflection coefficient of the slot grid. (b) Lossy model of the slot grid. An 8 Ω resistor is added to the circuit to model the loss at 16.5 GHz.

4.4.3 Bow-tie Grid

In chapter 3, we found that a bow-tie grid could be modeled with a section of transmission line. To check the validity of this model, the grid shown in Fig. 4.16 was built and its reflection coefficient measured. A shorting strip appears across the apex of the bow-ties, which have a flair angle of 45° and a diagonal length of 5 mm (corresponding to a 3.5 mm × 3.5 mm unit cell). With these dimensions and a 2.5 mm thick substrate ($\epsilon_r = 10.5$), the EMF analysis gives a bow-tie characteristic impedance of 78 Ω and an electrical length of 65° at 10 GHz. The measured and theoretical reflection coefficients for the grid are shown in Fig. 4.17. As with the slot grid, there are two resonances predicted by the EMF model. There is good agreement between the model and measured data up to 13 GHz, but the EMF method fails to correctly predict the second resonance. For comparison, the bow-tie unit cell was also analyzed using Hewlett Packard's *High-Frequency Structure Simulator* (HFSS) [12]. The structure simulator correctly predicts the measured response over the whole frequency range, indicating that the EMF model breaks down above 13 GHz.

It is interesting to note that the lowest order TM and TE modes for the bow-tie unit cell equivalent waveguide begin to propagate in the dielectric at 13.2 GHz. Above this frequency, the bow-tie inductance and capacitance start to change rapidly and this may be responsible for the discrepancy between measurement and the EMF model. As a check, a square bow-tie grid with a smaller unit cell dimension (a = b = 1.5 mm) was analyzed using the HFSS and compared to the EMF model. For this grid structure, the lowest order TE and TM modes have a cut-on frequency of 30 GHz. The results, shown in Fig. 4.18, are in good agreement and indicate that the EMF transmission-line model is valid as long as the high-order TE and TM modes are evanescent.

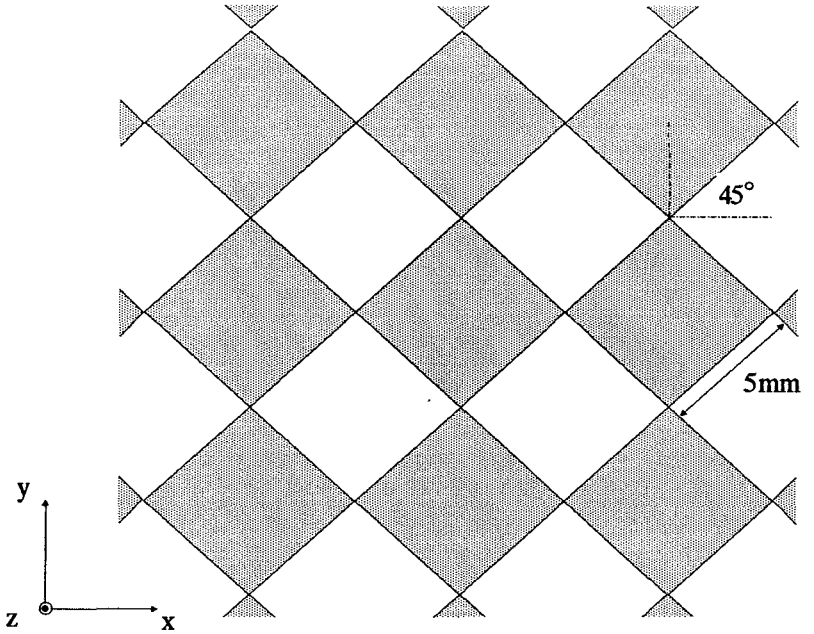

(a)

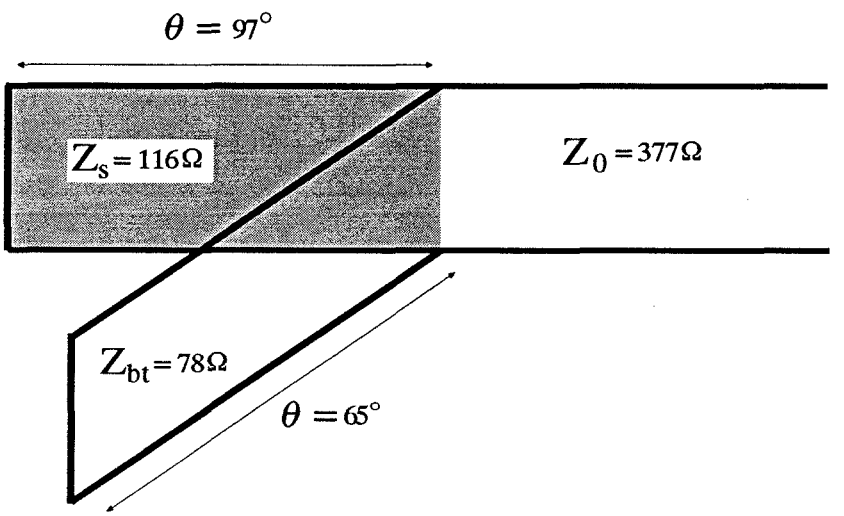

(b)

Figure 4.16. (a) Schematic of the bow-tie grid. (b) Bow-tie grid transmission-line model. The electrical length of the transmission lines are specified at 10 GHz.

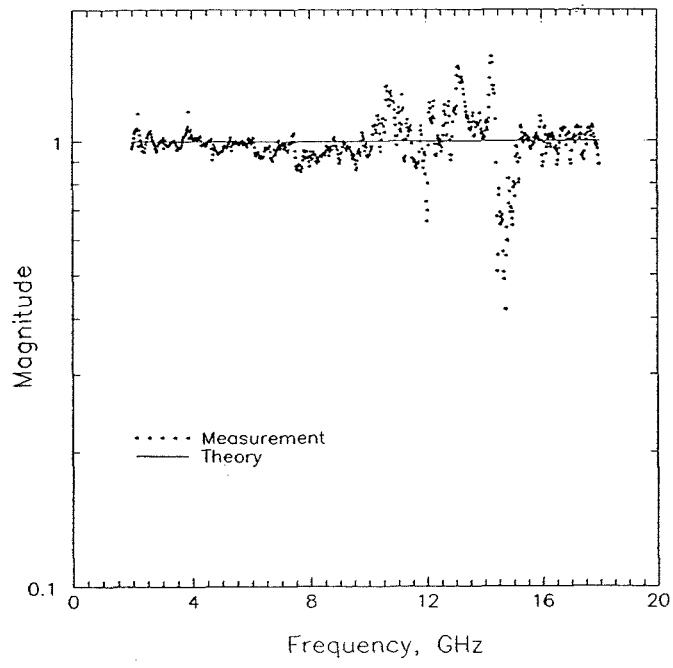

(a)

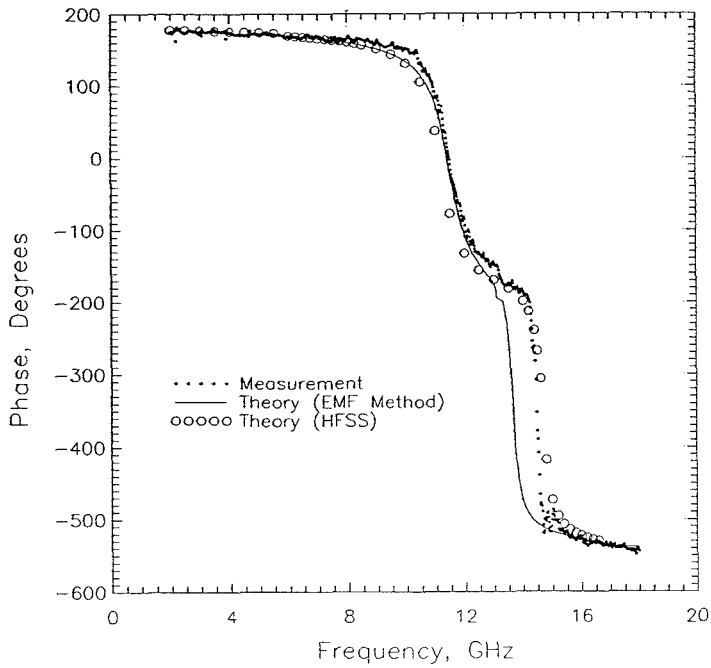

(b)

Figure 4.17 (a) Magnitude of the bow-tie grid reflection coefficient. The measurement shows loss at the grid resonant frequencies. The transmission-line model assumes no losses. (b) Phase of the bow-tie grid reflection coefficient. Theoretical curves obtained from the EMF model and *High-Frequency Structure Simulator* (HFSS) are shown for comparison.

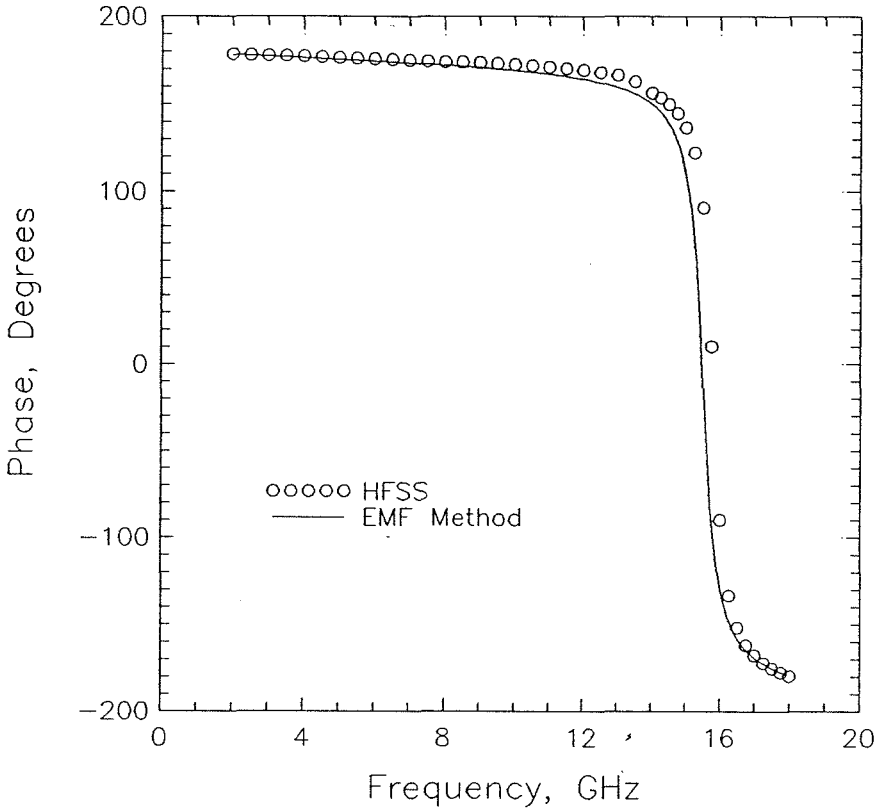

Figure 4.18 Predicted phase response for a shorted bow-tie grid with bow flair angle of 45° and unit cell dimension of 1.5 mm. The substrate is 2.5 mm thick and has $\epsilon_r = 10.5$.

4.4.4 Planar Transistor Grid Configuration

Compared to the grids discussed thus far, the planar transistor grid configuration, shown in Fig. 3.7, has a slightly more complicated transmission-line model. The major features of the model (shown in Fig. 3.10) are the three input terminals and a center-tapped transformer. To experimentally investigate the equivalent circuit models for the rectangular slot and bow-tie grids, shorts are placed across the grid input terminals and the grid reflection coefficient is

measured. This can also be done with the transistor grid, but, because there are three terminals, two different grid measurements are required. The idea is illustrated in Fig. 4.19 and 4.21.

Fig. 4.19(a) shows a planar transistor grid in which the devices are replaced with shorting strips. It is similar to the slot grid of Fig. 4.13, except that the slots are much wider than the horizontal metal strips. As a result, the capacitance between the metal strips (bias lines) is neglected. The grid equivalent circuit is given in Fig. 4.19(b). An electric field polarized in the y-direction induces current on the vertical metal strips and allows us to measure the grid's lead inductance, L. This grid, however, does not permit measurement of the reactive elements, L_m and C_m, in the center lead. The measured and theoretical phase of the grid reflection coefficient, shown in Fig. 4.20, are in good agreement.

To measure the reactive elements L_m and C_m, it is necessary to prevent the currents induced on the grid from flowing along the vertical leads. In other words, we can measure L_m and C_m by open-circuiting one of the terminals and shorting the other. The grid illustrated in Fig. 4.21(a) accomplishes this by eliminating one of the vertical leads in the equivalent waveguide. The center-tapped transformer then becomes the $1 : 2$ transformer shown in Fig. 4.21(b). Because the model has an inductor and capacitor connected in series, we refer to this as a "series-resonant" grid. With this grid, a vertically polarized wave induces currents on the vertical strips which also flow along the horizontal strips. As a result, this configuration permits measurement of the reactive elements in the center lead. The measured phase of the reflection coefficient for this grid, shown in Fig. 4.22, is in good agreement with theory. As a result, the transmission-line circuit of Fig. 3.10 is a valid model for the planar transistor grid.

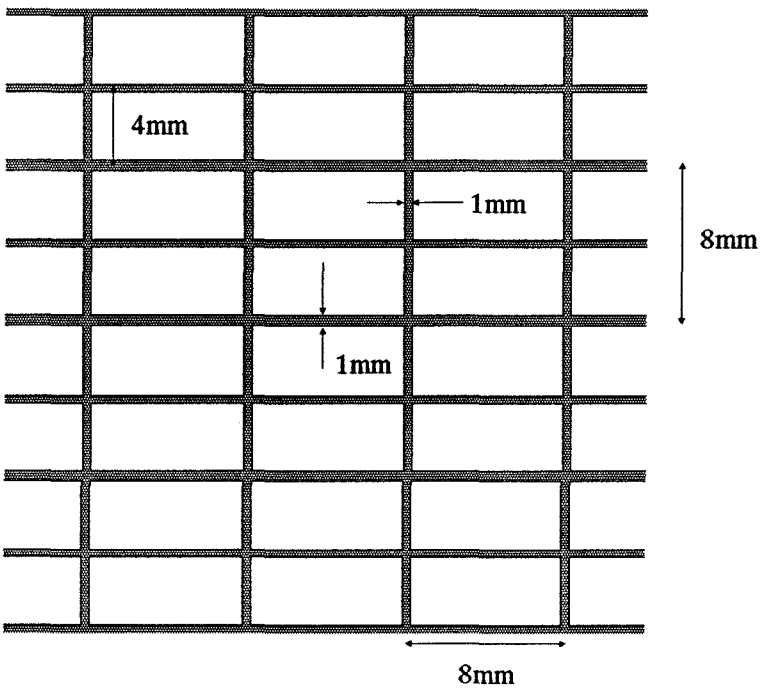

(a)

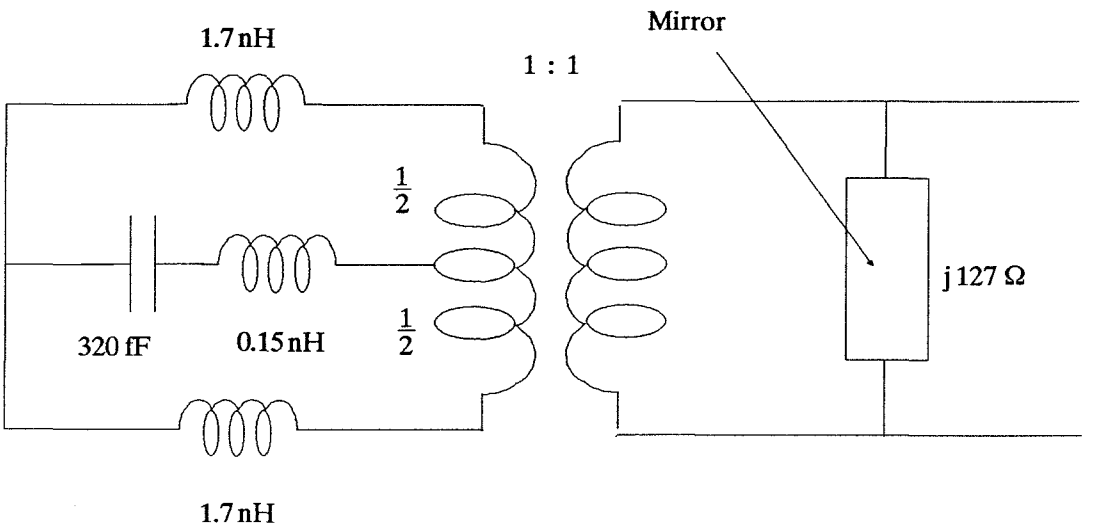

(b)

Figure 4.19 (a) Configuration used to measure the lead inductance of the transistor grid. The substrate is 2.5 mm thick and has a dielectric constant of 10.5. The grid dimensions are indicated on the diagram. (b) Transmission-line model for the grid in Fig. 4.19(a). Values for the circuit elements are specified for 5 GHz.

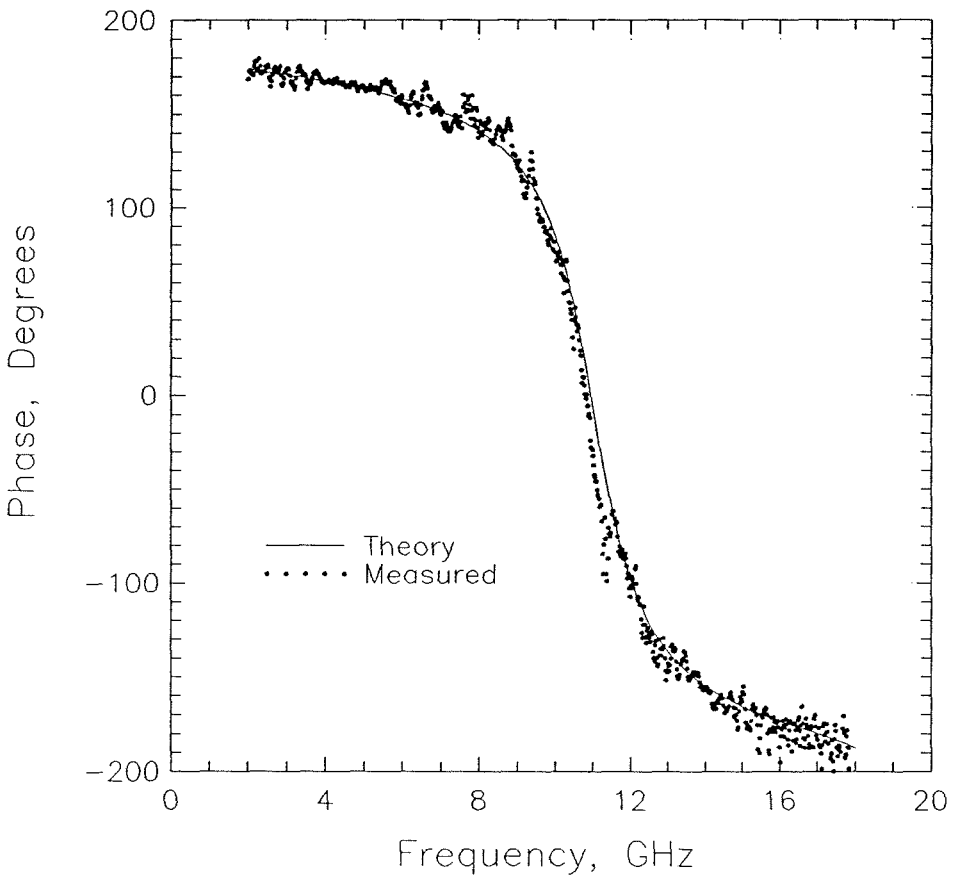

Figure 4.20 Phase of the reflection coefficient for the inductive grid of Fig. 4.19.

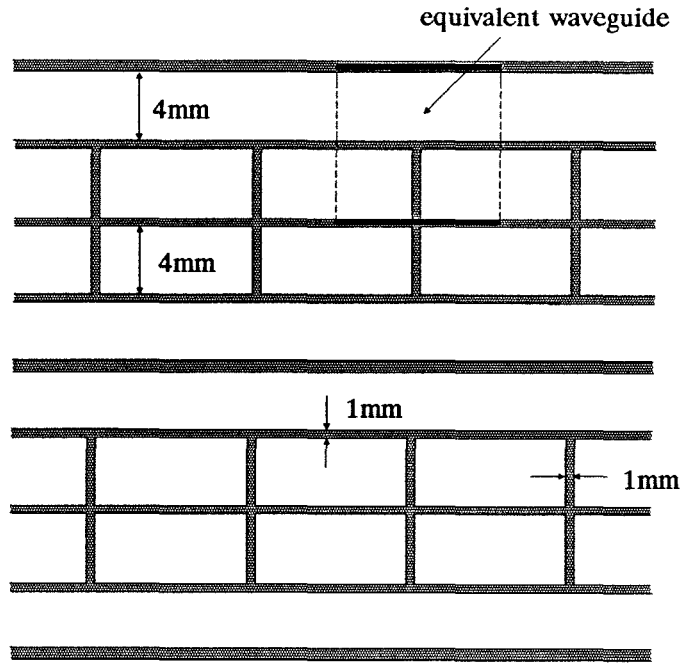

(a)

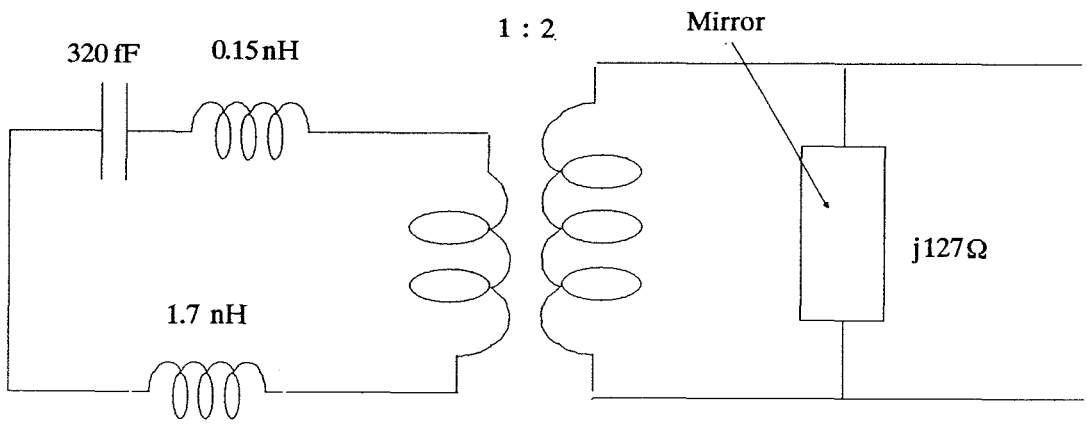

(b)

Figure 4.21 (a) Configuration used to measure the center-lead impedance of the transistor grid. (b) Transmission-line model for the grid in Fig. 4.21(a). Values for the circuit elements are specified at 5 GHz.

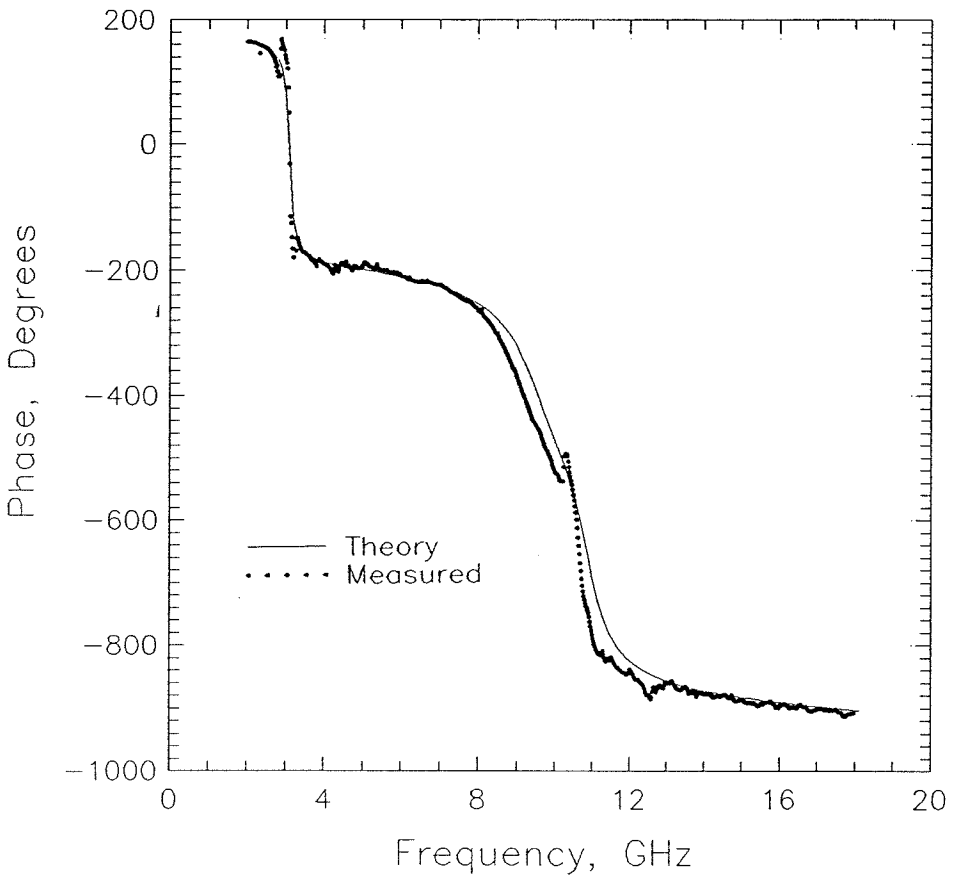

Figure 4.22 Phase of the reflection coefficient for the series-resonant grid of Fig. 4.21.

4.5 Losses

Reflection measurements for several of the passive grids show that at certain frequencies a substantial amount of power is lost. The frequencies where this loss occurs corresponds to the resonant frequencies of the grids. Furthermore, we found that this loss can be taken into account by including a resistor in the grid equivalent circuit model. Fig. 4.23(a) shows a modified transmission-line model for the series-resonant grid of Fig. 4.21(a). A $10\,\Omega$ resistor is added to model the losses. The resulting response is compared to measurement in Fig. 4.23(b).

The magnitude of the measured losses is somewhat unexpected. The substrate material has a very low loss tangent (the manufacturer specifies $\delta \approx 0.0028$ up to 10 GHz) and the dielectric slab reflection measurement of section 4.3 shows no discernible loss. Dissipation due to the finite conductivity of copper is another possibility. Copper's surface resistivity is given by [13]:

$$R_s = 2.61 \times 10^{-7}\sqrt{f}\ \Omega \tag{4.3}$$

where f is frequency measured in Hertz. The metal strips in the unit cell have an aspect ratio of 8:1, giving a resistance of about $0.2\,\Omega$ at 10 GHz. This is also too small to account for the measured losses. A third possibility is that power is being coupled into surface waves. Lam [14] argued that surface wave excitation can be avoided if the grid period, a, is chosen such that:

$$a < \frac{\lambda_0}{(n+1)} \tag{4.4}$$

where λ_0 is the free-space wavelength and n is the substrate's refractive index. From this criterion, we expect grids fabricated on substrates with $\epsilon_r = 10.5$ to excite substrate modes only at frequencies above 8.8 GHz. Pursuing this idea, a series-resonant grid was fabricated on a substrate of dielectric constant 2.2. Because of the low dielectric constant, substrate modes should be excited at higher frequencies (greater than 15 GHz). The magnitude and phase of the reflection

coefficient (Fig. 4.24) show the grid to have 10 dB of loss at 6 GHz. There is also substantial loss at 3 GHz for the grid built on *Duroid* with $\epsilon_r = 10.5$. As an additional check, a horn antenna was positioned to measure any radiation leaking out the sides of the grid. None was detected, indicating that the power is dissipated in the grid itself.

One grid configuration which exhibits no measurable loss is the inductive grid discussed in section 4.4.1 and illustrated in Fig. 4.9. This grid, like the others, lies on a *Duroid* substrate with dielectric constant of 10.5. Therefore, it seems reasonable to postulate that the loss mechanism depends primarily on the grid structure. The inductive grid differs from the other configurations in that there are no horizontal metal lines running across the substrate. If these lines are indeed responsible for the measured losses, then it seems plausible that placing gaps along them should decrease these losses. This idea is illustrated in Fig. 4.25. Gaps 1 mm wide are placed along the horizontal lines at the edges of the grid equivalent waveguide. Because magnetic walls are supposed to exist along these unit cell boundaries, the gaps should not effect the grid reflection coefficient. The measured response for this grid is shown in Fig. 4.26. The loss at 6 GHz has decreased by more than 7 dB and the phase response is much smoother than before. These measurements indicate that the losses probably arise from power coupling into transverse modes which propagate along the horizontal metal lines.

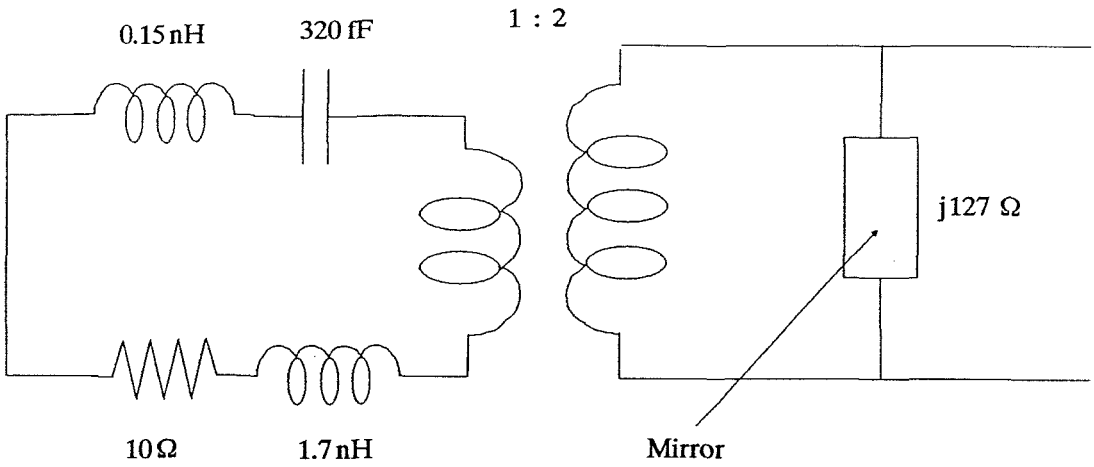

(a)

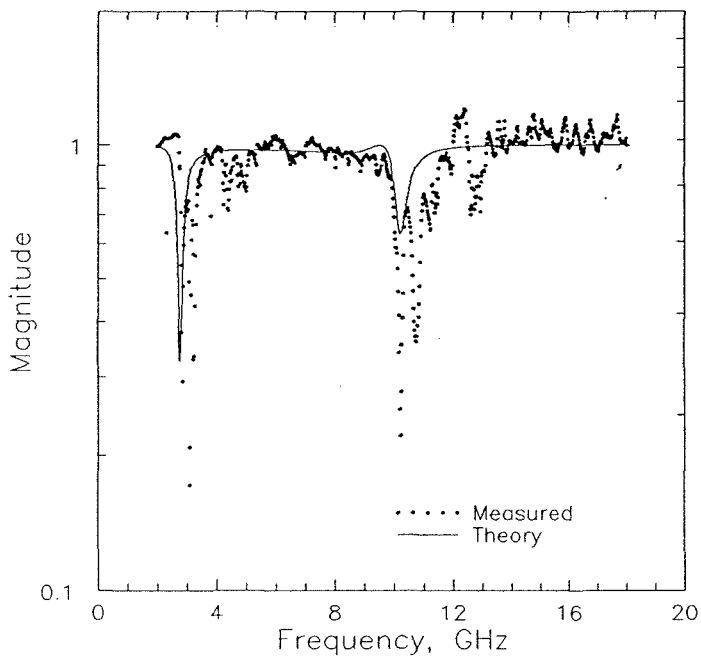

(b)

Figure 4.23 (a) Transmission-line model for the series-resonant grid with a resistor included to model losses. (b) Magnitude of the reflection coefficient for the series-resonant grid.

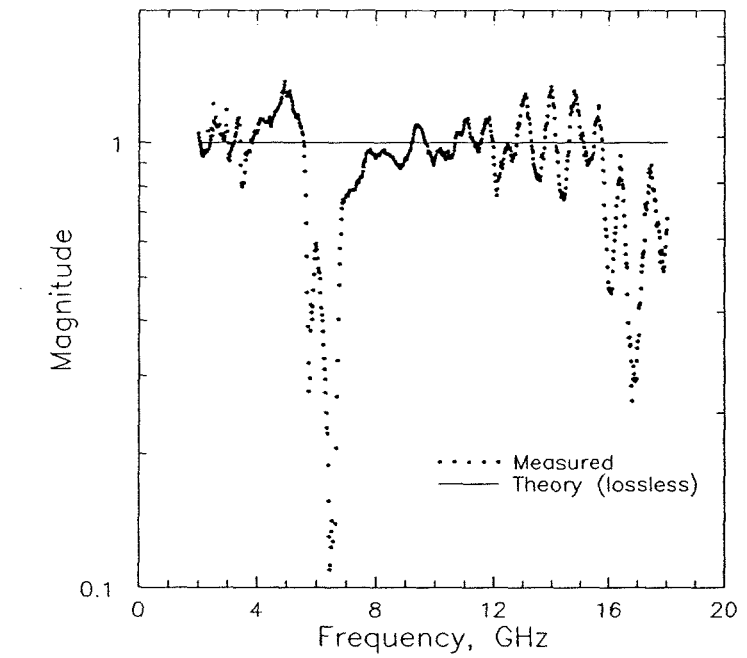

(a)

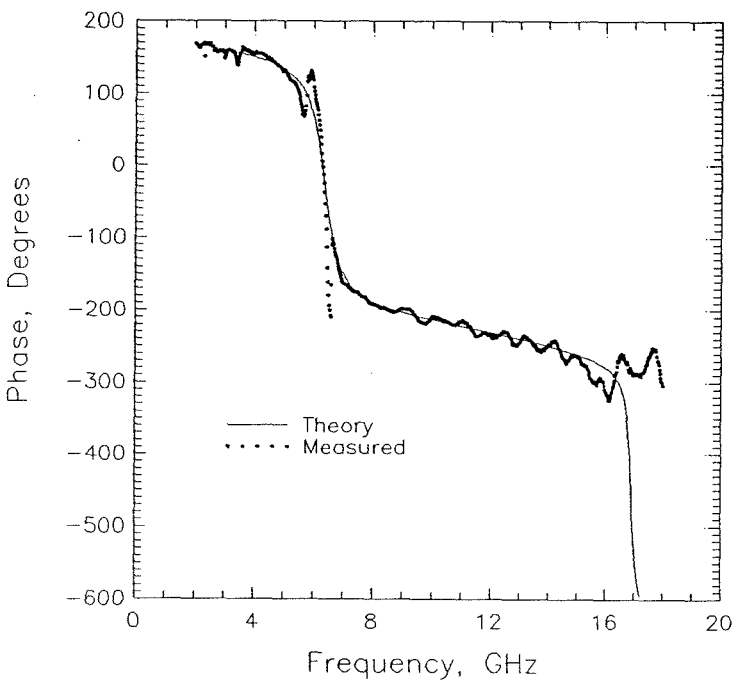

(b)

Figure 4.24 (a) Reflection coefficient magnitude for a series-resonant grid fabricated on *Duroid* with $\epsilon_r = 2.2$. (b) Phase response of the series-resonant grid.

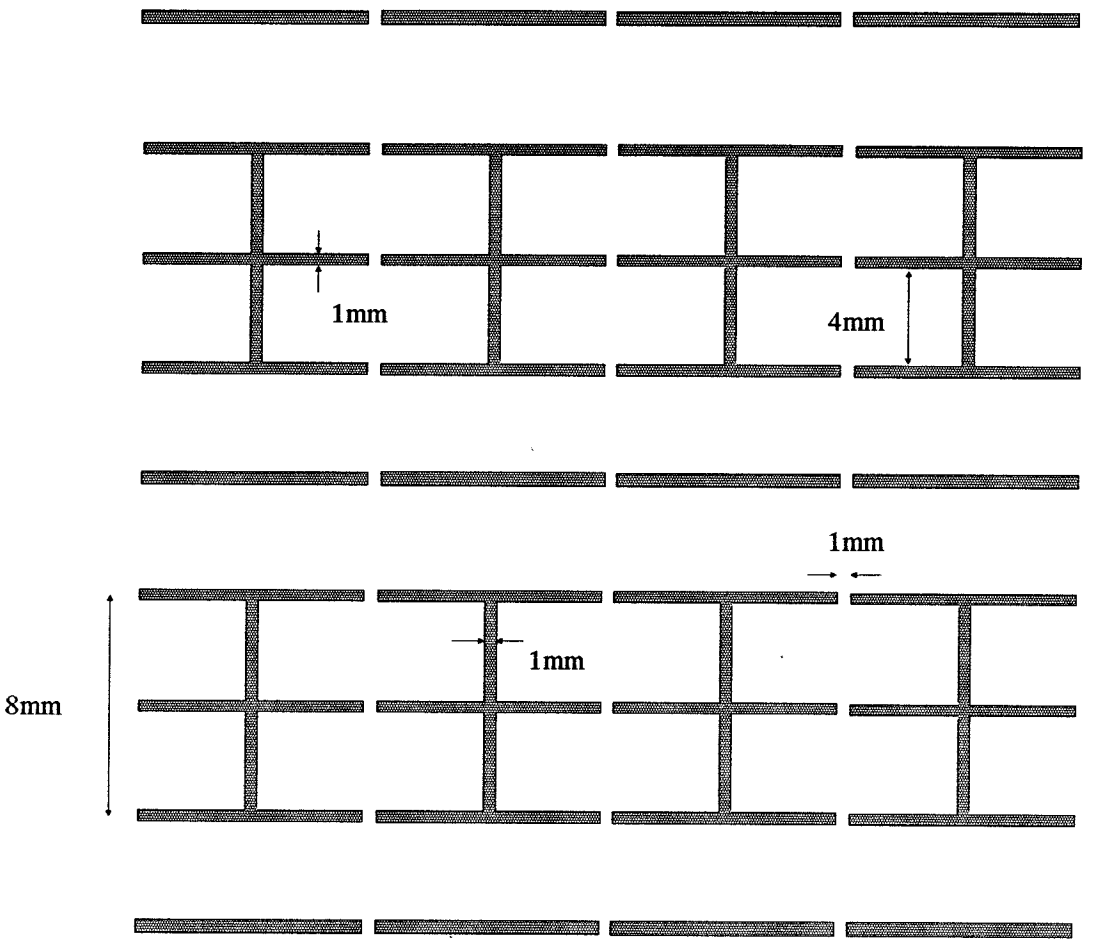

Figure 4.25 Schematic of a series-resonant grid with 1 mm gaps placed in the horizontal lines. The gaps are placed at the unit cell edges where a magnetic wall is assumed to exist. As a result, they are not expected to affect the grid embedding impedance.

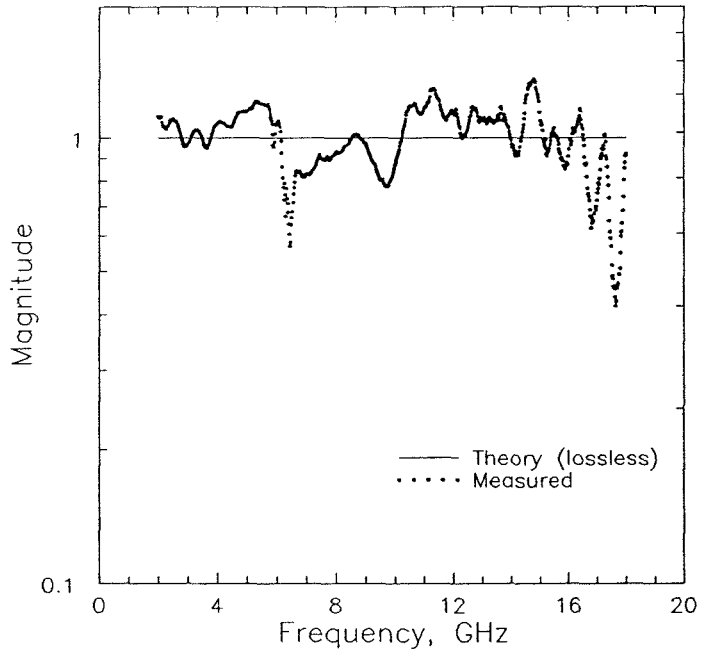

(a)

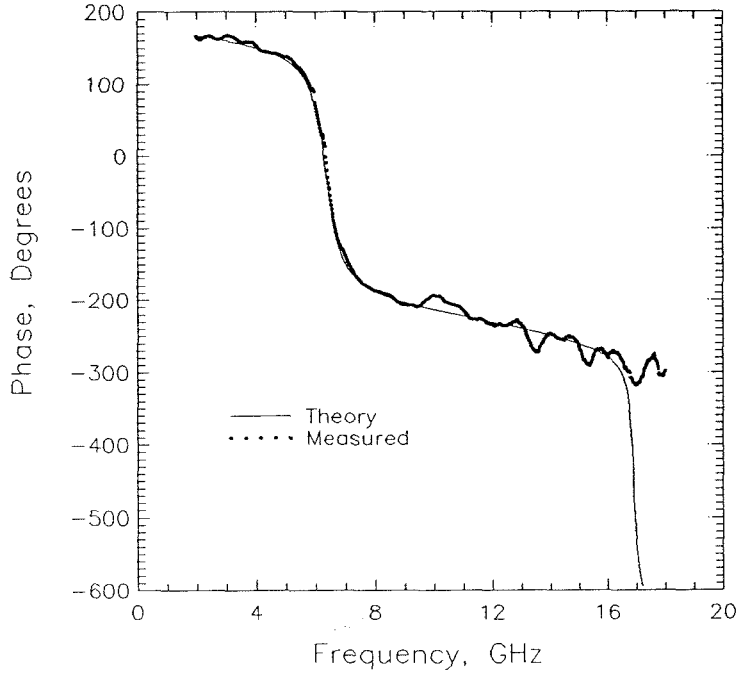

(b)

Figure 4.26 (a) Magnitude response of the series-resonant grid in Fig. 4.25. (b) Phase response of the series-resonant grid in Fig. 4.25.

References

[1] P.W. Hannan, M.A. Balfour, "Simulation of a Phased-Array Antenna in Waveguide," *IEEE Trans. Antennas Propag.,* AP-13, pp. 342–353, May 1965.

[2] A. Pance, M.J. Wengler, "Microwave Modeling of 2-D Active Antenna Arrays," *submitted to the IEEE Trans. Microwave Theory Tech.,* August 1991.

[3] G.F. Engen, "The Six-Port Reflectometer: An Alternative Network Analyzer," *IEEE Trans. Microwave Theory Tech.,* MTT-25, pp. 1075–1085, 1977.

[4] U. Stumper, "Six-Port and Four-Port Reflectometers for Complex Permittivity Measurements at Submillimeter Wavelengths," *IEEE Trans. Microwave Theory Tech.,* MTT-37, pp. 222–230, January 1989.

[5] R.A. Bohlander, A McSweeny, J.M. Newton, V.T. Brady, R.G. Shackelford, "A Quasi-Optical Scanning Multiport (QUOSM) Network Analyzer," 6^{th} *Int. Conf. on Infrared and Millimeter Waves,* F-2-5, Miami Beach, FL, 1981.

[6] W.W. Lam, C.F. Jou, H.Z. Chen, K.S. Stolt, N.C. Luhmann, Jr., D.B. Rutledge, "Millimeter-Wave Diode-Grid Phase Shifters," *IEEE Trans. Microwave Theory Tech.*, MTT-36, pp. 902–907, May 1988.

[7] A. Roberts, R.C. Compton, "A Vector Measurement Scheme for Testing Quasi-Optical Components," *Int. J. of Infrared and Millimeter Waves,* vol. 11, No. 2, pp. 165–174, 1990.

[8] S.J. Mason, "Feedback Theory – Some Properties of Signal Flow Graphs," *Proceedings of the IRE*, pp. 1144–1156, September 1953.

[9] G.F. Engen, "Calibrating the Six-Port Reflectometer by Means of Sliding Terminations," *IEEE Trans. Microwave Theory Tech.,* MTT-26, pp. 951–957, 1978.

[10] "*RT/Duroid* 6010," product specification sheet RT 8.6010, Rogers Corporation, Microwave Materials Division, 100 S. Roosevelt Ave., Chandler, AZ 85226, U.S.A.

[11] D.R. Gagnon, "Highly Sensitive Measurements with a Lens-Focussed Reflectometer," *IEEE MTT-S International Symposium Digest,* vol. 3, pp. 1017–1018, Boston, MA., 1991.

[12] "HP 85180A High-Frequency Structure Simulator," Hewlett-Packard Company, Networks Measurements Division, 1400 Fountaingrove Parkway, Santa Rosa, CA 95403, U.S.A.

[13] S. Ramo, J.R. Whinnery, T. Van Duzer, *Fields and Waves in Communication Electronics*, 2nd ed., John Wiley & Sons, New York, 1984, pp. 147–153.

[14] W.W. Lam, *Millimeter-Wave Monolithic Schottky Diode-Grid Phase Shifter*, Ph.D. Thesis, California Institute of Technology, pp. 20–22, 1987.

Chapter 5

Planar MESFET Oscillator Grids

A limitation in the development of millimeter and submillimeter-wave systems has been the lack of reliable and inexpensive high-power solid-state sources. Power combining has thus become a subject of much interest. Microwave power combining techniques based on resonant cavities and hybrids can be scaled for use in the millimeter and submillimeter-wave range [1], but waveguide wall losses become more severe at high frequencies and the smaller waveguide dimensions make circuit fabrication difficult. Quasi-optical power combining techniques avoid these problems because the signal propagation occurs in free space and the array of active devices can be many wavelengths across [2].

A variety of quasi-optical power-combining arrays have been investigated over the past few years [3–7]. Several of these involve arrays of microstrip radiators [4,5] which are coupled by either mutual or external injection-locking. In this chapter, we will discuss a different approach based on integrating active devices directly into periodic planar grids. The planar configuration is advantageous because it is compatible with monolithic fabrication techniques. In addition, we can represent the grid with a simple transmission-line circuit into which the device is readily included.

5.1 Grid Configurations

There are two important factors which determine the behavior of a quasi-optical array. The first is the choice of devices used in the grid. Gunn diodes

and IMPATT's are two-terminal devices and thus easily incorporated into a grid array. The low DC-to-RF efficiency, however, is a major drawback. In addition, Gunn diodes are inherently unstable and synchronization can prove difficult. Others have found it necessary to individually bias each device in the array to facilitate locking [4]. In contrast, transistors have a separate control terminal. This allows the devices in the grid to be more easily stabilized, thus permitting oscillation to be controlled through an appropriately designed feedback network.

The second major factor determining the behavior of a quasi-optical array is the grid's physical configuration. The grid structure, together with the optical resonator, provides an embedding circuit in which the solid-state devices are placed. The oscillation frequency, output power, and efficiency of the grid depend on the impedances this embedding circuit presents at the device terminals. A planar transistor grid configuration was discussed in section 3.3 and is shown again in Fig. 5.1. Transistors are placed at each node in the grid and are

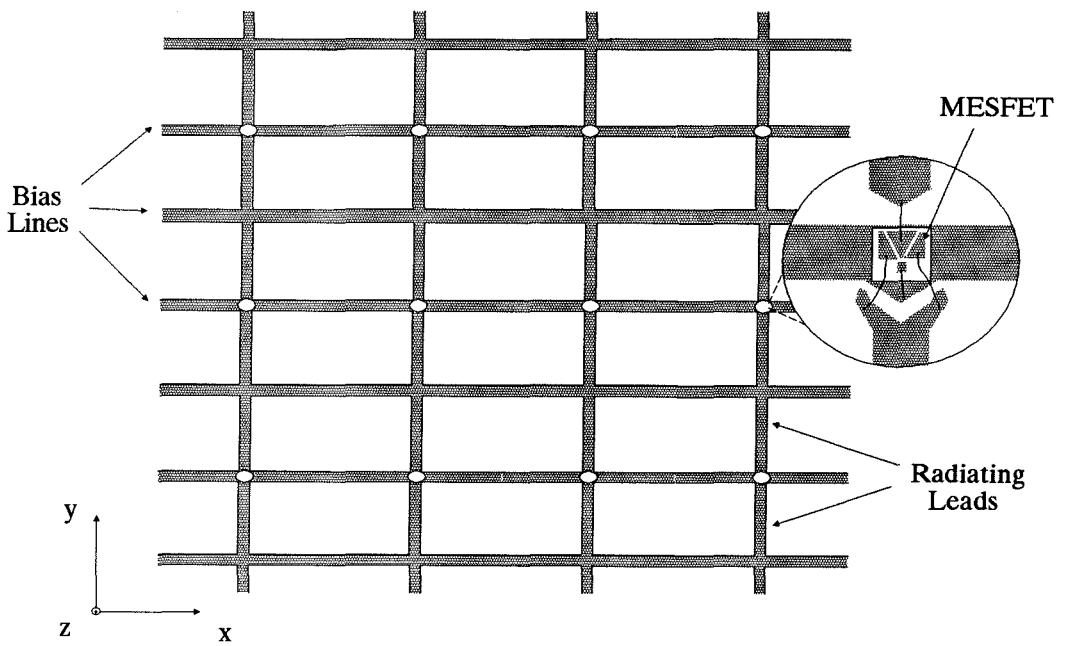

Figure 5.1 Schematic of the planar transistor grid. Bias lines run horizontally across the grid while the radiating leads run vertically as shown. Adjacent rows of devices share bias lines.

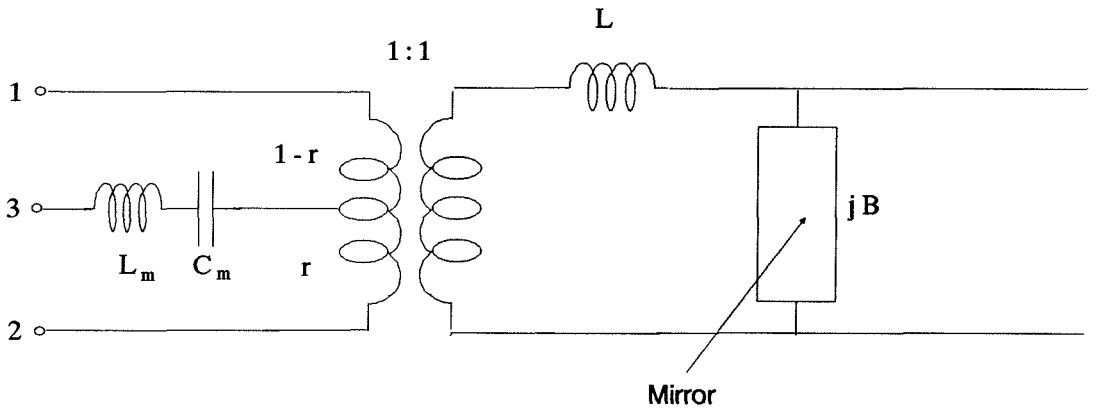

Figure 5.2 Transmission-line model for the planar transistor grid. Terminals 1 and 2 represent connections to the grid vertical leads while terminal 3 represents a connection to the horizontal lead. The transformer turns ratio r is defined as $r = c/b$.

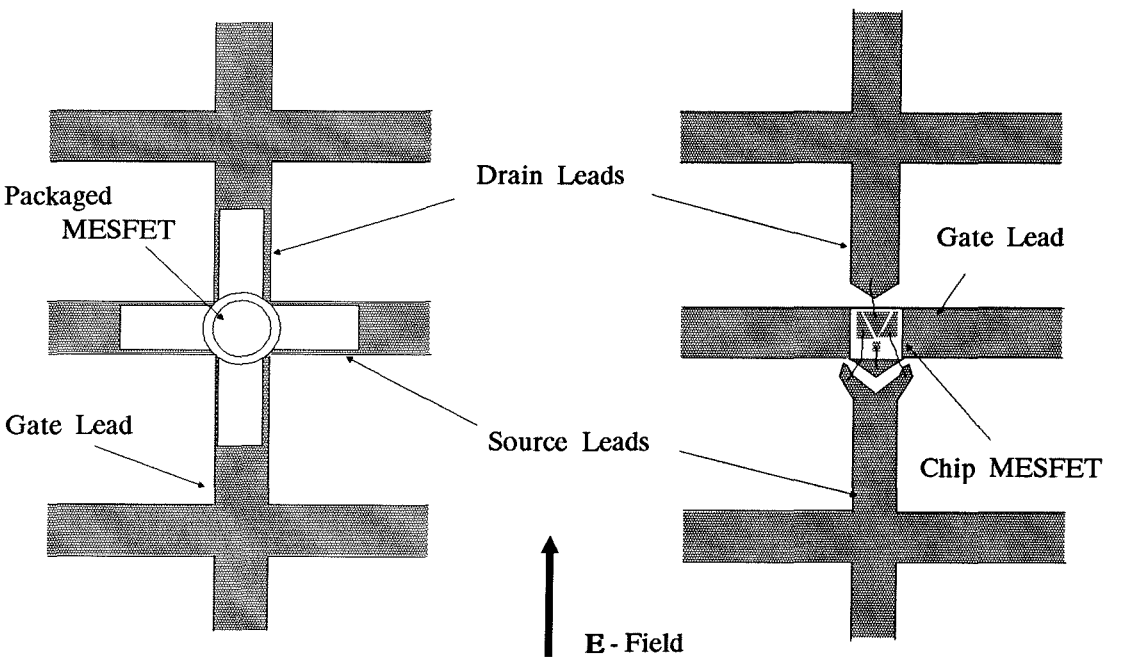

Figure 5.3 (a) Unit cell for a source-feedback grid oscillator which uses packaged MESFET's. The drain and gate leads are parallel to the incident electric field. (b) Unit cell configuration for a gate-feedback grid. A chip MESFET is wire bonded to the grid allowing the drain and source to couple to incident radiation.

represented by circles. The details of how the transistor is connected to the grid depends on the physical layout of the device and several options are possible. The DC bias is fed along horizontal leads which extend across the grid in the x-direction. Adjacent rows of devices share bias lines. The radiating leads run in the y-direction and are connected to two terminals of the transistor. The third transistor terminal is connected to the center bias line which runs along the row of devices.

In chapter 3, we derived an equivalent circuit model for the planar transistor grid. This model is shown in Fig. 5.2. In addition to the dimensions of the unit cell and the substrate thickness and dielectric constant, we are free to vary the orientation of the device in the grid. Two examples are shown in Fig. 5.3. With a "vertical drain-gate" or "source-feedback" grid, an incident electric field couples to the MESFET drain and gate leads. As a result, the source lead does not radiate. It does, however, couple indirectly to the radiated field through the grid embedding circuit. Due to the device layout, the source-feedback grid is a natural configuration for packaged microwave transistors like *Fujitsu's* FSC11LF. Using chip devices, as shown in Fig. 5.3(b), a "vertical drain-source" or "gate-feedback" configuration is possible. A gate-feedback grid allows the drain and source currents to radiate. In the following sections, experimental results for source-feedback and gate-feedback grids are discussed in detail.

5.2 Source-Feedback MESFET Grids

Figure 5.4 shows a photograph of a 100-element source-feedback oscillator grid [8]. Packaged MESFET's (*Fujitsu* FSC11LF) are soldered to the grid which is fabricated on a *Duroid* substrate with $\epsilon_r = 2.2$. This substrate, which is 0.5 mm thick, is mounted on a second substrate 2.5 mm thick with dielectric constant of 10.5. The design of the grid was determined by the size and layout of the device packages. A source-feedback configuration is necessary because of the package layout. Devices in the grid are spaced 8 mm apart in both the x and y-directions

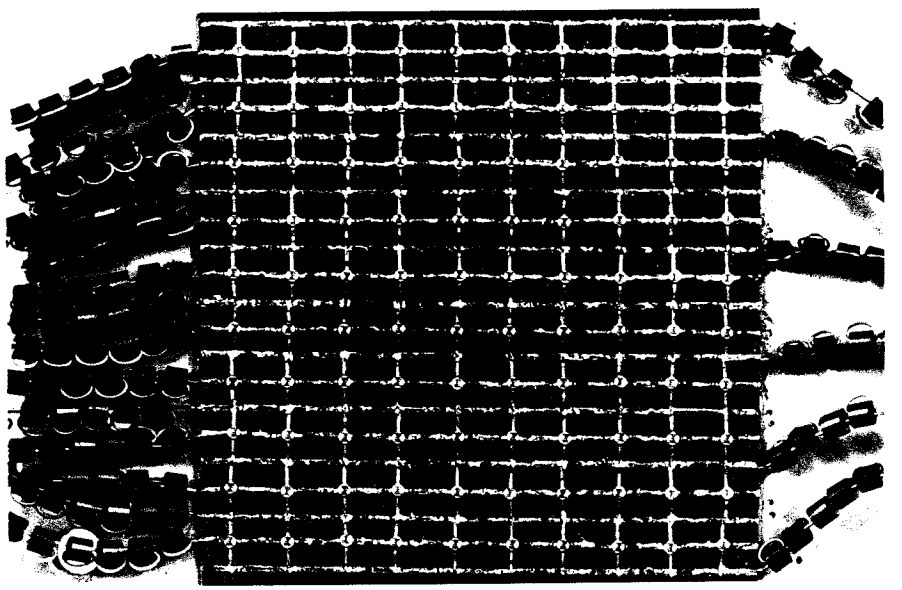

Figure 5.4 Photograph of the 100-element source-feedback MESFET grid. Horizontal metal lines are used for bias and the vertical leads radiate. The devices are FSC11LF packaged MESFET's manufactured by *Fujitsu*. Ferrite beads are added to the bias lines to suppress low-frequency oscillations.

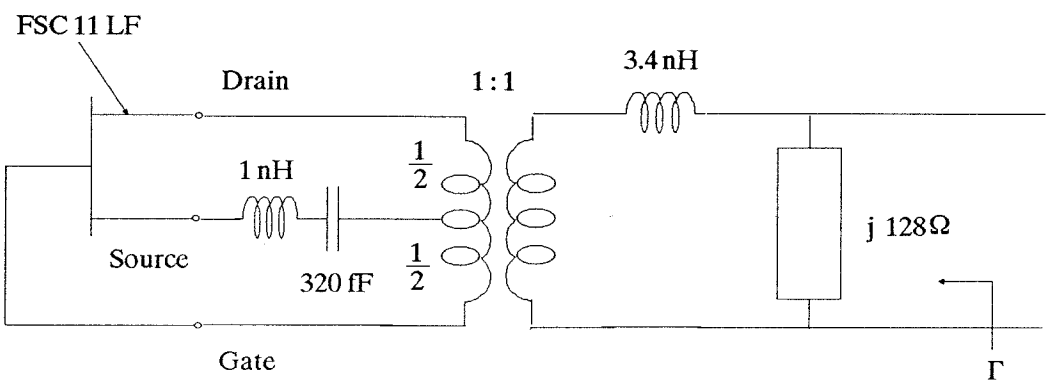

Figure 5.5 Equivalent circuit model for the source-feedback MESFET grid of Fig. 5.4. The values for the lumped elements are specified for 5 GHz. The grid reflection coefficient is given by Γ.

due to the length of the package leads.

By adding the MESFET to the transmission-line model for the grid, we obtain the circuit shown in Fig. 5.5. Equations (3.30)–(3.33) are used to calculate values for the lumped elements in the model. We can predict the oscillation frequency of the grid by computing the reflection coefficient the grid presents to an incident plane wave. This approach is different from traditional oscillator design methods in that the circuit is analyzed from an external port rather than internally. For oscillation to occur, the grid reflection coefficient, Γ, must satisfy the relation:

$$\Gamma = \frac{1}{s_l} \tag{5.1}$$

where s_l is the load reflection coefficient. For oscillation into a matched load, the grid reflection coefficient must become infinite. This can be realized if the grid reflection coefficient traces out a counterclockwise loop in the complex plane as shown in Fig. 5.6. As the oscillation in the resonator grows, the MESFET gain decreases until the roundtrip gain balances the roundtrip loss. Measurements done by Johnson [9] suggest that transistor saturation can be simulated by decreasing $|s_{21}|$ of the MESFET. The effect of decreasing $|s_{21}|$, also shown in Fig. 5.6, is that the counterclockwise loop expands until the oscillation condition ($\Gamma = \infty$) is met.

The oscillation frequency of the grid also depends on reactive tuning provided by the Fabry-Perot cavity. A mirror is placed behind the grid to synchronize the devices and its position influences the oscillation frequency. Frequency tuning versus mirror position as predicted by the transmission-line model is shown in Fig. 5.7 and is in good agreement with measurement. The theoretical curve is obtained by finding the frequency corresponding to the maximum value of the reflection coefficient for each mirror position. The tuning range is about 10% at 5 GHz. From the far-field radiation pattern, the directivity is measured to be 16 dB. This gives a maximum radiated power of 600 mW and corresponds to

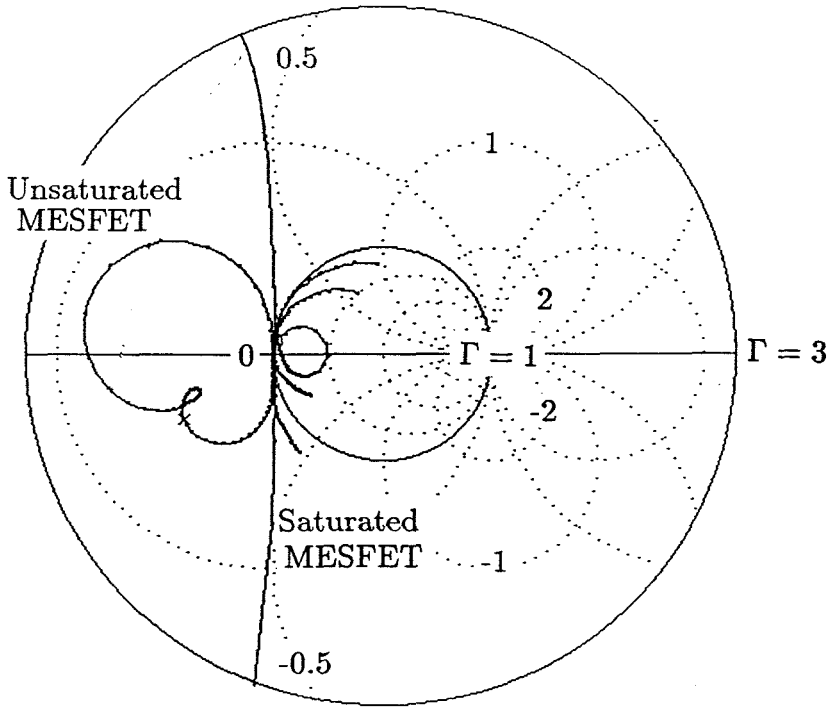

Figure 5.6 Smith chart plot of the source-feedback grid reflection coefficient. The MESFET is modeled using its small-signal s-parameters. Transistor saturation is simulated by decreasing the magnitude of s_{21} until the counterclockwise loop sweeps out to infinity.

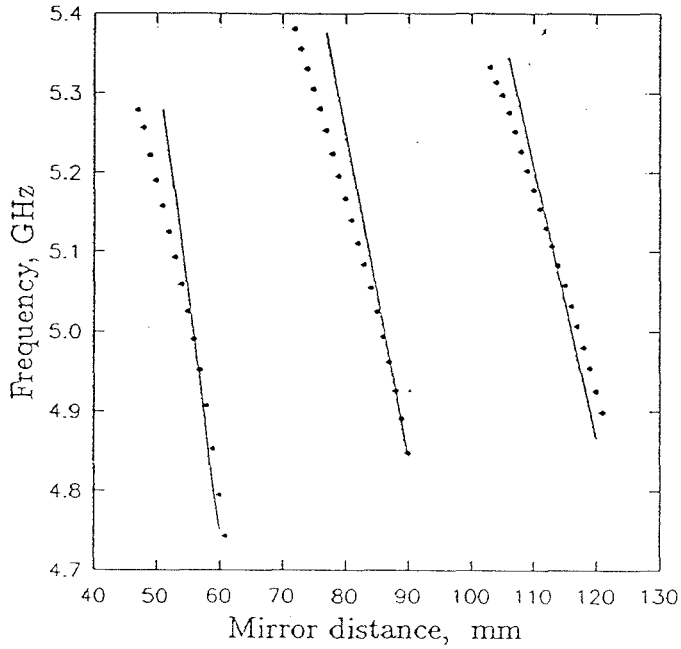

Figure 5.7 Measured and predicted frequency tuning curves for the source-feedback oscillator grid.

a DC-to-RF conversion efficiency of 20%. Details of the measurements and other results pertaining to external injection locking are discussed in reference [8].

5.3 Gate-Feedback MESFET Grids

A disadvantage of the source-feedback oscillator grid is the MESFET gate lead is parallel to the radiated electric field. Because the gate and radiated field are strongly coupled, the grid tends to oscillate at lower frequencies where the MESFET has high gain. A variety of simulations were performed using the grid transmission-line model and the FSC11LF in the source-feedback configuration. In these studies, the 5 GHz oscillation could not be suppressed, suggesting that a different configuration be investigated to increase the grid operating frequency.

The gate-feedback configuration shown in Fig. 5.3(b) permits the drain and source leads of the MESFET to radiate. Because the gate leads are perpendicular to the electric field, they now couple to incident plane waves through the reactive elements in the grid model. Consequently, the signal fed back to the MESFET gate is strongly dependent on frequency. This makes it possible for an appropriately designed gate-feedback grid to meet the conditions necessary for oscillation at higher frequencies. To demonstrate the feasibility of high-frequency oscillations with the gate-feedback configuration, a number of grid designs using FSC11X chip MESFET's were studied.

5.3.1 Grid Design

An alternative method for designing oscillator grids is based on calculating the loop gain for the MESFET grid circuit model. This technique, which is essentially an application of Nyquist's criterion for finding instabilities in a system, has been used to design several gate-feedback grids. To determine the system loop gain, it is necessary to use the lumped element circuit model for the MESFET. Figure 5.8 shows the small-signal circuit model and chip layout for the FSC11X. Values for the lumped elements, which are dependent on DC bias,

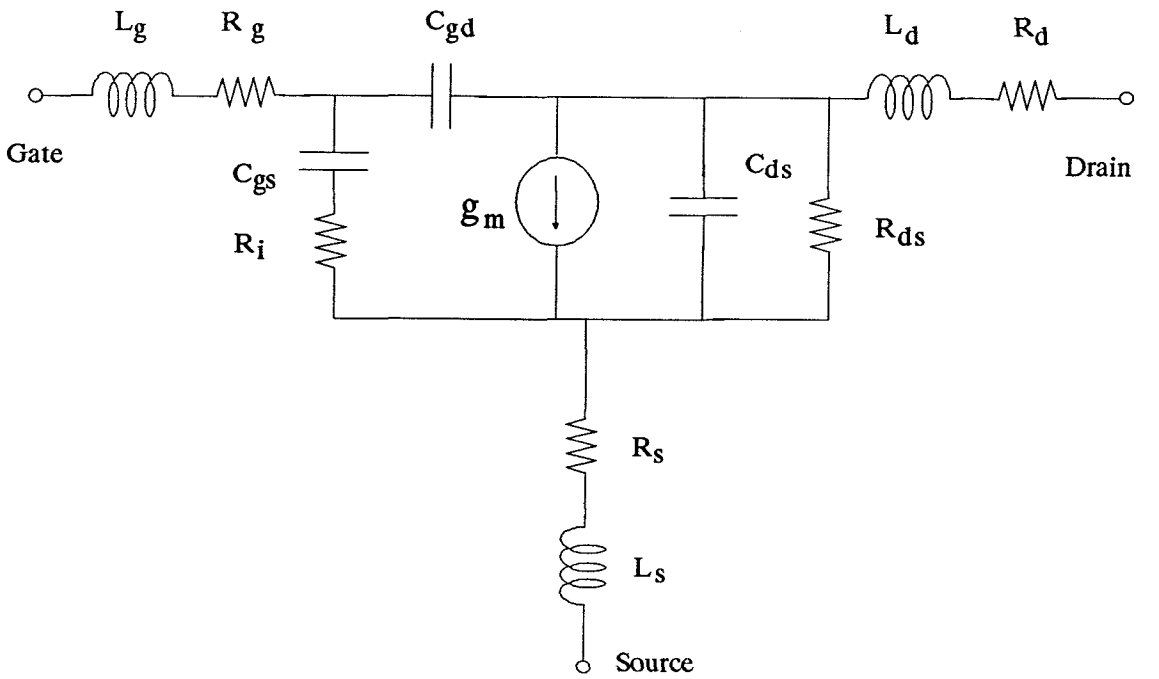

(a)

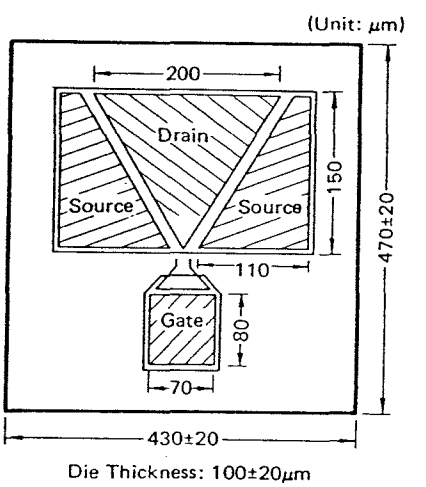

(b)

Figure 5.8 (a) Lumped element circuit model for the *Fujitsu* FSC11X. The values for the circuit elements are obtained from the manufacturer's data sheet. (b) Chip layout for the FSC11X [10].

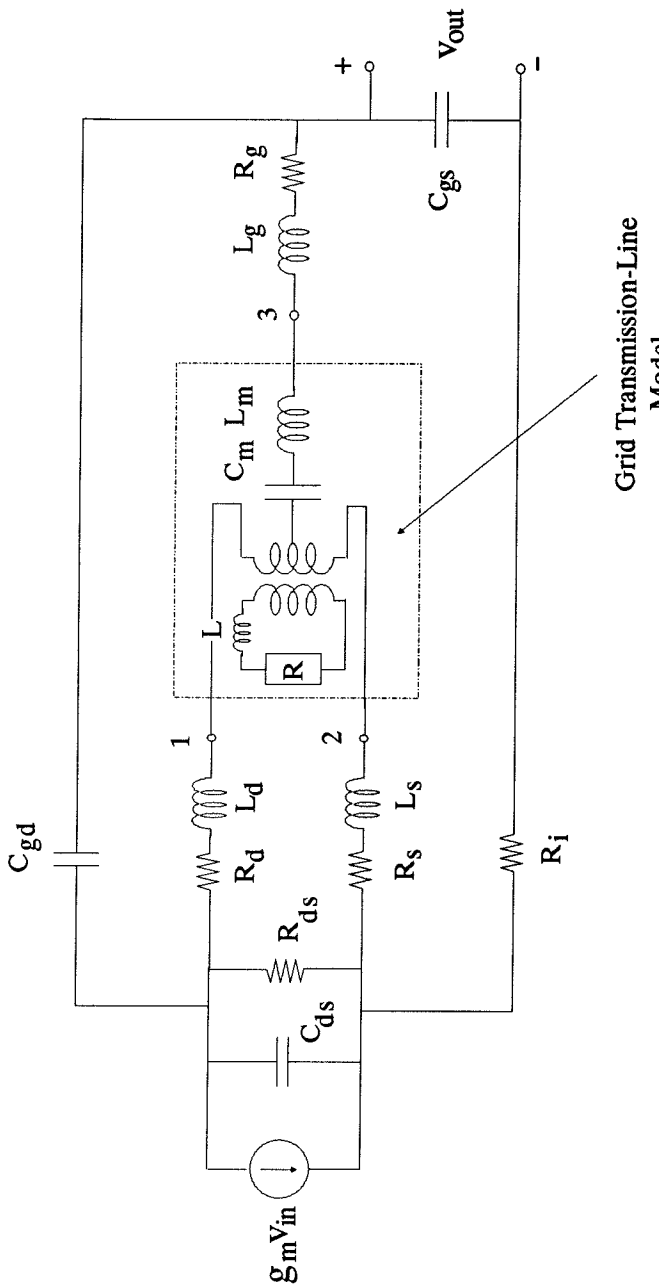

Figure 5.9 Circuit used to calculate the loop gain of the gate-feedback oscillator grid. The voltage across the gate-source capacitor controls the transconductance current. The grid tranmission-line model provides a path between the drain-source port and the gate terminal. A lumped element, R, represents the TEM mode produced by the drain and source currents.

are given in Table 5.1. The transconductance current is controlled by the voltage appearing across the gate-source capacitor, C_{gs}. Adding the MESFET to the grid transmission-line model gives us the gate-feedback circuit shown in Fig. 5.9. The grid transmission-line model provides a path between the drain-source port of the MESFET and the gate, hence the terminology "gate-feedback."

The system loop gain is calculated by assuming the MESFET current source excites the circuit with a current $I = g_m v_{in}$. This excitation results in a voltage across the gate-source capacitor, v_{out}. Loop gain is given by v_{out}/v_{in}. Because v_{out} controls the current source, a loop gain with magnitude greater than unity and zero phase shift indicates instability and, as a result, oscillation. By adjusting the dimensions of the grid and choosing an appropriate dielectric substrate, the circuit of Fig. 5.9 can be used to design a grid that will oscillate at a particular frequency.

I_{DS} (mA)	10	30
g_{m0} (mS)	40	65
τ (psec)	2.5	2.5
C_{gs} (pF)	0.38	0.54
C_{gd} (pF)	0.059	0.044
C_{ds} (pF)	0.12	0.12
R_i (Ω)	4.0	5.5
R_{ds} (Ω)	220	180
R_g (Ω)	2.0	2.0
R_s (Ω)	2.2	1.5
R_d (Ω)	2.2	1.5
L_g (nH)	0.2	0.2
L_s (nH)	0.055	0.055
L_d (nH)	0.2	0.2

Table 5.1 Component values for the lumped elements in the FSC11X MESFET model of Fig. 5.8. The transconductance has an associated transit time delay, τ, such that $g_m = g_{m0}e^{-j\omega\tau}$. The parameters are specified for a drain voltage of 3 V.

Thus far, we have discussed two techniques for oscillator grid analysis: a counterclockwise loop method based on examining the grid from an external port, and a loop gain method in which the circuit is examined internally. Both can be used to design grid oscillators. Which method to choose depends on the particular situation. If a device model is not available, then the counterclockwise loop method can be applied using the device's small-signal s-parameters. A drawback to this technique, however, is that some instabilities may not be found by looking for counterclockwise loops. In addition, it may be difficult to determine an exact frequency of oscillation because the MESFET s-parameters may experience phase shifts as the device gain saturates. If the device circuit model is known, then the loop gain method is readily applied. An oscillation frequency is easily determined from the loop gain by finding the zero-phase crossing. In addition, a polar plot of the loop gain clearly shows if the oscillation condition is met.

5.3.2 X-Band MESFET Grid

A gate-feedback grid oscillator, designed using the circuit of Fig. 5.9, is shown in Fig. 5.10. The grid contains 16 MESFET chips (*Fujitsu* FSC11X) spaced 9 mm apart in both the x and y-directions. The substrate is 2.5 mm thick *Duroid* with a dielectric constant of 2.2. Copper lines etched on the substrate surface are 1 mm wide. The MESFET chips are soldered to the horizontal (gate) leads and connected to the grid using 1 mil diameter gold bond wire. From these dimensions, the radiating lead inductance, L, is calculated to be 3.4 nH at 5 GHz. L_m and C_m are 0.94 nH and 304 fF at 5 GHz, respectively. Because the reactive components in the grid model are dispersive, these values are specified at a particular frequency. To preserve the symmetries assumed in the grid model, the vertical leads extend a quarter wavelength above and below the top and bottom rows. In choosing the lengths of these quarter-wave stubs, we use the mean dielectric constant for the substrate and free space. Bond wires are used to bring the DC bias in from the sides.

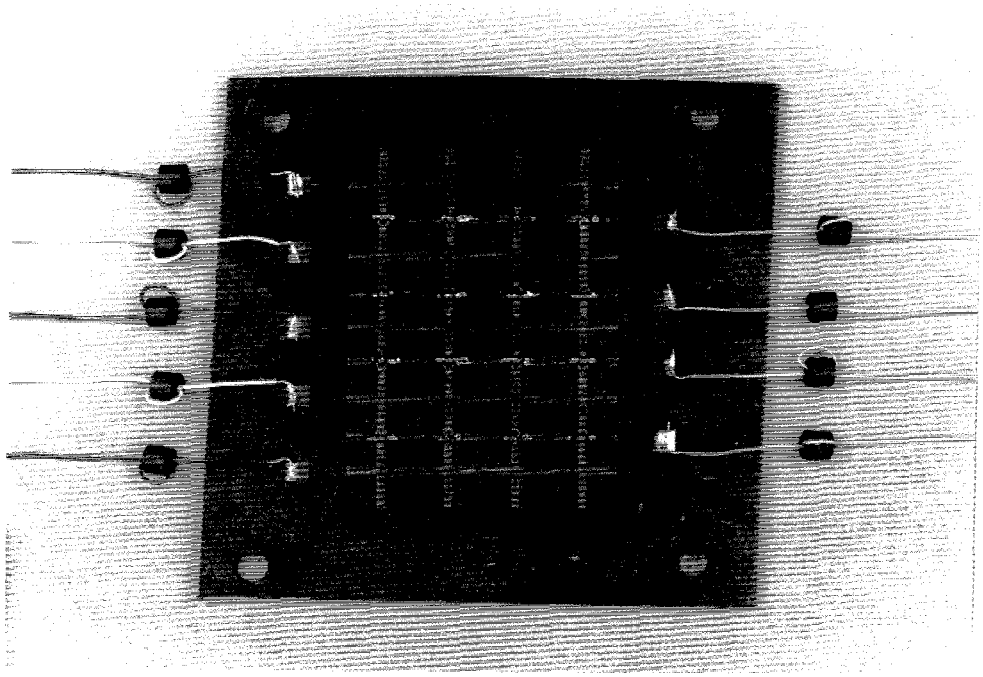

(a)

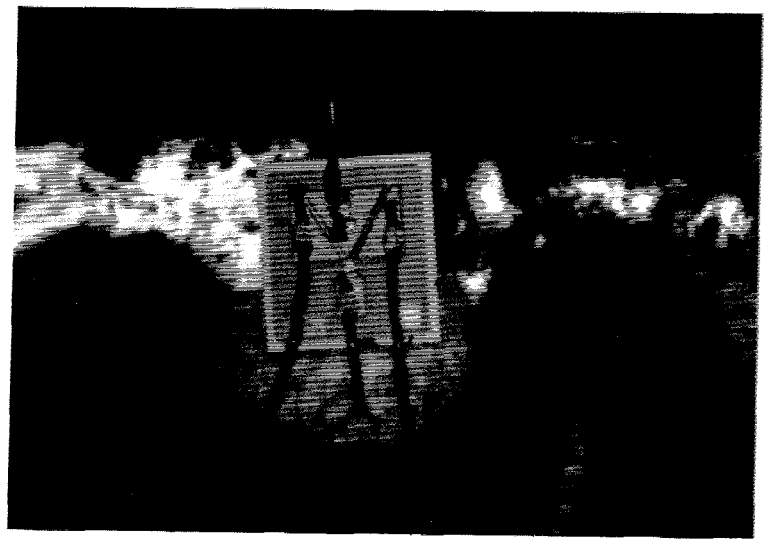

(b)

Figure 5.10 (a) Photograph of the X-band grid oscillator. The substrate is 2.5 mm thick *Duroid* with $\epsilon_r = 2.2$. The grid is placed between a mirror and dielectric slab which form the Fabry-Perot cavity. Ferrite beads in the bias lines suppress low-frequency oscillations. (b) Photograph of a FSC11X chip in the unit cell.

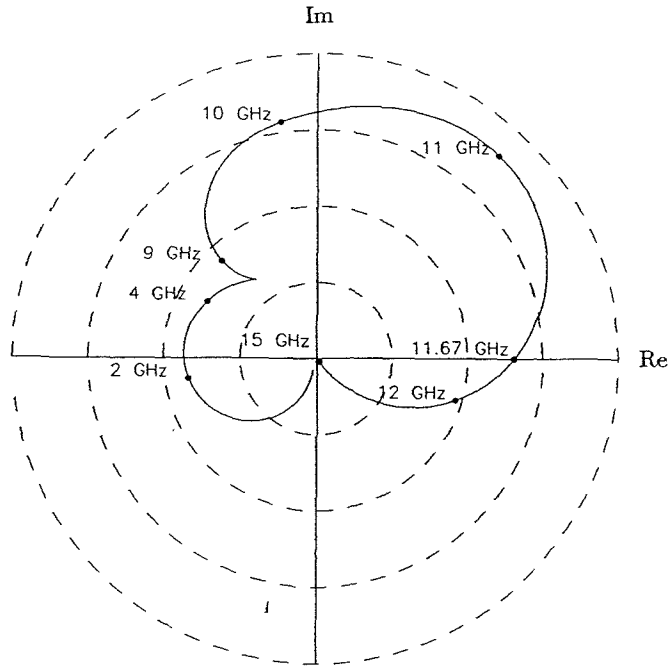

Figure 5.11 Calculated loop gain of the X-band MESFET grid as frequency is swept from DC to 15 GHz. The locus crosses the zero-phase point at 11.67 GHz indicating oscillation at that frequency.

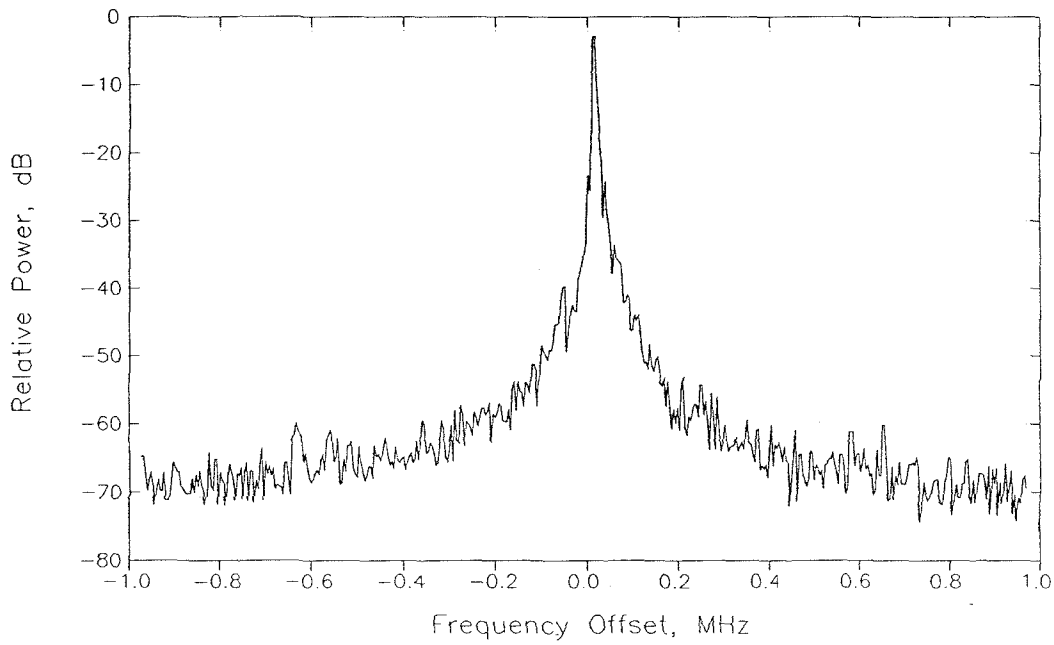

Figure 5.12 Spectrum of the X-band MESFET grid. The center frequency is 11.58 GHz and the resolution bandwidth is 10 kHz.

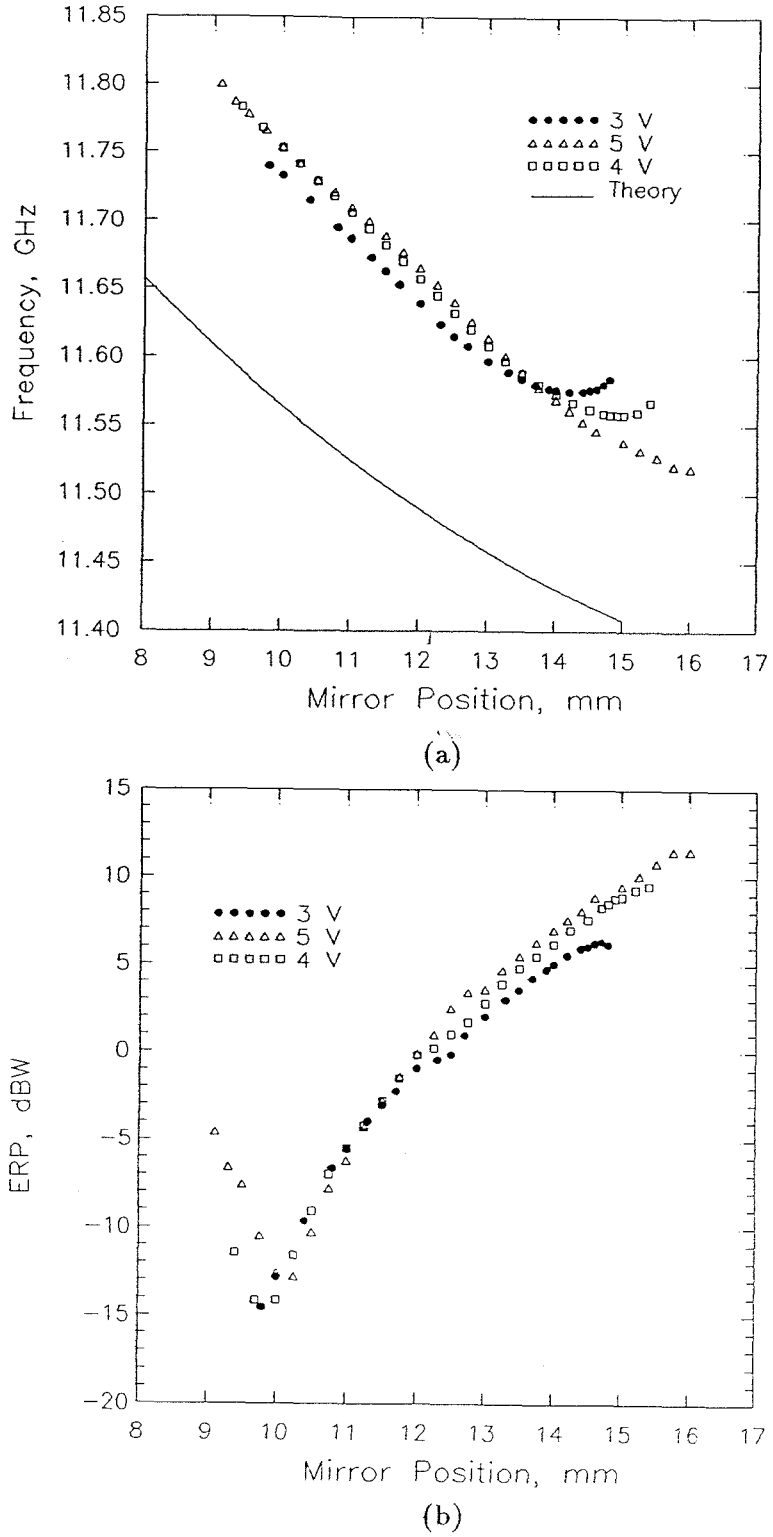

Figure 5.13 (a) Oscillation frequency and (b) effective radiated power of the grid as a function of mirror position for various drain bias voltages. For these measurements a dielectric slab was placed 2 cm in front of the grid and the gate was biased at −1.4 V.

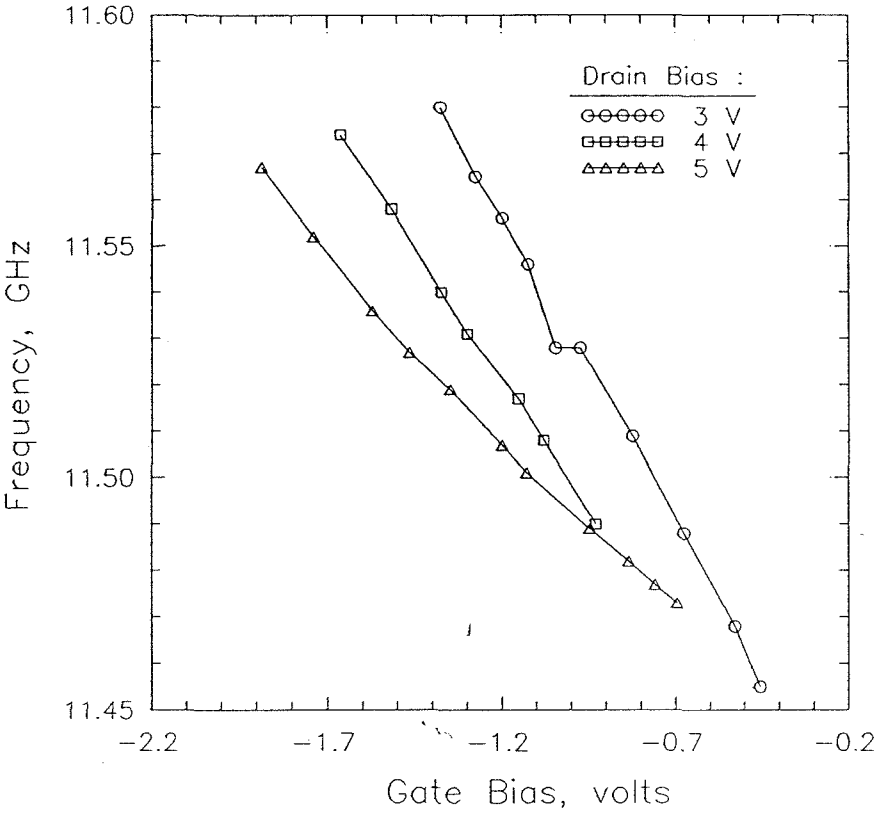

Figure 5.14 Measured frequency tuning with gate bias. The mirror was positioned 14 mm behind the grid with the dielectric slab 2 cm in front.

A polar plot of the loop gain, v_{out}/v_{in}, for the grid is shown in Fig. 5.11. The loop gain has a magnitude of 2.7 and zero phase at 11.67 GHz, indicating an oscillation at that frequency. Fig. 5.12 shows the measured spectrum when the grid is biased with a drain voltage of 3 V and total current of 200 mA. The maximum effective radiated power (ERP) of the grid is 15 W. For this measurement, a planar mirror is placed 14 mm behind the grid and a dielectric tuning slab is placed 2 cm in front of the grid. The dielectric slab (1.25 mm thick with $\epsilon_r = 10.2$) was found to be helpful in locking the grid to a single frequency, but not necessary. The mirror and dielectric slab can be used to tune the frequency and power of the oscillation. These tuning curves are shown in Fig. 5.13 for three different bias points. A theoretical frequency tuning curve obtained from the equivalent circuit model is shown for comparison and is within 2% of the

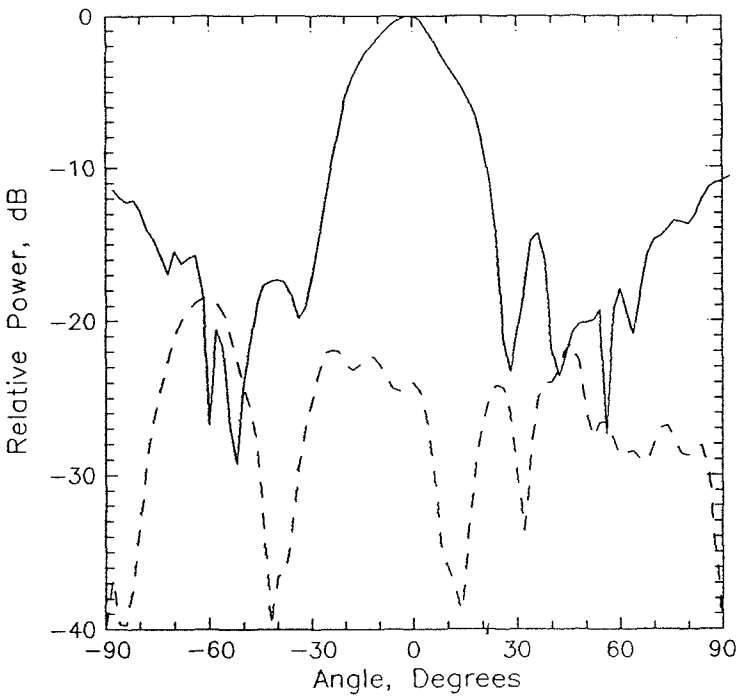

(a)

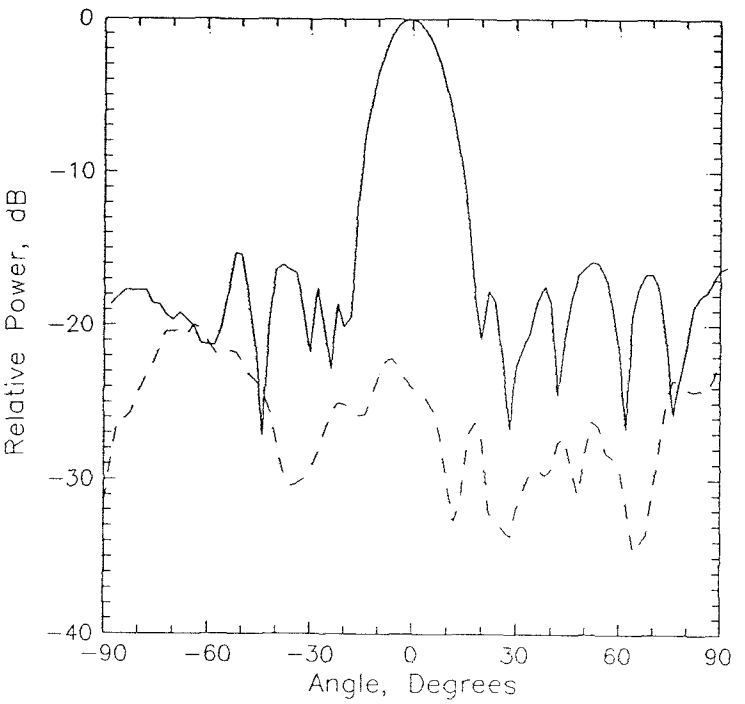

(b)

Figure 5.15 Measured far-field radiation patterns for the X-band grid in the (a) H-plane and (b) E-plane. The cross-polarized patterns are shown with dashed lines.

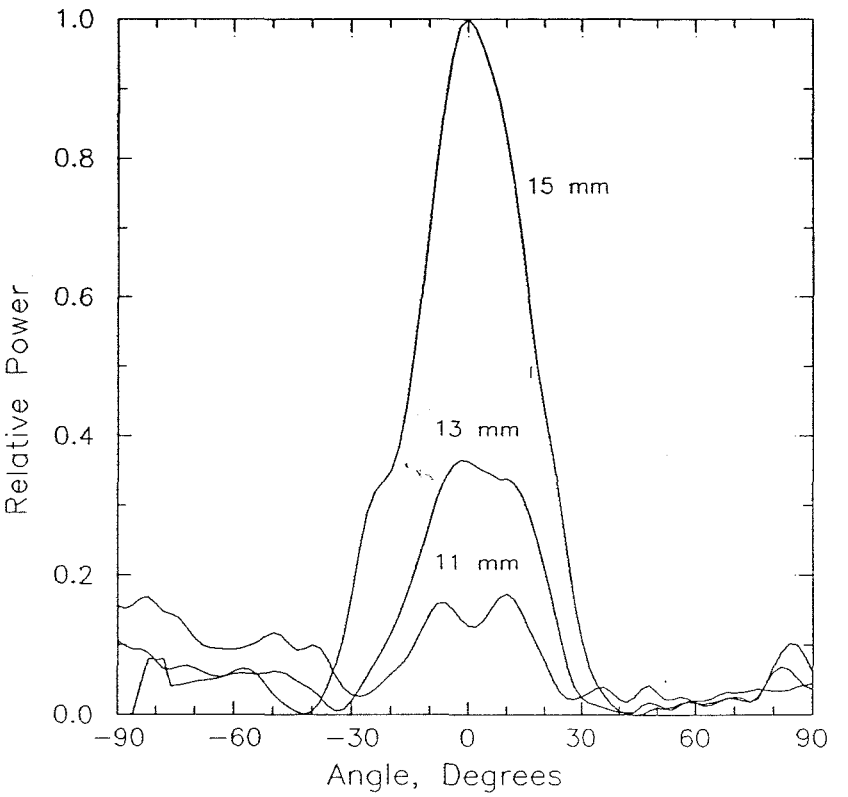

Figure 5.16 Far-field H-plane pattern of the X-band grid as a function of mirror position. As the mirror is moved towards the grid, directivity and radiated power decrease.

measured curve. Gate bias voltage can also be used to tune the frequency but has little effect on the output power (Fig. 5.14). The far-field radiation pattern measured with a standard-gain pyramidal horn at a distance of 160 cm gives a maximum directivity of 16.5 dB (Fig. 5.15). The antenna pattern is also a strong function of mirror position as shown in Fig. 5.16. Maximum power radiated from the grid is measured to be 335 mW, or 20 mW per device. This corresponds to peak directivity and gives a DC-to-RF conversion efficiency of 20%.

5.3.3 Ku-Band MESFET Grid

One advantage of planar transistor grids is that they can be scaled for operation at higher frequencies. Simulations with the grid equivalent circuit model indicate that oscillation near the f_T of the transistor is quite reasonable to obtain. To investigate the practicality of scaling grids and as a further check on the grid transmission-line model, a Ku-band grid was designed, built and tested. The Ku-band design uses the same devices as the X-band oscillator (FSC11X MESFET's) and is connected in a gate-feedback configuration. A 36-element grid fabricated on *Duroid*, 2.5 mm thick with $\epsilon_r = 2.2$, is shown in Fig. 5.17. The unit cell is square and the devices are spaced 5 mm apart. The leads are 0.5 mm wide and, as with the X-band grid, extended a quarter wavelength above the top row and below the bottom row of the grid.

Simulations performed with the equivalent circuit model indicated the grid would oscillate at 17 GHz . A polar plot of the system loop gain is shown in Fig. 5.18. Single frequency operation of the Ku-band grid was verified with a spectrum analyzer. Again, power and frequency can be tuned using the mirror (Fig. 5.19). The grid produces an effective radiated power (ERP) of 3.3 W, corresponding to a total radiated power of 235 mW. This is equivalent to 6.5 mW per device and gives a DC-to-RF conversion efficiency of 7%. Measurement of the grid radiation pattern, shown in Fig 5.20, gives a directivity of 11.5 dB.

The observed reduction in output power and efficiency compared to the X-band grid is expected due to the higher operating frequency. Evans has given an expression for the maximum efficiency that can be obtained from a transistor oscillator [11] :

$$\eta = \frac{1}{2}\left\{1 - \frac{1}{G_0} - \frac{\ln(G_0)}{G_0}\right\} \times 100\%, \tag{5.2}$$

where G_0 is the small-signal maximum available gain of the device and is given by $G_0 = (f_{max}/f)^2$. Equation (5.2) assumes the transistor circuit operates in class A and that the power saturation characteristic of the device can be represented with

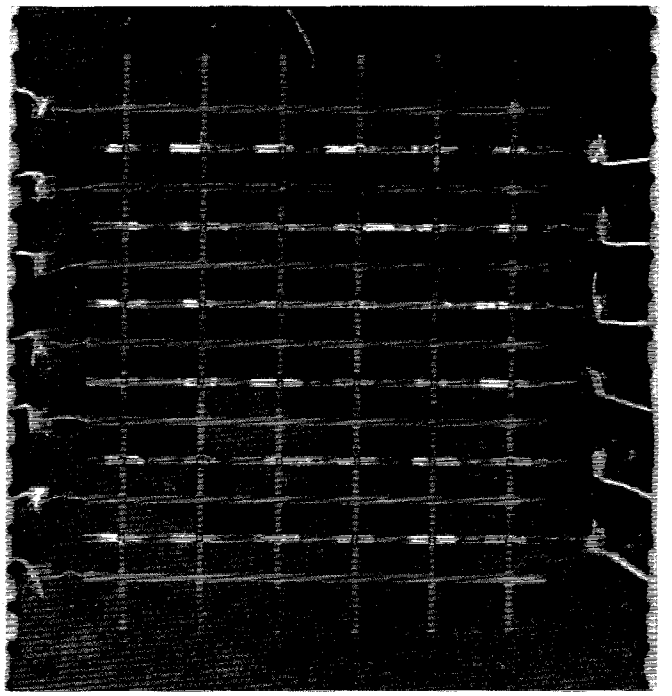

Figure 5.17 Photograph of the Ku-band MESFET oscillator grid. The devices are *Fujitsu* FSC11X MESFET chips.

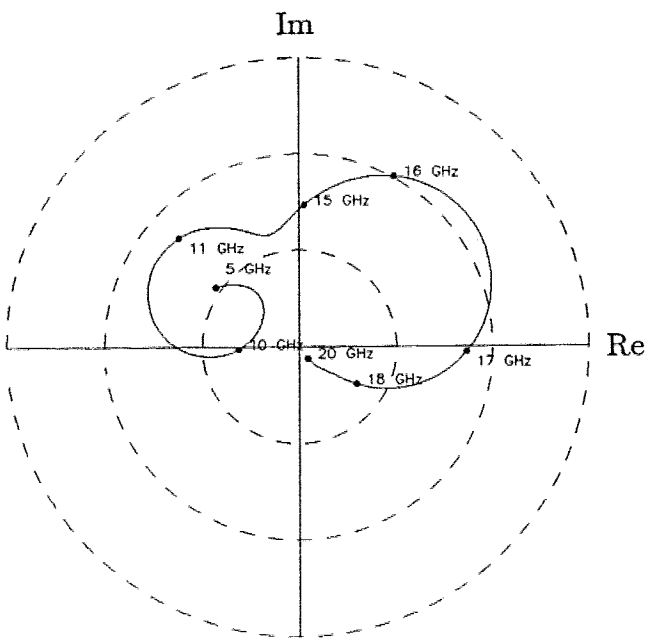

Figure 5.18 Loop gain of the Ku-band MESFET oscillator grid. The frequency is swept from 5 to 20 GHz. The locus crosses the zero-phase point at 17 GHz. indicating oscillation at that frequency.

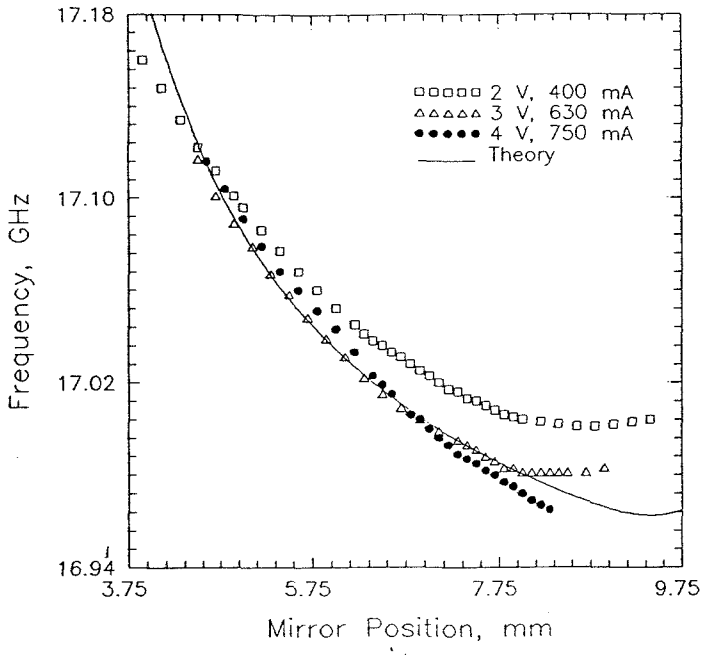

(a)

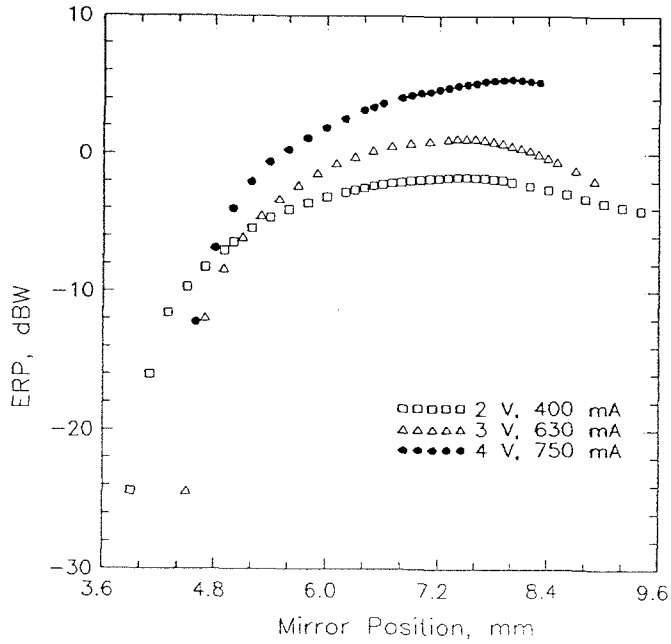

(b)

Figure 5.19 (a) Frequency and (b) ERP tuning curves for the Ku-band MESFET grid at three different bias points. These measurements were taken without a front dielectric reflector.

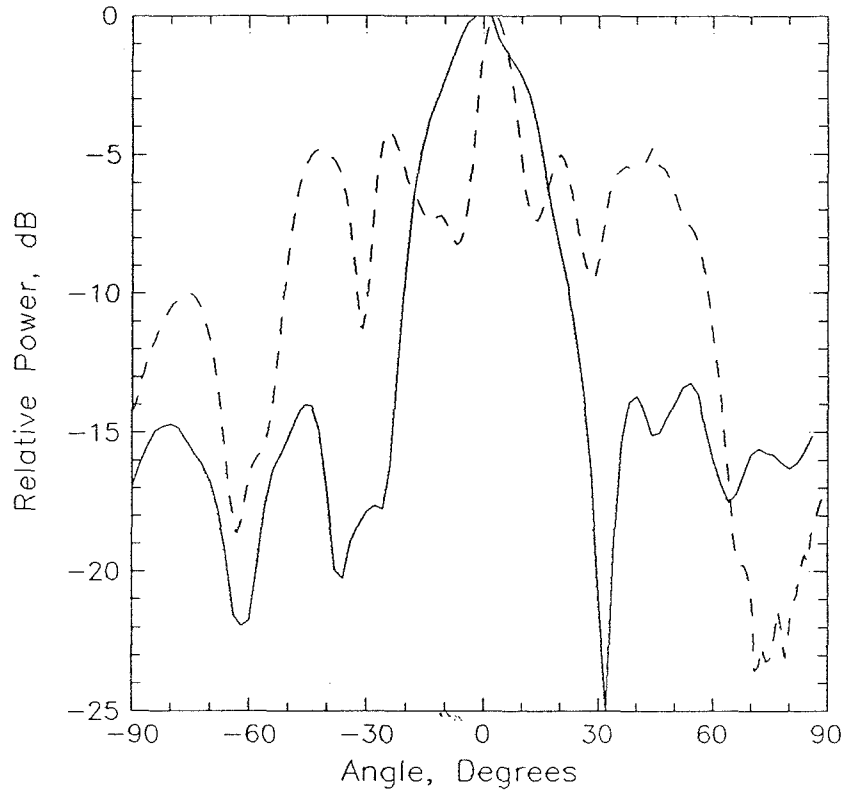

Figure 5.20 Measured far-field radiation pattern for Ku-band grid on the (—) H-plane and (– – –) E-plane.

an exponential formula [9]. The f_{max} of the FSC11X is approximately 33 GHz. From equation (5.2) we can expect a maximum DC-to-RF conversion efficiency of 30% at 11.5 GHz and 19% at 17 GHz. Clearly, by optimizing the design, it should be possible to improve the efficiency and power output of the gate-feedback grids

References

[1] K. Chang, C. Sun, "Millimeter-Wave Power Combining Techniques," *IEEE Trans. Microwave Theory Tech.,* MTT-31, pp. 91–107, February 1983.

[2] J. W. Mink, "Quasi-Optical Power Combining of Solid-State Millimeter-Wave Sources," *IEEE Trans. Microwave Theory Tech.*, MTT-34, pp. 273–279, February 1986.

[3] L. Wandinger, V. Nalbandian, "Millimeter-Wave Power Combiner Using Quasi Optical Techniques," *IEEE Trans. Microwave Theory Tech.,* MTT-31, pp. 189–193, February 1983.

[4] R.A. York, R.C. Compton, "Quasi-Optical Power-Combining Using Mutually Synchronized Oscillator Arrays," *IEEE Trans. Microwave Theory Tech.,* MTT-39, pp. 1000–1009, June 1991.

[5] J. Birkeland, T. Itoh, "A 16-Element Quasi-Optical FET Oscillator Power-Combining Array with External Injection Locking," *submitted to the IEEE Trans. Microwave Theory Tech.,* June 1991.

[6] Z.B. Popović, R.M. Weikle, II, M. Kim, K.A. Potter, D.B. Rutledge, "Bar-Grid Oscillators," *IEEE Trans. Microwave Theory Tech.,* MTT-38, pp. 225–230, March 1990.

[7] M. Nakayama, M. Heida, T. Tanaka, K. Mizuno, "Millimeter and Submillimeter Wave Quasi-Optical Oscillator with Multi-Elements," *1990 IEEE MTT-S International Symposium Digest,* vol. 3, pp. 1209–1212, Dallas, TX.

[8] Z.B. Popović, R.M. Weikle, II, M. Kim, D.B. Rutledge, "A 100-MESFET Planar Grid Oscillator," *IEEE Trans. Microwave Theory and Tech.*, MTT-39, pp. 193–200, February 1991.

[9] K.M. Johnson, "Large Signal GaAs MESFET Oscillator Design," *IEEE Trans. Microwave Theory Tech.,* MTT-27, pp. 217–227, March 1979.

[10] "Fujitsu Microwave Semiconductor Data Book," Fujitsu Microelectronics, Inc., Microwave and Optoelectronics Division, 3330 Scott Blvd., Santa Clara, CA 95054-3101, U.S.A.

[11] D.H. Evans, "High-Efficiency Ka- and Ku-Band MESFET Oscillators," *Electronics Lett.*, vol. 21, no. 6, pp. 254-255, 1985.

Chapter 6

Discussion and Suggestions for Future Work

In this work, we have examined several different planar grid structures that are suitable for solid-state device integration. Two of these grids, the rectangular slot array and the bow-tie array, can be used with two-terminal devices. A third configuration consisting of an array of vertical and horizontal strips is amenable to three-terminal devices. We also found that these grids could be represented with simple transmission-line models. This feature is advantageous because it greatly facilitates the grid design procedure. The grid transmission-line models were derived using the induced EMF method — a technique readily applied when the structure is geometrically simple. Furthermore, we found, using a quasi-optical reflectometer, that the EMF transmission-line models were quite good as long as the grid period is small enough to prevent multimode propagation in the grid's dielectric substrate.

Although the EMF method is convenient in many circumstances, it is not well-suited for analyzing structures of arbitrary shape. Investigation of new grid configurations will be important and electromagnetic solvers such as Hewlett Packard's *High-Frequency Structure Simulator* will be of great use in such studies. By better understanding the electromagnetic properties of different grid configurations, the designer can optimize the grid structure for a particular device.

One of the main goals of quasi-optical grid research is the design and fabrication of high-power solid-state sources. The results presented in chapter 5

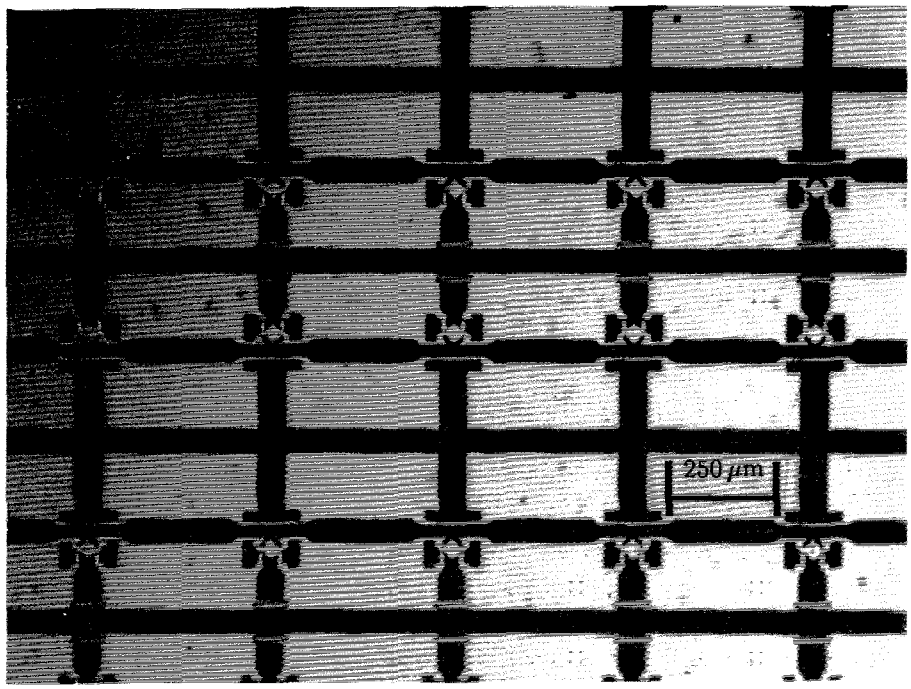

Figure 6.1 Photograph of a monolithic HEMT grid for operation at 94 GHz. The grid was designed by Michael De Lisio at Caltech and fabricated at Martin Marietta. The devices are spaced 440 μm apart and the substrate is GaAs.

have shown this to be feasible and much of the initial groundwork has been laid. Demonstration of a high-power oscillator is the next logical step. Two obvious ways of obtaining more power from grids are to build larger arrays and to use higher-power devices. It will also be necessary to find what impedances to present the devices for maximum efficiency and power output. With the fabrication of high-power oscillator grids, designers will need to consider the thermal properties of the arrays and provide a suitable means for heat removal.

In addition to attaining higher power levels, future grids will need to operate at millimeter-wave frequencies. As a result, high-frequency transistors such as pseudomorphic HEMT's and heterojunction bipolar transistors (HBT's) will need to be monolithically integrated into grid arrays. Figure 6.1 shows a photograph of the first monolithic HEMT grid. The grid was designed at Caltech by Michael De Lisio and fabricated at Martin Marietta in Baltimore, Maryland. It is designed

for oscillation at 94 GHz and testing is scheduled to begin soon. Working with the Rockwell Science Center in Thousand Oaks, California, we have also designed a number of HBT grids for operation at 44 and 60 GHz. These grids, which are to be fabricated on 150 μm thick GaAs, are scheduled to be completed in November 1991. For submillimeter-wave applications, grids containing resonant tunneling diodes and Josephson junctions bear consideration. Also, with the advent of monolithically integrated oscillator arrays, issues involving the grids' tolerance to device failure will need to be investigated.

Although important for many microwave and millimeter-wave systems, oscillators are only one possible use for active quasi-optical arrays. Amplifiers are necessary in most applications. Grid amplifiers, structures which amplify and reradiate incident radiation, should offer the same advantages as grid oscillators: increased power-handling capability and elimination of the losses associated with waveguides and feed networks. A grid amplifier was recently reported in the literature, and the results are encouraging [1]. A gain of 11 dB was obtained at 3.3 GHz. Future work with active quasi-optical grids will certainly involve amplifiers and may lead to better designs for amplifying signals without need for receiving and transmitting antennas.

In addition to oscillators and amplifiers, quasi-optical grids have been used for mixing [2], filtering, phase-shifting [3], and frequency multiplication [4]. All of the components needed for a basic heterodyne receiver have been demonstrated as quasi-optical elements. In principal, a complete quasi-optical system can be built by cascading grids one after another. Figure 6.2 shows how this might be done to build a receiver. An oscillator grid illuminates a mixer grid to provide an LO. A grid amplifier, followed by a quasi-optical filter, is placed at the receiver input. Dielectric slabs can be added to provide matching. Such a system is straightforward to build and does not require separate antennas that feed waveguides or transmission-line circuits; all signals propagate in free space.

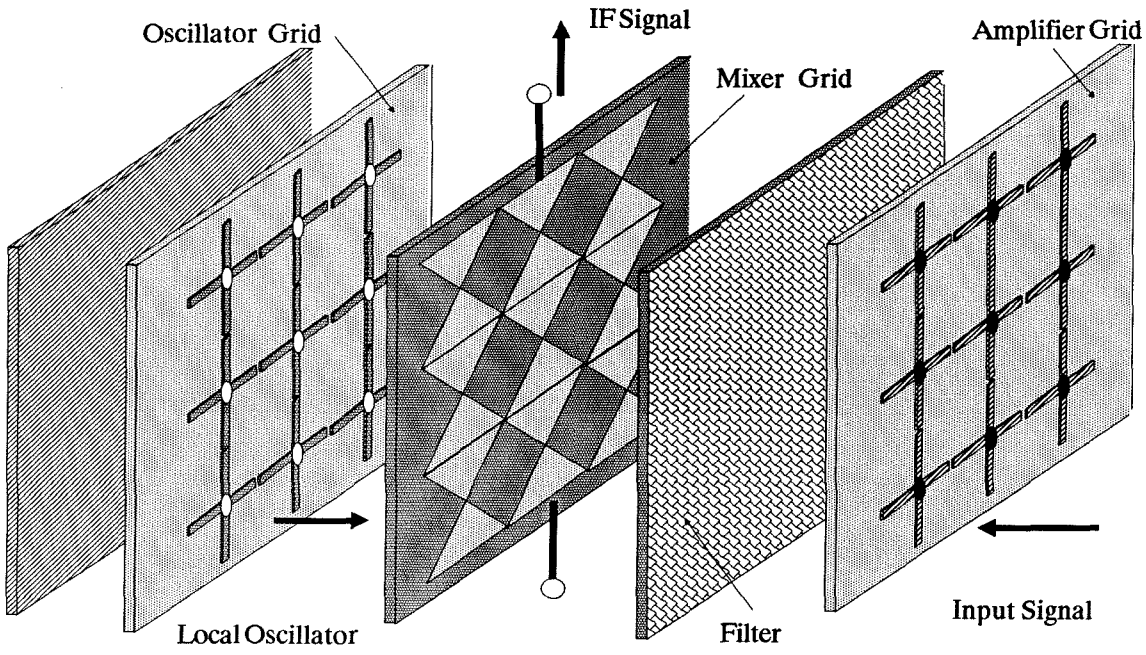

Figure 6.2 Schematic of a quasi-optical heterodyne receiver. A grid oscillator provides the LO and a grid amplifier followed by a filter constitutes the receiver's front-end. The IF is removed from the mixer with a coaxial cable.

References

[1] M. Kim, J.J Rosenberg, R.P. Smith, R.M. Weikle, II, J.B. Hacker, M.P. De Lisio, D.B. Rutledge, "A Grid Amplifier," *IEEE Microwave and Guided Wave Lett.,* vol. 2, no. 11, pp. 322-324, November 1991.

[2] J.B. Hacker, R.M. Weikle, II, M. Kim, M.P. De Lisio, D.B. Rutledge, "A 100-Element Planar Schottky Diode Grid Mixer," *submitted to the IEEE Trans. Microwave Theory Tech.,* July 1991.

[3] W.W. Lam, C.F. Jou, H.Z. Chen, K.S. Stolt, N.C. Luhmann, Jr., D.B. Rutledge, "Millimeter-Wave Diode-Grid Phase Shifters," *IEEE Trans. Microwave Theory Tech.,* MTT-36, pp. 902-907, May 1988.

[4] C.F. Jou, W.W. Lam, H.Z. Chen, K.S. Stolt, N.C. Luhmann, Jr., D.B. Rutledge, "Millimeter-Wave Diode-Grid Frequency Doubler," *IEEE Trans. Microwave Theory Tech.,* MTT-36, pp. 1507-1514, November 1988.

Appendix :

Center-Tapped Transformer Scattering Matrix

One of the important features of the transistor grid equivalent circuit derived in chapter 3 is the center-tapped transformer. To use this equivalent circuit, it is helpful to know the center-tapped transformer scattering parameters. These can be derived directly using the transformer circuit relations. Figure 1 shows the center-tapped transformer and defines the ports. We assume that port 1 is terminated with a characteristic impedance Z_1 and the remaining ports have characteristic impedance Z_0. The turns ratios for the transformer branches are m and n, with $m + n = 1$. The currents and voltages at the transformer ports are related by:

$$V_1 - V_2 + V_4 = 0 \tag{1}$$

$$nV_2 - V_3 + mV_4 = 0 \tag{2}$$

$$i_1 - mi_2 + ni_4 = 0 \tag{3}$$

$$i_2 + i_3 + i_4 = 0. \tag{4}$$

If a wave is incident on port 1, then we can use equations (1—4) to write expressions for the s-parameters describing the waves scattered to the other ports:

$$s_{11} - \frac{s_{21}}{\sqrt{z}} + \frac{s_{41}}{\sqrt{z}} = -1 \tag{5}$$

$$s_{11} + m\sqrt{z}s_{21} - n\sqrt{z}s_{41} = 1 \tag{6}$$

$$ns_{21} - s_{31} + ms_{41} = 0 \tag{7}$$

$$s_{21} + s_{31} + s_{41} = 0, \tag{8}$$

where $z = Z_1/Z_0$. These equations can be solved using Gaussian elimination or Kramer's rule to find the scattering parameters, s_{11}, s_{21}, s_{31}, and s_{41}. This method can also be carried out with waves incident on the other ports. For a wave incident on port 2, the s-parameter equations become:

$$\sqrt{z}s_{12} - s_{22} + s_{42} = 1 \tag{9}$$

$$s_{12} + m\sqrt{z}s_{22} - n\sqrt{z}s_{42} = m\sqrt{z} \tag{10}$$

$$ns_{22} + ms_{42} - s_{32} = -n \tag{11}$$

$$s_{22} + s_{32} + s_{42} = 1. \tag{12}$$

Similar sets of equations are generated by assuming waves are incident on ports 3 and 4. Solving these sets of equations, we find the four-port s-parameters for the center-tapped transformer are given by:

$$\frac{1}{\Delta}\begin{pmatrix} 3-2z(1-mn) & 2\sqrt{z}(1+m) & 2\sqrt{z}(n-m) & -2\sqrt{z}(1+n) \\ 2\sqrt{z}(1+m) & 2zm-1 & 2(1+zn) & 2(1-zmn) \\ 2\sqrt{z}(n-m) & 2(1+zn) & -(1+2zmn) & 2(1+zm) \\ -2\sqrt{z}(1+n) & 2(1-zmn) & 2(1+zm) & 2zn-1 \end{pmatrix} \tag{13}$$

where $\Delta = (1+n)(1+zn) + (1+m)(1+zm)$. As expected, the s-parameter matrix is reciprocal and, because the circuit is frequency-independent, real. It can also be shown, with some work, that the scattering matrix is lossless. It should be further noted that this scattering matrix assumes that the left side of the transformer of Fig. 1 is port 1. Ports 2, 3, and 4, however, are defined with respect to a floating ground terminal.

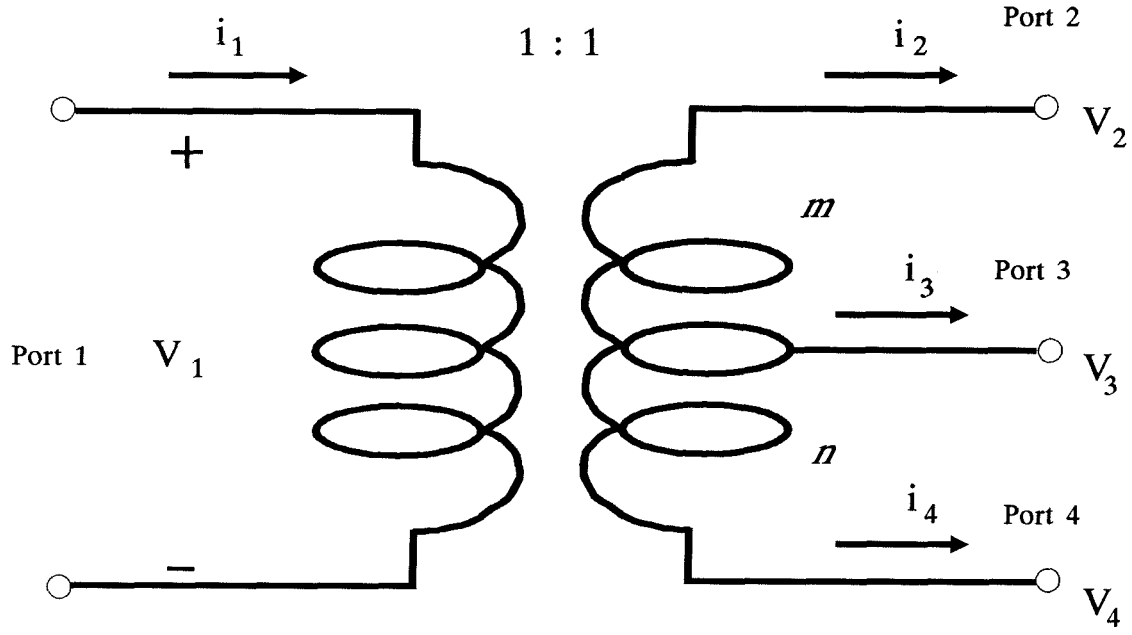

Figure 1 Schematic of a center-tapped transformer. All ports are assumed to be matched. Port 1 has a characteristic impedance of Z_1 and the other ports are terminated with impedance Z_0. Also, ports 2, 3, and 4 are defined with respect to a floating grounded terminal

For a symmetric ($m = n = \frac{1}{2}$) center-tapped transformer with port 1 representing free-space ($Z_1 = 377\,\Omega$) and the other ports terminated with $50\,\Omega$, the scattering matrix is:

$$S = \begin{pmatrix} -0.581 & 0.576 & 0 & -0.576 \\ 0.576 & 0.457 & 0.667 & -0.124 \\ 0 & 0.667 & -0.333 & 0.667 \\ -0.576 & -0.124 & 0.667 & 0.457 \end{pmatrix}. \tag{14}$$